2010

Interaction Between Secondary Flow & Film Cooling Jets Of A Realistic Annular Airfoil Cascade (High Mach Number)

Cuong Quoc Nguyen
University of Central Florida

STARS Citation
Nguyen, Cuong Quoc, "Interaction Between Secondary Flow & Film Cooling Jets Of A Realistic Annular Airfoil Cascade (High Mach Number)" (2010). *Electronic Theses and Dissertations, 2004-2019*. 1651.
https://stars.library.ucf.edu/etd/1651

INTERACTION BETWEEN SECONDARY FLOW & FILM COOLING JETS OF A REALISTIC ANNULAR AIRFOIL CASCADE (HIGH MACH NUMBER)

by

CUONG QUOC NGUYEN
B.S.A.E., HCM City Polytechnique University, 2002
M.S.M.E., University of South Florida, 2006

A dissertation submitted in partial fulfillment of the requirements
for the degree of Doctor of Philosophy in Thermo-Fluid Sciences
in the Department of Mechanical, Materials, and Aerospace Engineering
in the College of Engineering and Computer Science
at the University of Central Florida
Orlando, Florida

Fall Term
2010

Major Professor: Jayanta Kapat

ABSTRACT

Film cooling is investigated on a flat plate both numerically and experimentally. Conical shaped film hole are investigated extensively and contribute to the current literature data, which is extremely rare in the open public domain. Both configuration of the cylindrical film holes, with and without a trench, are investigated in detail. Design of experiment technique was performed to find an optimum combination of both geometrical and fluid parameters to achieve the best film cooling performance. From this part of the study, it shows that film cooling performance can be enhanced up to 250% with the trenched film cooling versus non-trenched case provided the same amount of coolant. Since most of the relevant open literature is about film cooling on flat plate endwall cascade with linear extrusion airfoil, the purpose of the second part of this study is to examine the interaction of the secondary flow inside a 3D cascade and the injected film cooling jets. This is employed on the first stage of the aircraft gas turbine engine to protect the curvilinear (annular) endwall platform. The current study investigates the interaction between injected film jets and the secondary flow both experimentally and numerically at high Mach number (M=0.7). Validation shows good agreement between obtained data with the open literature. In general, it can be concluded that with an appropriate film coolant to mainstream blowing ratio, one can not only achieve the best film cooling effectiveness (FCE or η) on the downstream endwall but also maintain almost the same aerodynamic loss as in the un-cooled baseline case. Film performance acts nonlinearly with respect to blowing ratios as with film cooling on flat plate, in the other hand, with a right blowing ratio, film cooling performance is not affect much by secondary flow. In turn, film cooling jets do not increase pressure loss at the downstream wake area of the blades.

TO MY PARENTS

WHO ARE ALWAYS THERE FOR ME

ACKNOWLEDGMENTS

To my family who always guide me, support me and love me more than anything else. Thank you for unbound love from my parents, former grandparents and my family members. I give thanks to the United State of America which has supported and helped me to achieve goals in my life. Special thanks due to my major advisor, Dr. Jayanta S. Kapat, who plays a role model in my career life with his dedication for science. I would like to thank to all my committee members: Dr. Reda Mankbadi (co-advisor), Dr.Bijay Sultanian, Dr. Marcel Ilie, Dr. Juan Gou, Dr. Ratan Guha, and Dr. Son Ho for their valuable time and support. I owe an extremely deep appreciation to Dr. Son Ho for his valuable time on supporting me throughout this study.

I appreciate Dr. L. Malone (UCF, Orlando, FL) for her very valuable advises in the field of design of experiment and Dr. E. Steinthornsson (Parker Hannifin, Mentor, OH) for his fruitful discussions and advices in numerical simulation. I thank to Dr. J. Ling (Alstom, Switzerland), Dr. S. Rodriguez (L3, FL), Dr. Donald Gauthier (PSM, FL), and Dr. H. Zuniga (Siemens, FL) for their contributions in this study. Finally, I like to thank for my friends| my colleagues William M., Matt G., Bryan B., Mark R., Lucky T., Tim C., Perry J., Nghia T., Craig N., Quan L., Vaidy K., Carson S., Lee K., Mike, An L., Sri K., Jared P., Ahbishek S., Stephanie K., Michelle V. for their friendships and encourage during the treasure time in the CATER Laboratory.

Next, I would like to express special thank to NASA (FCAAP program), Siemens Energy for funded E^3 and BFC projects, and the UTSR fellowship program. Final but not least, I ultimately appreciate Parker Hannifin Corporation for its supporting on computing resource.

TABLE OF CONTENTS

LIST OF FIGURES

LIST OF TABLES

NOMENCLATURES

BR	Blowing ratio
C	Chord
CUC	Cooling uniformity coefficient
D	Nominal metering hole diameter, mm
DR	Density ratio, ρ_c/ρ_m
FCE	Film cooling effectiveness
k	Thermal conductivity, $Wm^{-1}K^{-1}$
L	Length of hole center line axis, mm
m	Mass flow, kg
MR	Momentum flux ratio
N	Number of cooling holes on a test coupon
P	Pressure, Pa
p	Distance between 2 neighbor holes, mm
PR	Pressure ratio
R	Specific gas constant, 287 Jkg^{-1} K^{-1}
T	Temperature, K
V	Velocity, ms^{-1}
x	Distance in the mainstream direction, mm

y	Distance in the lateral direction, mm
y^+	Dimensionless wall distance

Greek symbols:

α	Film injection angle, degree
β	Compound angle
η	Film cooling effectiveness
γ	Specific heat ratio
ρ	Density, kgm^{-3}
ζ	Pressure loss coefficient
Φ	Angle of attack
Ψ	Flow exit angle
γ	Conical flaring angle
∞	Main flow (free stream)

Subscripts:

a	Actual (or axial direction in chapter 4 and 5)
c	Coolant
cl	Centerline
m	Mainstream
s	Static
t	Total

r	Recovery

Superscripts:

-	Laterally-averaged
=	Spatially-averaged
•	Rate of change, 1/s

Acronyms:

LE	Leading edge
TE	Trailing edge
FHP	Five hole probe
BFC	Basic film cooling (wind tunnel)
E^3	Energy efficient engine
RANS	Reynolds Averaging Navies-Stoke
LES	Large eddy simulation
CATER	Center for advanced turbine energy research

CHAPTER I: BACKGROUND AND LITERATURE REVIEW

This chapter overviews gas turbine engines, its applications and the need for cooling on the working surfaces. Background of this innovative film cooling technology will also be covered. We will mention the application of film cooling on the flat plate and annular airfoil cascade. Then, we will walk through literature for the current state of the art about film cooling and available open public domain data. Finally, the contribution of the current study will be stated.

I.1 Introduction

Gas turbines, which are mainly operated based on the Brayton cycle, are very low in emission, installed cost, but high efficiency as well as very fast response with respect to equivalent engines, for example: steam turbines, wind turbines, etc. Still, gas turbines' efficiency has been constantly improved since the first time it was introduced (early 1800's). That is the reason why it is employed not only in electrical power generation (approximately 5000 plus power plants over the world at the moment) but also in aero propulsion (about 200,000 plus commercial aircrafts nowadays) as well as in marine application as depicted in Figure 1. Furthermore, combined cycle power plant can bring the overall cycle efficiency up to 65% thermal cycle efficiency.

Figure 2 shows a typical layout of a gas turbine engine which is composed of compressor, combustor and turbine. Thermal cycle efficiency for a gas turbine is given in the Equation 1.1

$$\eta_{cycle} = \frac{q_i - q_o}{q_i} \tag{1.1}$$

where q_i is the supplied heat from the combustor reaction as shown in the Figure 1.2 (a), q_o is the heat coming out the system at the exit of the turbine component. For a simple process assumption, η_{cycle} can be expressed as in Equation 1.2 and Equation 1.3

$$\eta_{cycle} = 1 - \frac{(T_4 - T_1)}{(T_3 - T_2)} \tag{1.2}$$

$$\eta_{cycle} = 1 - \frac{T_4\left(1 - {}^{T_1}\!/_{T_4}\right)}{T_3\left(1 - {}^{T_2}\!/_{T_3}\right)} \tag{1.3}$$

where T_1, T_2, T_3, and T_4 are the temperatures at the compressor inlet, compressor exit, turbine inlet and turbine exit respectively. For an isentropic process, one can have the result shown in Equation 1.4

$$\frac{T_1}{T_4} = \frac{T_2}{T_3} \tag{1.4}$$

Substitute Equation 1.4 into Equation 1.3, we can have Equation 1.5

$$\eta_{cycle} = \eta_{ideal,Brayton} = 1 - \frac{T_4}{T_3} \tag{1.5}$$

In order to increase the cycle efficiency of the gas turbine engine, higher rotor inlet temperature is desired (the turbine inlet temperature, T_3), which is one of the most appropriate solution (Goldstein and Chen, 1985, Sinha et al., 1991; Bunker, 2002; Gritsch et al., 2003). Unfortunately, without protection, T_3 can only reach the melting temperature of the sophisticated metal components, which is limited to somewhere 1200K-1400K in the present (Lashminarayana, 1999; Kiezow and Kapat, 2008) and it is shown in Figure 3.

However, thanks to contributors to the current accumulated film cooling knowledge and thermal barrier coating technology (TBC), film cooling technology was invented and came into play back in 1940, (Kercher, 2003) from a work of Bohl, who was believed to be the first to apply film cooling first in cooling mechanical engineering parts. In other words, in film cooling technique, a solid surface is protected from the extremely hot mainstream by injecting coolant jets out of the surface (Eckert and Drake, 1987)

The injected "cool" air that is usually from 800F to 1100F (700-900K) is cold only with respect to the turbine rotor and stator inlet temperature which can be as high as 3000F (1900K). In 2005, Cardwell reported that if one can manage to reduce 25F of the metal surface temperature at 2225F, they could extend twice the life of that working part as shown in Figure 4 (a). In fact, there are many components failures which due to fraud cooling practice in gas turbines, have occurred during last several decades. A typical fraud case is selected to show in the Figure 4 (b).

In the past, mid-span flow which came out of the combustor was usually kept hotter than the flows that are close to the inner and outer platforms (Friedrichs, 1997). Since, the mean turbine rotor inlet temperature is continually rising; the result is endwall film cooling design has become an important task to protect the hub and the casing surfaces in the gas turbine engines. Figure 5 shows typical configuration of film cooling on endwalls of a first stage vane.

I.2 Background

The major role of film cooling application is then to reduce the heat transfer between the hot mainstream and the body surface. There is several film cooling schemes as shown in Figure 6. In general, heat flux is given in the Equation 1.6.

$$q'' = h\left(T_{ref} - T_w\right) \tag{1.6}$$

where h is the heat transfer coefficient; T_{ref} and T_{w} are the reference and wall temperatures respectively. For the case of the present of film cooling (Figure 7a), T_{ref} should be assigned as the temperature of the local fluid right above the wall, $T_{\mathrm{ref}}=T_{\mathrm{f}}$. Provided we have an adiabatic surface, which one often assume in most of film cooling analysis, needs to be cooled, then the T_{f} in the above Equation 1.6 is equaled to the T_{aw}, which is the temperature of the fluid sitting right above the adiabatic surface. Then, the heat transfer flux between the surface and the fluid is given in the Equation 1.7

$$q_f^{"} = h_f\left(T_{aw} - T_w\right) \tag{1.7}$$

In the case without film cooling scheme applied, the heat transfer flux is given as Equation 1.8

$$q^{"} = h\ \left(T_m - T_w\right) \tag{1.8}$$

where T_{aw} is usually found experimentally in the term of film cooling effectiveness, η as given in Equation 1.9, where T_{m} is replaced by T_{r}.

$$\eta(x,y) = \frac{T_{aw}(x,y) - T_r}{T_c - T_r} \tag{1.9}$$

where η becomes unity represents an ideal cooling scenario (the surface has the same temperature of the injected coolant); while η equal zero means that we gain nothing in that specific film cooling arrangement. There are two alternate forms of film cooling effectiveness, which are used extensively in literature for comparison among film cooling designs: laterally averaged film cooling effectiveness (Equation 1.10) and spatially averaged film cooling effectiveness (Equation 1.11). Blowing ratio, *BR* which is a ratio of mass flux between the coolant and the mainstream, is often mentioned in film cooling technology and defined as in Equation 1.12

$$\bar{\eta}(x) = \frac{\int \eta(x,y)dy}{\int dy} \tag{1.10}$$

$$\bar{\bar{\eta}} = \frac{\int \eta(x,y)\,dxdy}{\iint dxdy} \tag{1.11}$$

$$BR = \frac{(\rho V)_c}{(\rho V)_m} \tag{1.12}$$

Film cooling performance can be affected by many involved factors (input variables) which can be classified as: (1) Flow conditions group: the momentum ratio (*MR*, is the ratio between the linear momentum of the injected coolant over the mainstreams, Equation 1.13, 1.14 and 1.15); the density ratio (*DR*, is the ratio of coolant density over the mainstream density, Equation 1.16). (2) Geometrical parameter group as depicted in the Figure 8: the inclination angle between the hole and the main stream surface (α), the ratio of the pitch over the hole diameter (*P/D*), and the ratio between the length of the hole and the diameter (*L/D*)

$$MR = \frac{\left(\rho V^2\right)_c}{\left(\rho V^2\right)_m} \tag{1.13}$$

$$MR = \frac{(\rho V)_c \big/ (\rho V)_m}{\rho_c \big/ \rho_m} \tag{1.14}$$

$$MR = \frac{BR^2}{DR} \tag{1.15}$$

where:

$$DR = \frac{\rho_c}{\rho_m} \tag{1.16}$$

Basically, to evaluate the benefit of any film cooling design, one can consider the ratio of heat transfer with the present of film cooling scheme to the no-film-cooling case: q_f/q. This ratio can be estimated as in Equation 1.17 and 1.18

$$q_f \big/ q = \frac{h_f \left(T_f - T_w\right)}{h \left(T_m - T_w\right)} \tag{1.17}$$

$$q_f \big/ q = \frac{h_f}{h} \frac{\left(T_f - T_w\right) \big/ \left(T_m - T_c\right)}{\left(T_m - T_w\right) \big/ \left(T_m - T_c\right)} \tag{1.18}$$

To simplify the form of this equation, one can transform the dependent variable by defining a non-dimensional (normalized) temperature, θ as in Equation 1.19

$$\theta = \frac{T_m - T_w}{T_m - T_c} \tag{1.19}$$

Then:

$$q_f / q = \frac{h_f}{h} \frac{\eta}{\theta} \tag{1.20}$$

So, as seen in Equation 1.20, one needs to design film cooling scheme in order to bring q_f/q as close to zero as possible, but also want to push η as close to unity as much as possible. Therefore, both film cooling effectiveness and film cooling heat transfer coefficient are important in judging any film cooling design and film cooling performance.

Therefore, to obtain and fully control these factors are extremely important. It obviously requires a good understanding of interaction structure between the film cooling jet and the hot mainstream. The author of this study would like to contribute to the current knowledge on the basis film cooling behavior on a flat plate, and then from there the author wants to extend the work to an annular 3D cascade film cooling where the mainstream itself possess a complex flow with a presence of secondary flows which inhered from the suction-side horseshoe vortex, pressure-side horseshoe vortex (will turn into passage vortex), endwall cross flow, etc. as depicted in the Figure 9 as a wonderful classical sketch from the work of Langston (1980).

I.3 Literature Review

Film cooling was usually addressed as a "boundary-layer cooling" and was introduced back to 1929 by R.H. Goddard, who was considered the first known pioneer film cooling applicator (Kercher, 2003). He applied boundary-layer cooling technique for the combustor chamber wall of the rocket motor propellant. The work was reported in "Rocket Development" in 1948.

In 1940, J.G.E.V Bohl is known as the person wrote the first boundary-layer cooling technical paper. In his work, “Das Verhalten Paralleler Luftstrahlen” where he studied the behavior of parallel flow (main flow and the injected coolant). M.J. Zucrow was known as the first one who applied boundary-layer cooling for weapon systems (WW2 German V-2 rocket chamber). Film cooling for gas turbine was not happened until 1948 when P. Destival employed discrete hole to cool a French turbo-propeller and turbo reaction machine.

Then the film cooling technique was soon to be one of the hottest research science topics which can be reflected through number of technical papers and reports as listed by D.W. Kercher in 2003 (Kercher, 2003). The work can be plotted as in Figure 10. The work was drastically increased in the ’60s (almost three times) and was doubled in the ‘70s. There is really a hidden factor that there was not an increase of film cooling research in the ‘80s, since anyone could easily make any prediction. But, the trend was again came back in the ‘90s and ‘2000s. In general, film cooling work is kept increasing every decade which prove that it is one of the most useful and long living technical topic.

Since there is a large amount of film cooling research, the author only able to address some typical and most cited work, which could be classified as experimental work with advanced measurement techniques, numerical work with RANS simulation scheme, and application of statistical methods on film cooling study.

Zhang and Jaiswal (2001) studied film cooling effectiveness on a flat turbine nozzle end-wall. It was reported that for low blowing ratios the secondary flows dominate over the momentum of the jet, resulting in a decrease in effectiveness. On the contrary, at high blowing ratios the jet momentum overcomes the flow field yielding to a higher effectiveness.

Film cooling performance is affected by not only geometrical parameters (shape of the film cooling hole, injection angle, inclination angle, etc.) but also the flow conditions. From the sensitivity analysis work of Nguyen et al. (2009), the most important flow factor is the blowing ratio (*BR*), which is defined as mass flux ratio of the coolant over the main flow (Equation 1.12). Density ratio (*DR*) is simply the ratio of film coolant density to the mainstream density. The momentum flux ratio, *MR* is defined similarly to the blowing ratio. While the blowing ratio is based on the velocity of the coolant, the momentum flux ratio is more closely related to its energy. *MR* is used to compare the kinetic energy of the coolant (per volume) versus that of the mainstream.

The pitch-to-diameter ratio (*p/D*) was studied by Dorrington and Bogard (2007). They varied *p/D* between 2.78, 4, and 5, and it was concluded that the optimal *p/D* was 2.78. This result proved to be significant. It showed that as the pitch decreased, more coolant was ejected to the main flow per unit length and the added interaction between closed jets led to a behavior approaching that of a trench. Harrison and Bogard (2007) conducted a numerical study and confirmed that the jet interaction was the driving mechanism behind the improvement shown by trenched film cooling holes.

The trench depth-to-diameter ratio was studied by Nguyen et al. (2010). Their result showed that there was a large improvement in terms of thermal performance when the trench depth was increased from 0.1*D* to 0.55*D*. Also, there is not a significant increase in film cooling performance when trench depth is increased up to 1*D*.

Their result is confirmed by a study of Wang et al. (2002). Wang investigated the performance of such a configuration in terms of mixing and its consequent benefit to film cooling applications. He studied multiple parameters in order to determine how to transform discrete hole cooling into a 2*D* phenomenon. Wang found that the ideal slot depth ranged from 2 to 2.8 diameters and was perpendicular to the primary flow (i.e. with 90^{o} inclination angle). Note that the trench was primarily initiated from a repair process, which means that the trench depth was about the thickness of the TBC and bond layer coats, which was in the order of 10/1000” to 45/1000” as shown in the Table 1. The thickness of the bond coat is typically known as of 3/1000” to 12/1000”. So the depth of a typical trench can vary practically from 13/1000” to 57/1000”.

Table 1 Typical Thickness of TBC Coating Layer (Courtesy of Power System Mfg,. Inc.)

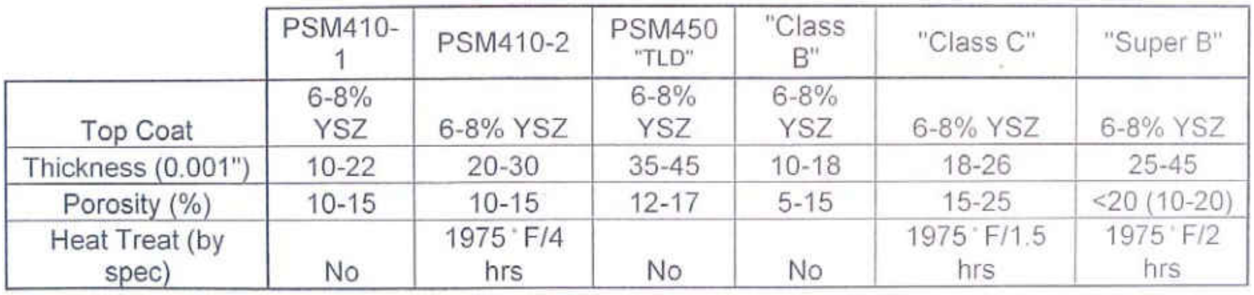

	PSM410-1	PSM410-2	PSM450 "TLD"	"Class B"	"Class C"	"Super B"
Top Coat	6-8% YSZ	6-8% YSZ	6-8% YSZ	6-8% YSZ	6-8% YSZ	6-8% YSZ
Thickness (0.001")	10-22	20-30	35-45	10-18	18-26	25-45
Porosity (%)	10-15	10-15	12-17	5-15	15-25	<20 (10-20)
Heat Treat (by spec)	No	1975 °F/4 hrs	No	No	1975 °F/1.5 hrs	1975 °F/2 hrs

Nguyen et al. (2009) claimed that *DR* was not a significant factor on the spatially-averaged FCE in comparison to the *BR* (most significant factor) and hole length-to-diameter ratio (*L/D*). As *DR* decreased from the high to a middle level (from 2.0 to 1.5), the spatially-averaged film cooling effectiveness (FCE) increased because the momentum flux has increased from 1.125 up to 1.5. This increase allowed the coolant flow to retain enough energy to spread out towards the downstream area after reattaching onto the downstream surface. However, the reduction in *DR* from 1.5 to 1 made *MR* increase up to 2.25. The excessive energy transferred *MR* to the coolant jet, which made the coolant reattachment move further in the downstream direction. If *DR* continued to reduce, the coolant flow would not be able to reattach onto the flat plate. Hence this reduced film performance.

Film cooling performance is affected by many factors. Only by employing design of experiment (DOE) can one find an appropriate combination of geometrical and flow parameters for optimizing the cooling design

I.4 Current Work and Contribution to the Engineering Society

The current study will have two parts: film cooling on flat plate and film cooling on an inner platform inside a cascade. The current study will consider the effect of the material conductivity with conjugate heat transfer numerical model, and this study also contributes to the availability of open-domain data about the film cooling performance of the conical-shape film hole both numerical analysis as well as experiment. Further, endwall film cooling has been studied for many years, but the majority of the work concerns straight cascades with two-dimensional (2D) extrusion airfoil vanes or blades. These are obviously a simplification and therefore many important effects cannot be studied. As the result, Burd and Simon (2003) pointed out that there has been little appreciation for the role of, and added complexity imposed by, reduced aspect ratios. A minor flow which is superimposed on the main flow is named a secondary flow. In this case, the secondary flows can be on the same order of magnitude as the primary flow. This current work will focus on the realistic cascade: 3D profile of airfoils plus annular endwalls, not a simple 2D extrusion airfoil with flat endwalls. The effect of film cooling jets on the aerodynamic performance (specifically: the loss coefficient at the downstream zone) and vice versa, i.e. the effect of the complex secondary vortex will affect the performance of the film cooling on the inner diameter (ID) endwall.

Figures

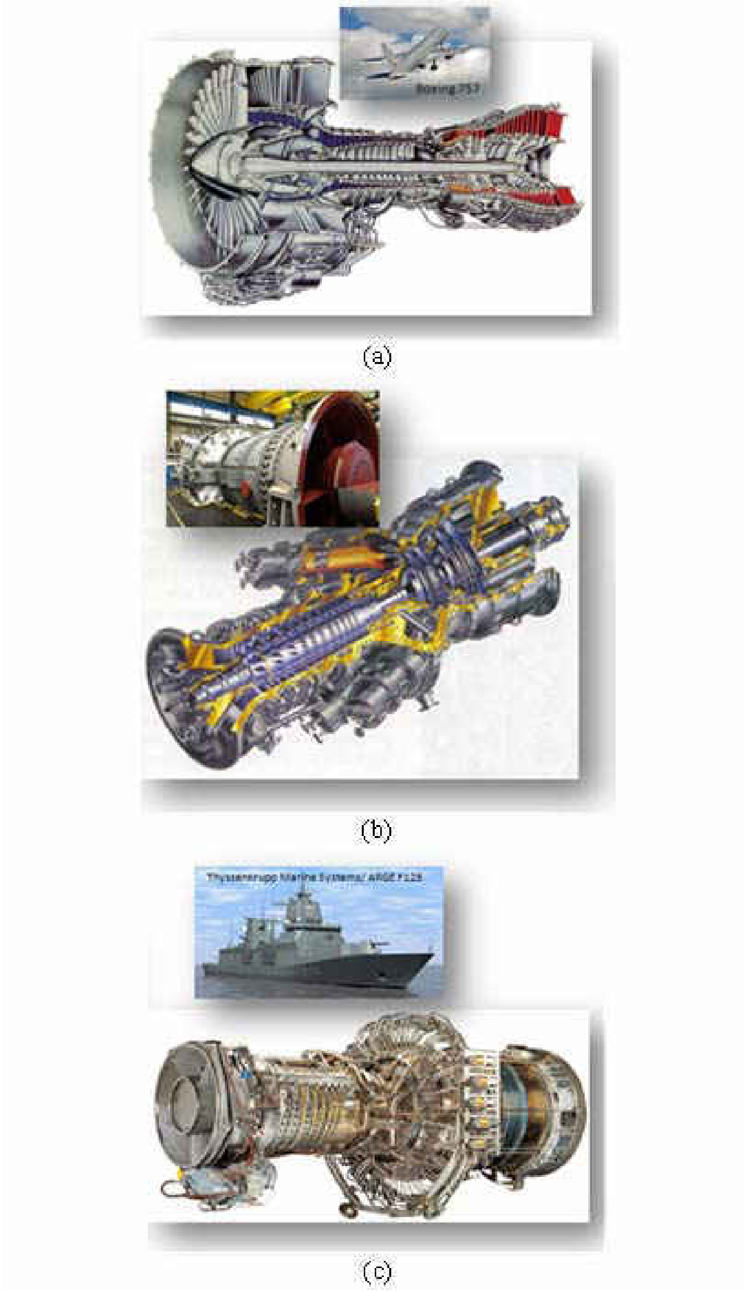

Figure 1 Applications of gas turbine engines in: (a) aero propulsion, turbo fan PW2000; (b) electrical generation, GE MS5000 2E; (c) marine applications, GE LM2500

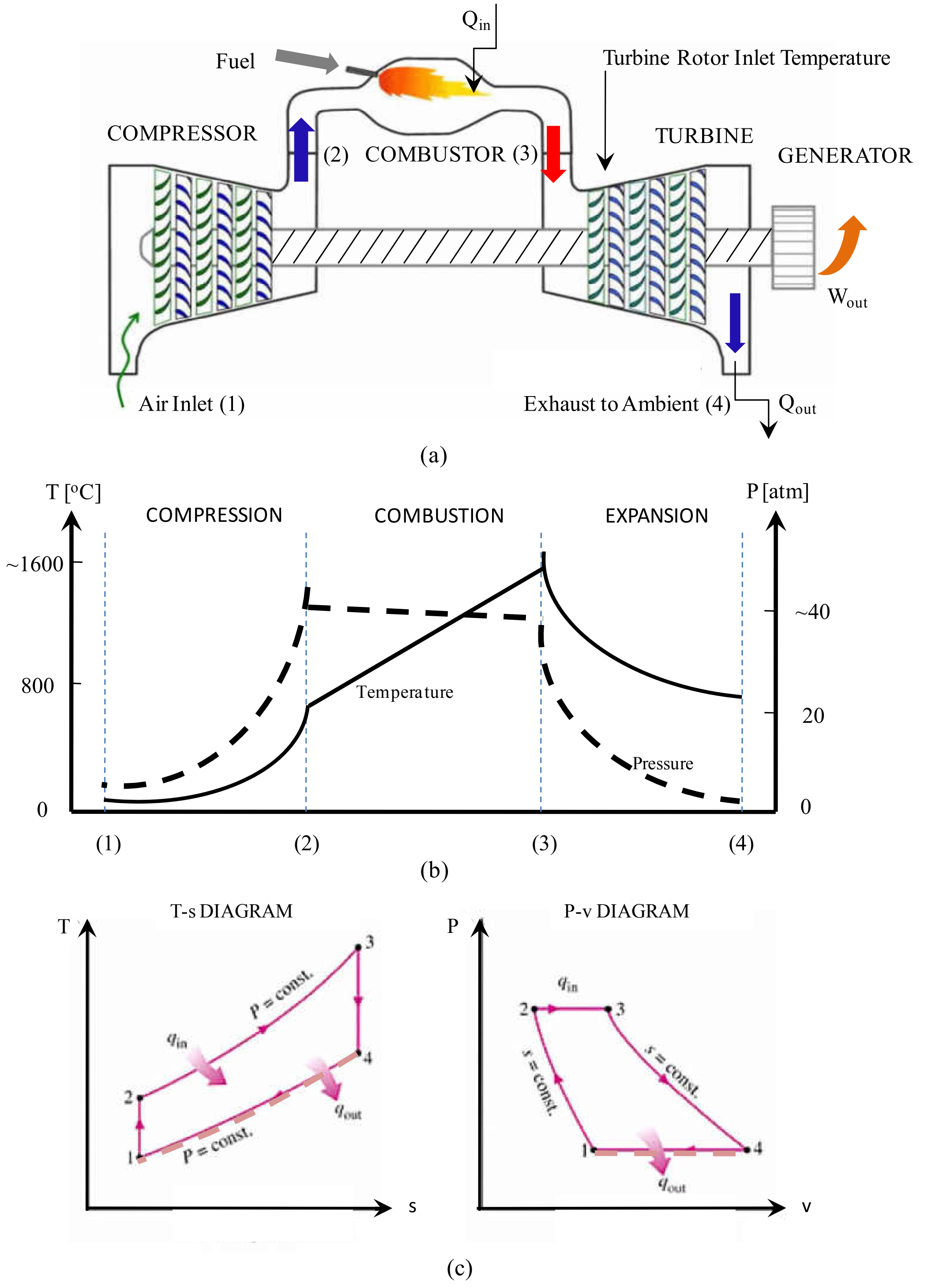

(a)

(b)

(c)

Figure 2 (a) Schematic of Gas Turbine Engine, (b) Temperature and Pressure of a Typical Operation Condition and (c) T-s and P-v Diagrams for an Ideal Brayton Cycle

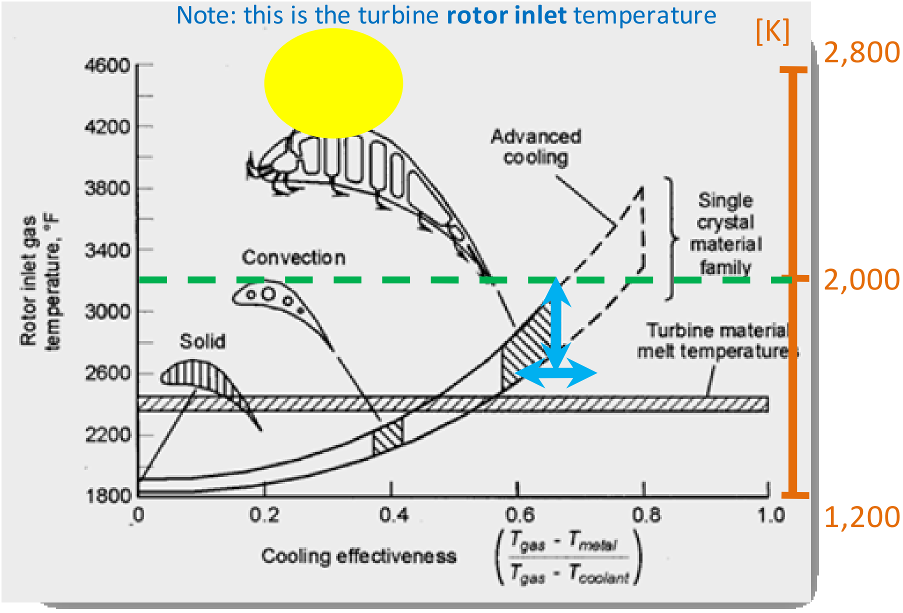

Figure 3. Turbine Rotor Inlet Temperature versus Cooling Effectiveness at Different Schemes of Cooling Technologies (Moustapha et al., 2003)

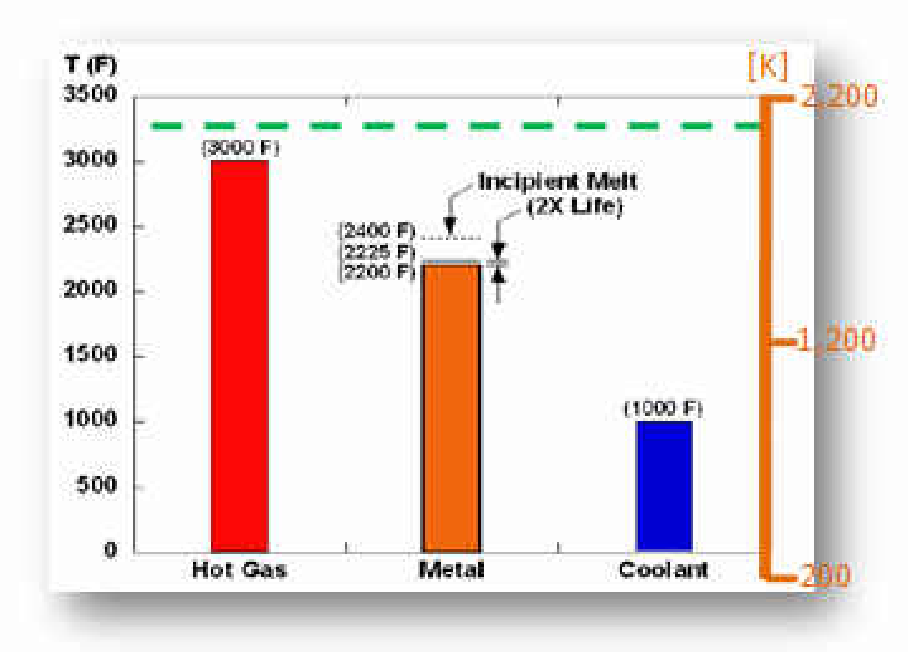

(a)

(b)

Figure 4 (a) A Reducing Metal Temperature of 25F can Double the Part Life (Cardwell, 2005 with Modification) and (b) A Typical Part Failure Occurred in the Turbine First Stage If It Is Not Cooled Properly (Sawyer, 1966)

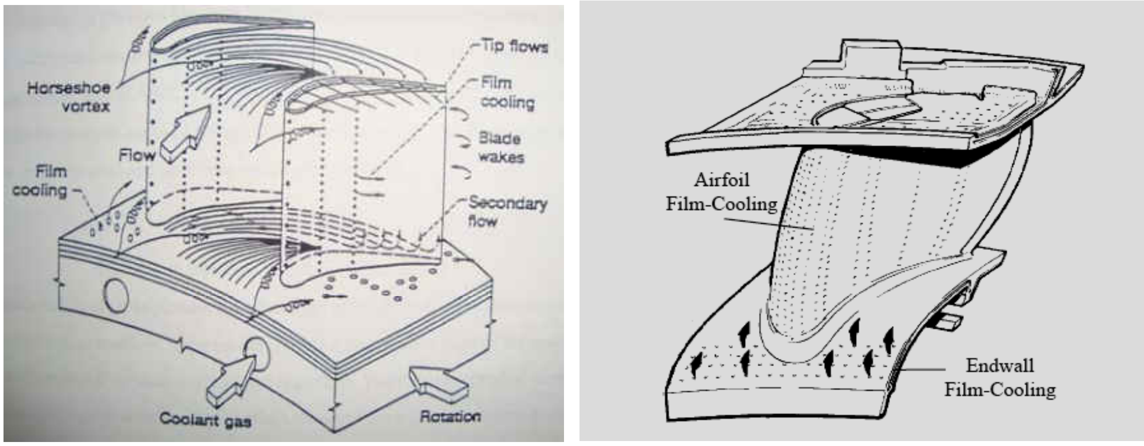

(a) (b)

Figure 5 Typical Endwall Film Cooling Configuration: (a) Blade/Rotor Row from Leylek, 1998, and (b) Vane/Stator Row from Freidrich, 1997

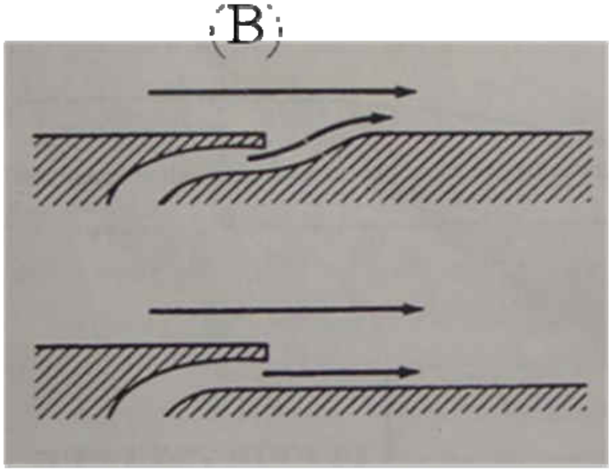

E.R.G. Eckert & R.M. Drake (1987, modified)

Figure 6 Various Film Cooling Arrangements (Eckert and Drake, 1987)

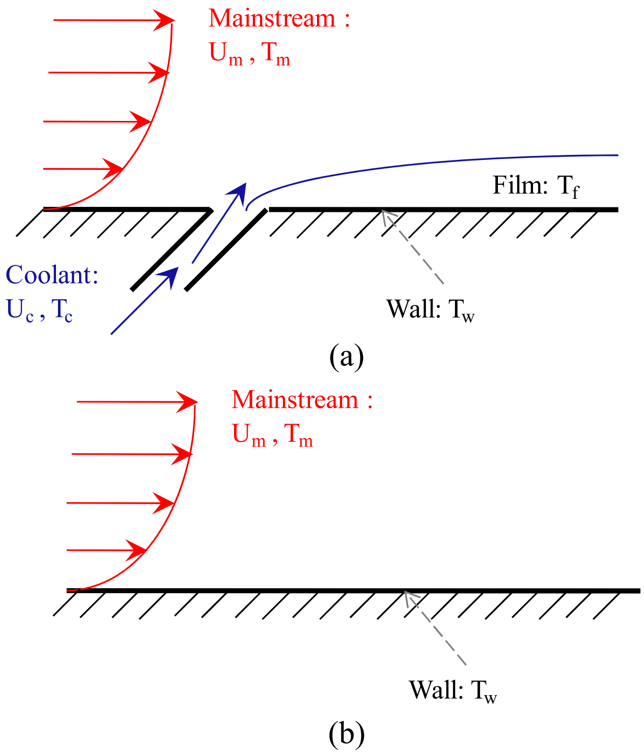

Figure 7 Graphic Depiction of a Hot Mainstream over a Flat Surface with film-Cooled Arrangement (a), and without Film Cooling (b)

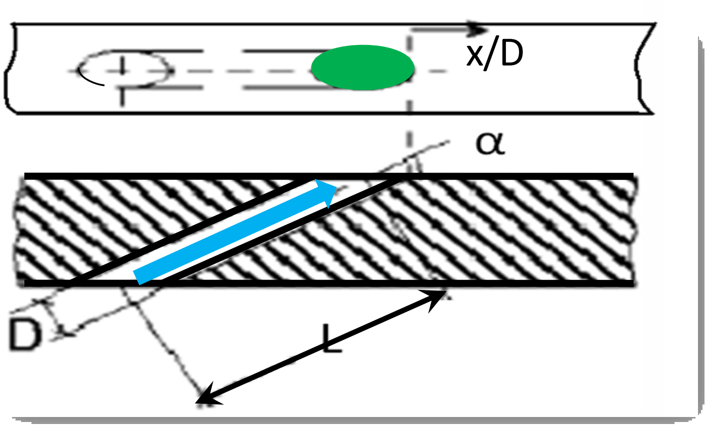

Figure 8 Schematic of the Geometrical Factors

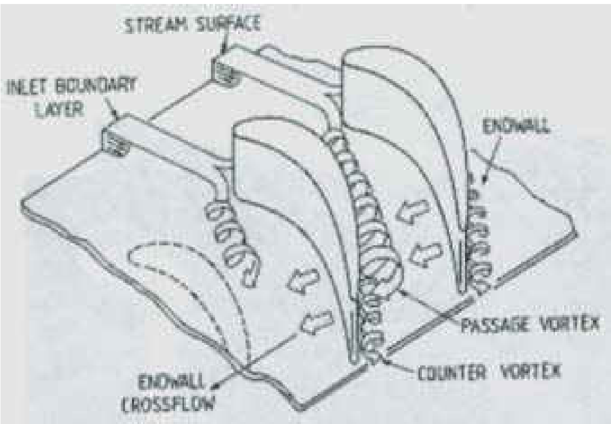

Figure 9 Complex Secondary Flow Structure, adapted from Langston (1980)

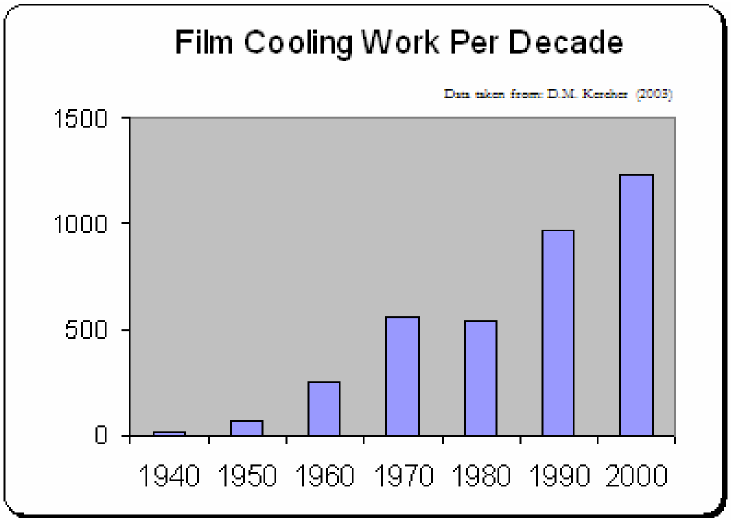

Figure 10 Technical Papers and Works on Film Cooling per Decade (adapted from Kercher (2003)

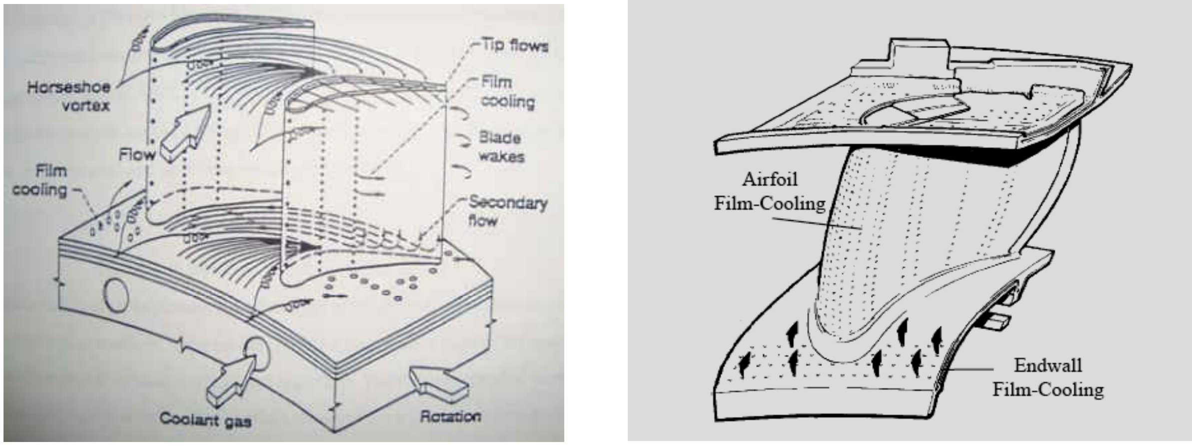

(a) (b)

Figure 11 Typical endwall film cooling configuration: (a) Blade/Rotor row from Leylek-(1998), and (b) Vane/Stator row from Freidrich (1997)

CHAPTER II. EXPERIMENTAL, NUMERICAL AND STATISTICAL APPROACHES

Three different approaches are used in this current study: conducting experiments, modeling simulation and employing statistical tools to analyze and gain depth in understanding the physics of film cooling behavior in both flat plate and on the hub platform of the annular transonic cascade.

II.1 Advanced Measuring Approach

Temperature Sensitive Paint

To capture the temperature distribution on the surface, the surface is painted with a temperature sensitive paint (TSP) manufactured by ISSI Inc. TSP liquid is made by dissolving luminescent florescent molecules with a transparent polymer in a solvent which is common for both species. The role of the polymer is adhering the luminescent onto the studied surface. Detail of temperature paint formulation as well as the corresponding inventors is reviewed in the work of Qiu (2001).

The florescent molecule is excited by shinning a proper light source which is composed of an array of blue LED also from ISSI Inc. The 76-LEDs lamp gives a peak intensity at 464nm wave length as shown in Figure 12. At a result, the luminescent molecule is excited electronically to an elevated energy level. However, this level will be deactivated back to ground state by a photo-thermal process, oxygen-quenching, which in turn will emit out a luminescent wavelength as following the energy level diagram showing in Figure 13. This emission intensity is strongly dependent on the local temperature of the surface. The intensity of the emitted wavelength is filtered and captured by a high resolution Charged Couple Device camera (CCD). A sketch of the TSP test set up is given in Figure 14.

After applying several layers (more than three coats are recommended, Qiu [2001]) on the studied surface, the surface then undergoes heat treatment by placing it in an oven or directly applying heat using a dryer. The surface is then ready to deploy for a new test in a wind tunnel and it takes about two to three hours for the surface temperature to reach steady state in the Basic Film Cooling (BFC) subsonic wind tunnel. A calibration process is conducted in advance to establish a correlation between the intensity and a correlation of the local temperature. This calibration curve is then employed to extract temperature on the studied surface with an intensity field which has just been captured by the CCD camera.

Boundary Layer Probe

An L-shaped United Technology boundary layer probe is used to measure the boundary layer thickness at the entrance of the testing area on the surface. Figure 15 shows a typical shape of the probe, whose special neck design help to reduce associated potential errors. The tip is a cylinder of 0.025” diameter (0.625mm), which is tapered to conform to the flat surface. This will help to collect data on the surface as close to 1-2mm. The tip tube is connected to the port at the tail of the probe where total pressure is measured with a Scanivale pressure transducer system. Based on the measured total pressure and the freestream static pressure, one can easily extract the velocity of the incompressible flow following the Equation 2.1.

$$V(y) = \sqrt{\frac{P_t(y) - P_s(y)}{0.5\,\rho}} \tag{2.1}$$

where: y is the vertical location with respect to the platform. Velocity profile can be plotted and boundary thickness can be determined at the distance where V reached 99% of the freestream velocity (V_{m}).

Five-Hole Probe

An L-shaped Aero-Probe five-hole probe (FHP) is deployed and depicted as in Figure 16. The probe has five holes: one is in the middle of the tip, and four holes is distributed around the circumference of the tip as sketched in Figure 17. The 5-hole probe was used to measure the exit flow field (total pressure, static pressure, and flow angles). The 5-hole probe has the advantage of an acceptance angle of 45° in both yaw and pitch planes, as compared to 5° for a traditional Pitot tube. Since the exact direction of the velocity vector may not be known everywhere, this major feature will be of great assistance. The measured data can be processed to provide velocity magnitude, direction, static pressure and stagnation pressure. Calibration will provide yaw, pitch, total and total minus static pressure, coefficients. A data reduction software which also came from Aero-Probe is used to obtain the flow field data.

II.2 Computational Simulation Approach

A steady state Reynolds Averaged Navier-Stokes (RANS) viscous model is adopted to conduct the numerical simulation for this current study. In general, governing equations of any flow field are well known and revisited in the Equation 2.2 to 2.4, which are mass conservation, and momentum equations written in the short notation that represent momentum in three directions, the last one, Equation 2.4, is the energy conservation.

$$\frac{\partial \rho}{\partial t}+\frac{\partial \rho U_i}{\partial x_i}=0 \tag{2.2}$$

$$\frac{\partial \rho U_i}{\partial t}+\frac{\partial \rho U_i U_j}{\partial x_i}=\rho g_i+F_i-\frac{\partial p}{\partial x_i}+\frac{\partial}{\partial x_i}\left(2\mu S_{ij}\right) \tag{2.3}$$

$$\frac{\partial \rho E_o}{\partial t}+\frac{\partial \rho U_i E_o}{\partial x_i}=\rho U_i F_i+F_i-\frac{\partial q_i}{\partial x_i}+\frac{\partial}{\partial x_j}\left(U_i T_{ij}\right) \tag{2.4}$$

Where the indices (i) have three value 1, 2 and 3 which corresponding to 3 dimensions (for example: $\{x,y,z\}$for a Cartesian coordinate). The commercial Fluent CFD analysis utilizes the finite volume method to discretize the studied domain, and introduce new variable(s) to model the turbulence term. For the steady state k-ε viscous model, two new variables: k and dissipation rate, *ε* are introduced together with 2 turbulence transport equations. Further, according to Fluent the realizable k-ε with enhanced wall treatment has been proved to be a better predictor for both planar and round jets. Literature also proves that that realizable k-ε has shown substantial improvement over the standard *k-ε* models where there is complex secondary flow features in the flow field. Equation 2.5 and Equation 2.6, the two model transport equations to solve for k and ε in coupling with flow field and energy equations, are employed by Fluent software (Fluent, 2010)

$$\frac{\partial}{\partial t}(\rho k) + \frac{\partial}{\partial x_j}(\rho k u_j) = \frac{\partial}{\partial x_j}\left[\left(\mu + \frac{\mu_t}{\sigma_k}\right)\frac{\partial k}{\partial x_j}\right] + G_k + G_b - \rho\epsilon - Y_M + S_k \tag{2.5}$$

$$\frac{\partial}{\partial t}(\rho\epsilon) + \frac{\partial}{\partial x_j}(\rho\epsilon u_j) = \frac{\partial}{\partial x_j}\left[\left(\mu + \frac{\mu_t}{\sigma_\epsilon}\right)\frac{\partial \epsilon}{\partial x_j}\right] + \rho C_1 S\epsilon - \rho C_2 \frac{\epsilon^2}{k + \sqrt{\nu\epsilon}} + C_{1\epsilon}\frac{\epsilon}{k}C_{3\epsilon}G_b + S_\epsilon \tag{2.6}$$

where G_k represents the generation of turbulence kinetic energy due to the mean velocity gradients, and G_b is the generation of turbulence kinetic energy due to buoyancy, Y_M represents the contribution of the fluctuating dilatation in the compressible turbulence to the overall dissipation rate, S_k and S are source terms which is defined by users and ignored in this study, σ_k and σ_ε are the turbulent Prandtl numbers. C_2 and $C_{1\varepsilon}$ are constants and defined as in Equation 2.7, 2.8 and 2.9

$$C_1 = \max\left[0.43, \frac{\eta}{\eta + 5}\right] \tag{2.7}$$

and

$$\eta = S\frac{k}{\epsilon} \tag{2.8}$$

in which S is defined as:

$$S = \sqrt{2S_{ij}S_{ij}} \tag{2.9}$$

II.3 Design of Experiment

Experimental design, which deals with collection of data, was developed at about the same time as the analysis of variance, mainly by R. A. Fisher (Chiang, 2003). Scientific research depends on the quality of data collected. A good design is as essential to a successful study as a proper method of analysis. Corresponding to an observation in statistical analysis, there is an experimental unit in the design. An experimental unit is one on which a treatment is applied and an observation is made. The need for the experiment design is because of the variation among experimental units. The objective of an experimental design is to control the experimental variation by proper assignment of treatments to experimental units. The method of assigning treatments to experimental units is the design of the experiment. Generally, experimental variations can be classified into two categories: systematic and random variations or factors (Figure 18). They are:

> *Systematic factors*: is associated with a specific factor, or factors in the study, usually can be controlled or subject to a statistical test.

Random factors: generally cannot be controlled and some may not even be detected before an experiment is performed. It is principally due to the innate difference among experimental units.

There are several types of design for an experiment (Montgomery, 2001): randomized complete block designs, Latin square designs, Graeco-Latin square designs, balanced incomplete block designs, factorial designs (general factorial design, 2^k factorial design, high-level and mixed-level factorial design) and response surface methodology.

Response surface methodology is a quite powerful tool in term of robust features and cost effectiveness. Taguchi, central composite design and Box Behnken are three major designs in the response surface methodology branch of design of experiment technique. For example, one is studying four factors: injection angle (A), blowing ratio (B), L/D ratio (C) and density ratio (D). Each factor has three levels of variation. The full design matrix would look like in the Figure 19. Number of tests or runs for full factorial design, central composite design, Taguchi and Box Behnken are given in Table 2.

Table 2 Number of runs for several statistical designs

Design Matrix	Number of Runs	Advantage | Disadvantage
Full Factorial Design, $3^{k=4}$	$3^4 = 81$	Precise but extremely expensive
Taguchi Design Method	Vary	Quite creative in the 1970s. It has been recently competed by the other methods developed by mathematicians and statisticians (using response surface methodology (RSM))
Central Composite Design	$24 + n_{\text{central runs}}$	Great design matrix, but it requires more than 1 central runs
Box- Behnken Design	$24 + 1_{\text{central run}}$	Creative design matrix and has been proved of robust and precise (require >=1 central run)

By using a classical full factorial $3^{k=4}$ design, we will need to run an excessive number of design points which is impractical. That would also cost a lot of time and is definitely a very inefficient way of studying of parameters. Central Composite Design (CCD) would be an ideal selection since it does not required knowledge of safety operation zone (known safety range of each factor). With the CCD, one can reduce the number of runs from 81 down to 16, but one needs to have two or more replicates for the axial point (central point). Unfortunately, with a numerical simulation tool, we can not generate more than one result for any specific problem. Fortunately, as we can see that Box Behnken is fit for the numerical simulation approach since it only requires a single run for the central run. Box Behnken design matrix which is actually a very creative design matrix, is invented by Box and Behnken in 1960, (Myers et al., 2009). This design is used for studying second-order response surfaces which is based on the balanced incomplete block designs. In other words, Box-Behnken design matrix is an alternative tool to study four involved factors which each one have three levels of fluctuation.

Figures

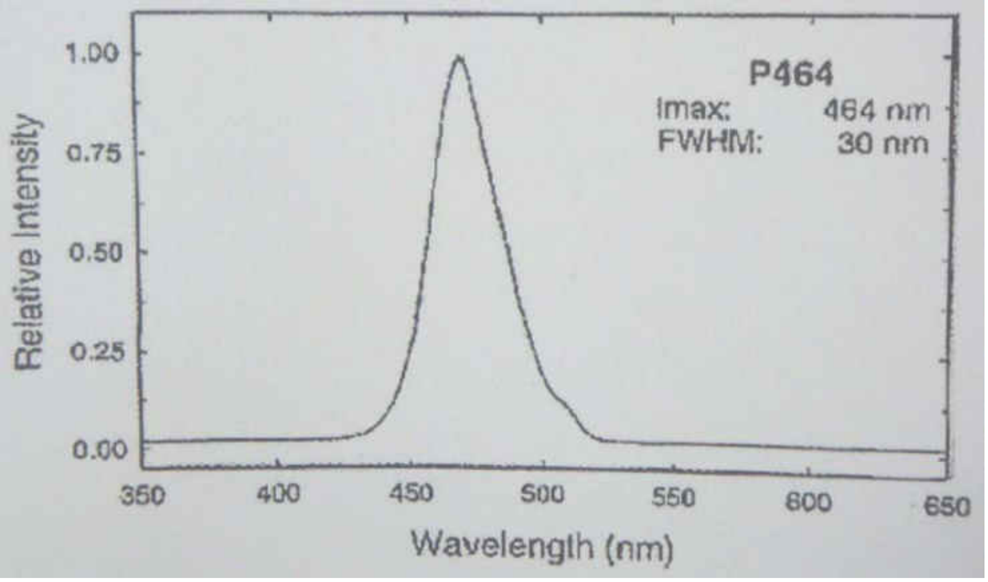

Figure 12 Peak Intensity Occur at λ=464nm (Liu, 2006)

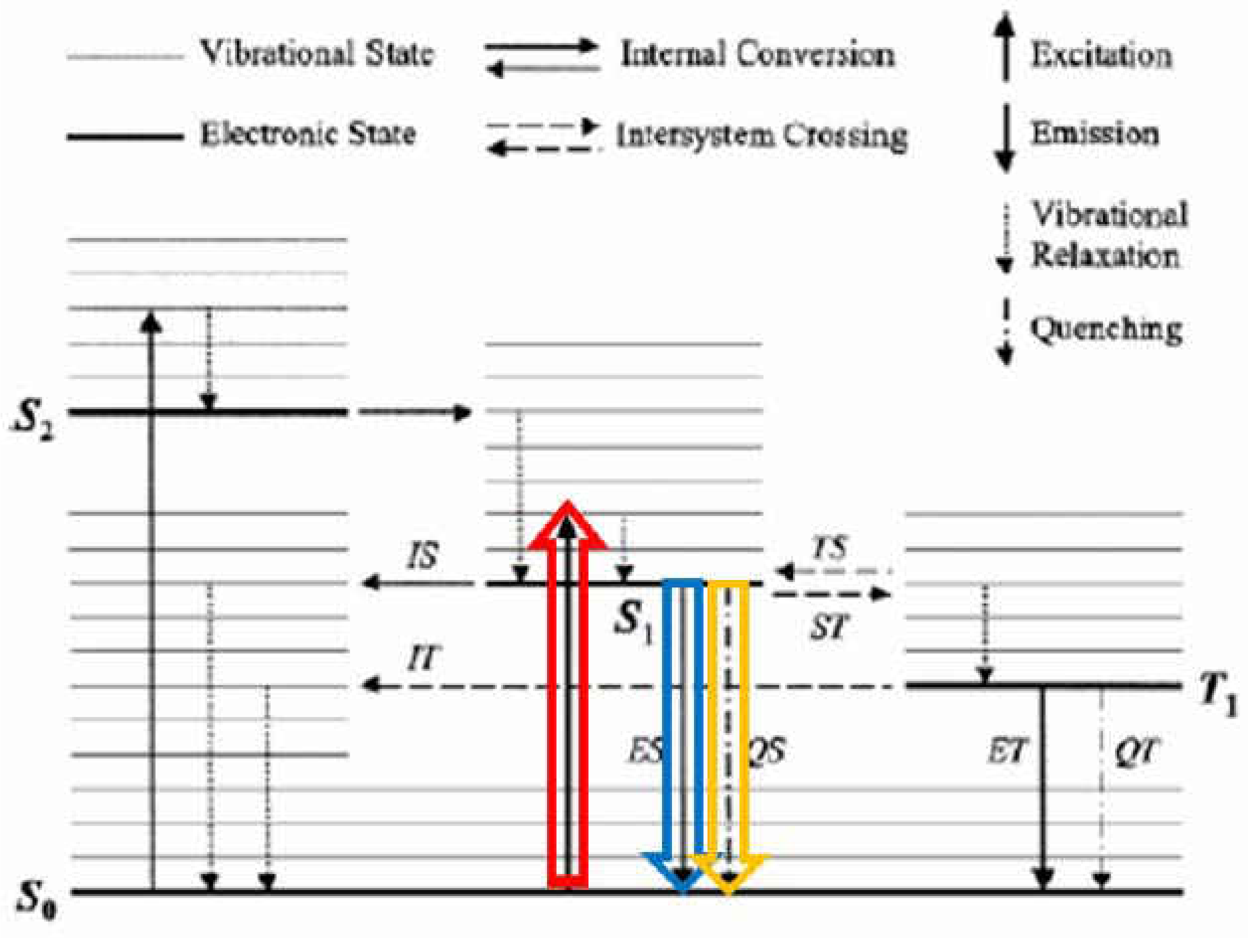

Figure 13 Diagram of Jablonski Energy Level (Adapted from Ricklick, 2009)

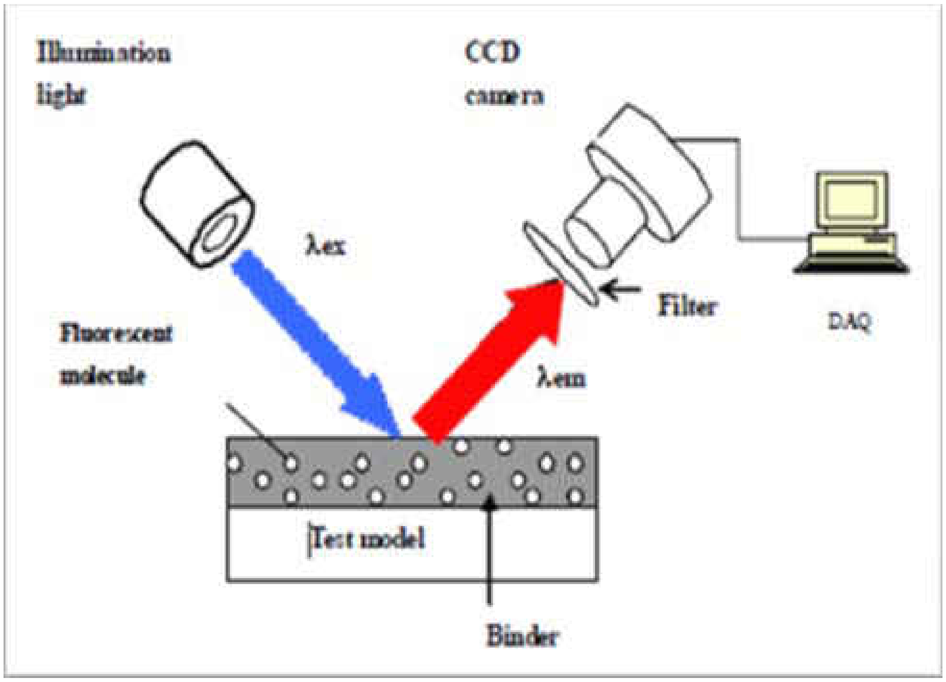

Figure 14 Typical TSP Test set-up (Adapted from Liu, 2006)

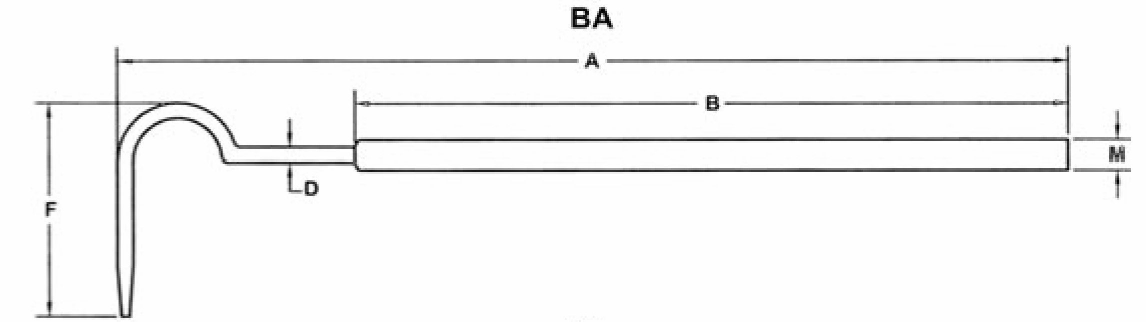

Figure 15 A Typical Boundary Layer Probe

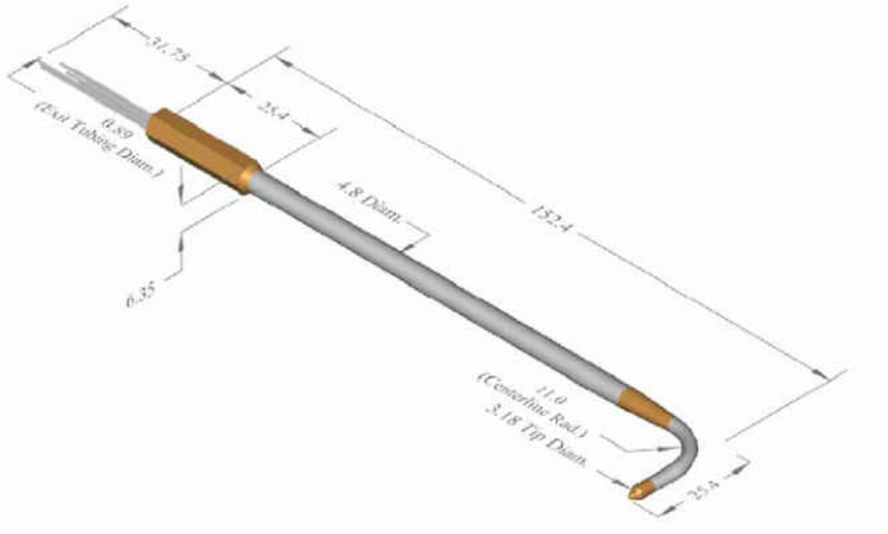

Probe tip diameter: 3.18mm
Neck: 25.4mm
Neck (central line) radius: 11.0mm
Body length: 152.4mm
Body diameter: 4.8mm

Figure 16 The L-shaped Conical Tip FHP Used for This Study (Unit: mm)

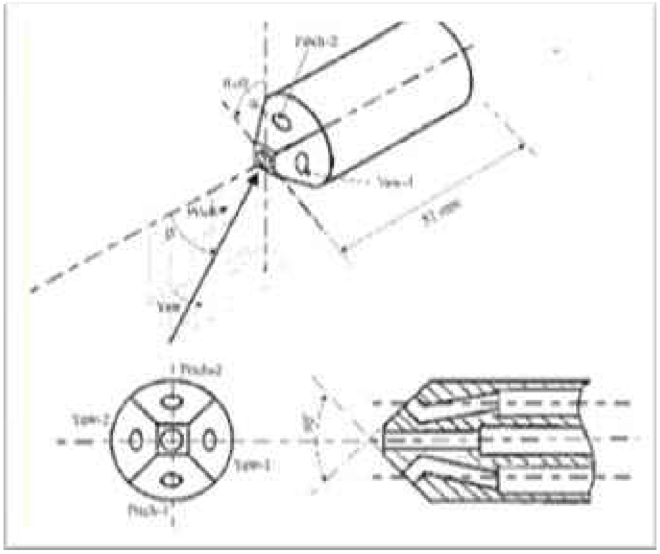

Figure 17 Distribution of The Holes on The FHP Tip

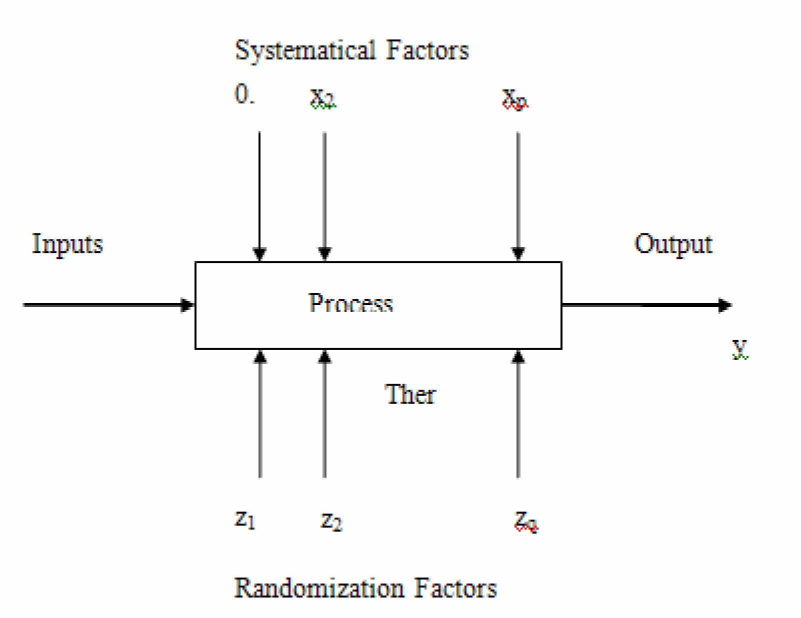

Figure 18 General Model of a Process or System (Montgomery, 2001)

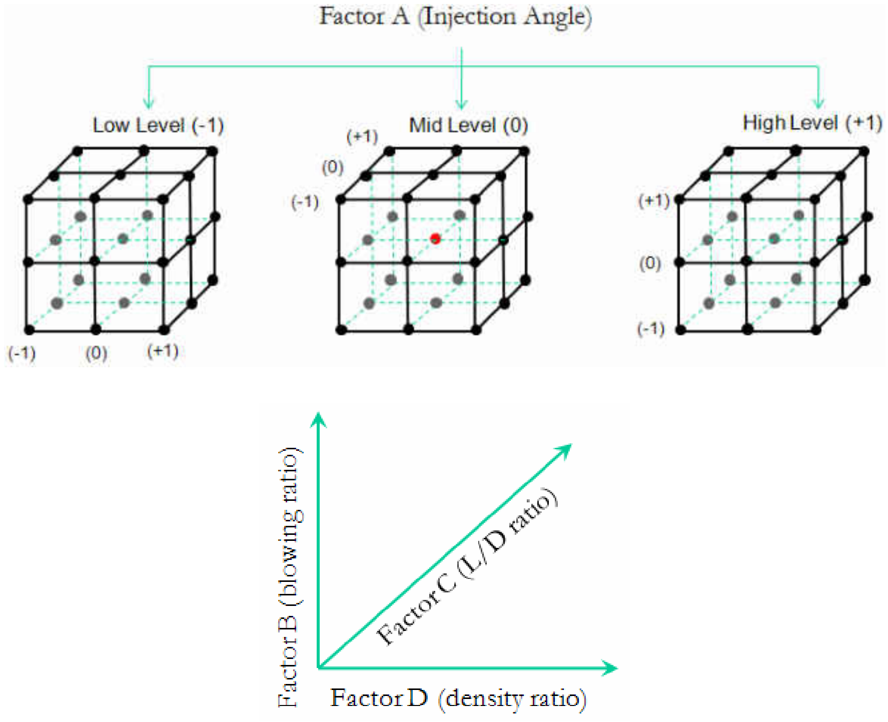

Figure 19 Diagram of Total Run for Four Factors at Three Levels

CHAPTER III. FILM COOLING ON FLAT PLATE: CFD VALIDATED AGAINST BFC TESTS

Film cooling technology deployed inside complex geometries of gas turbine engines is initially studied on a flat surface with zero pressure gradients (a simple flat plate). One can easily investigate the cooling performance of injecting coolant onto a flat surface, and withdraw preliminary conclusions and trends before conducting a detailed investigation on more complex and realistic geometries. A conjugated heat transfer numerical solution will be validated using experiments and literature on the conical-shaped film hole and trenched cylindrical-shaped hole. Benchmarking between different flare conical angles and baseline cylindrical film holes will be performed and conclusions will be drawn in this chapter.

III.1 Basic Film Cooling Test Rig

The subsonic wind tunnel in the CATER lab was built and employed since 2003. It includes a relatively hot main flow loop and a coolant supply system. The hot main loop is a vertical closed-loop duct with 0.15 Mach number at the test section. The main module is composed by three main components: blower, casings and flow conditioner, and test section as shown in the Figure 20.

The main loop employs a 15 kW blower, which supplies a volumetric flow rate up to 5m^3/s (which yields a freestream velocity of 52 m/s at the test-section cross section). It takes between 2 to 3 hours so that the free-stream air can heat up to 68 °C. This provides enough time for all wind tunnel walls reach the same temperature of the mainstream flow. This is verified by thermocouple measurements which are installed on the wind tunnel walls as well as in the freestream.

Immediately downstream of the blower is the flow conditioning section, which consists of a honeycomb and three screens. The tunnel, at this point, has a cross-section 0.45 m in height and 0.53 m in width. The honeycomb screen has a thickness of ½" and is followed by three screen-meshes spaced at 0.09 m intervals. Following the screens is the start of the 2D contraction nozzle. The area of contraction of this nozzle is from a cross-section height of 0.45 m to 0.17 m, over a length of 0.74 m (keeping the cross-sectional width unchanged).

The exit of the nozzle leads to the test section, which is made of an acrylic plate of ½" (or 12.7 mm) thickness. The transparent test section has a LxWxH dimension of 1.20mx0.53mx0.15 m. The top panel is removable for accessibility, and is sealed while conducting the experiment. On the top of the test section, there is a circular 10" diameter annealed glass which serves as a window for the CCD camera to capture the TSP image with a highest available clarity quality. Detail of the wind tunnel can be found in Zuniga (2007). Note that the test surface at the downstream surface where TSP was applied was replaced by balsa wood to reduce the thermal conductivity errors which were associated with the Plexiglas test section (Figure 21a).

Figure 21b and Figure 21d show a typical test coupon of 3.5inx1.5inx0.25 in (LxWxH) which has a row of cylindrical film holes embedded in a 0.75D-depth trench. This trenched-cylindrical film hole coupon was printed using rapid prototyping Stereolithography (SLA) method. The coupon geometrical configurations and wind tunnel operating conditions are listed in Table 3.

Table 3 The Typical Coupon Geometrical Configurations and Wind Tunnel Conditions

Hole Geometrical Parameters	
Coolant hole shape	Trenched Cylinder
D [in | m]	0.0783 | 2E-3
p/D	3.5
s/D	0.8
L/D	7.8
α [degree]	35
Main Flow Condition	
T_m [^{o}C | K]	67 | 340
P_{t_inlet} [Pa]	102,527
P_{s_inlet} [Pa]	101,118
P_{s_outlet} [Pa]	101,118
Coolant Flow Condition	
T_c [^{o}C | K]	-16 | 258
DR	1.263
Coolant stream mass flow rate, m [kg/s]	8.45e-5

The uncertainty in the calculation of the blowing ratios is estimated to be less than 1% over the range of investigations. The adiabatic wall temperature values obtained with TSP were used to calculate effectiveness values in each case. The uncertainty in the effectiveness values was on an average less than 3%, while the highest value were calculated to be less than 9%. The uncertainties reported were estimated following the procedure described by Kline and McClintock (1953).

III.2 Variety of Film Cooling Design

III.2.1 Round-hole Film Cooling versus Shaped Hole (Conical vs Cylindrical)

It has been known that the cylindrical-shaped film holes are usually machined by several different methods (water jet, electro-discharge, and/or laser machining method) as mentioned in Pepe and Illision (2004). Unfortunately, due to manufacturing defects, conical-shaped holes are usually obtained rather than perfect cylindrical-shaped ones. However, conical-shaped holes actually help to reduce the penetration of the coolant jet into the mainstream as concludes in the work of Zuniga (2007). Zuniga found that the coolant jets stay close to the downstream solid surface, resulting in a better uniformity of the coolant blanket over the surface. This uniformity reduces the heat transfer between the mainstream and the solid wall and hence also reduce thermal stresses (Bunker, 2001). It is clear that conical-shaped film cooling data is very limited in the open literature. The authors would like to conduct a study on the performance of conical-shaped holes in film cooling both numerically and experimentally. In the conjugate heat transfer numerical analysis, both fluid and solid zones are modeled in order to take into the account the effect of conduction errors which are associated with the ideal adiabatic wall assumption used in most of the numerical approaches in open literature.

Figure 22 depicts cylindrical-shaped film hole (CYL) and conical-shaped hole (CON) coupons with typical geometric parameters. A conical-shaped film hole has its cross section area expanded from inlet to exit around its centerline.

III.2.2 Traverse Slot (Trench vs. No Trench)

Slot or trenched film cooling provides a continuous and uniform protection blanket to the downstream application area. Although it seems to be an ideal configuration, it weakens the structure at the high combustion temperatures of modern gas turbine engines. This issue with slot film cooling can be avoided by employing a continuous trench imposed on the top of row of discrete film cooling holes shown in Figure 23. In 2001, Bunker et al. (2001) introduced trenched film cooling with thermal barrier coating (TBC), in which a trench is cratered on a row of discrete film cooling holes. Trenches were actually first introduced by Tabbita et al. (2001). This method actually had a big impact in gas turbine film cooling technology, because it helps the coolant flow spread out more onto the downstream area. Thus, this method improves film cooling in gas turbine engines without weakening the structure since its depth is the thickness of the TBC layer, without removing any metal material of the hub or the casing walls.

III.3 CFD Validated against BFC Test - Cylindrical versus Conical Shaped Film Hole

This section will introduce both the experimental set up on the wind tunnel inside the CATER lab and the details of the conjugate heat transfer (CHT) numerical simulation.

III.3.1 Experimental Set Up and Solutions

A cylindrical-shaped test coupon, CYL, and two conical-shaped coupons, CON3 and CON6, were tested. The tests were performed in a subsonic wind tunnel which was built and dedicated to the study of film cooling at the CATER facility. Cold nitrogen gas at –12 ± 1.5 °C was used as the coolant in these experiments. The temperature of the coolant was controlled to a fixed density ratio of 1.26 for all the cases. The plenum contained a perforated plate to break up the jet and promote mixing inside the plenum. The test section was made out of a 0.5 in (12.7 mm) section of balsa wood with thermal conductivity of 0.05 $Wm^{-1}K^{-1}$. This balsa wood was covered with a thin layer of Kapton tape to provide a smooth surface without increasing the thermal conductivity of the test section. The balsa-wood test section rendered a nearly ideal adiabatic condition during the tests. Adiabatic wall temperature distribution measurements immediately downstream of the test coupon were made with temperature sensitive paint (TSP). Typical TSP test setup and data reduction procedures are shown in Figure 24. Measurements are taken once the tunnel attains steady state, which was defined by a rise in the mainstream temperature of 0.1°C or less, over 10 minutes (while radiation loss is reasonably neglected in this experimental investigation). Conduction loss associated with Plexiglas is quite small and is also neglected. The TSP paint was previously calibrated in a separate chamber. Table 4 is the summary of all parameters for the cylindrical film hole (baseline, CYL) and conical-shaped film holes at 3^o and 6^o (CON3 and CON6).

Table 4 Coupons and Testing Experimental Conditions

Parameters / Shape hole	CYL	CON3 & CON6
Geometric parameters:		
Diameter, D	3	3
Blowing ratio, BR	0.5, 1.0, 1.5	0.5, 1.0, 1.5
Density ratio, DR	1.26	1.26
Pitch-to-diameter ratio, p/D	3	3
Inclination angle, α [degree]	30	30
Hole length-to-diameter ratio, L/D	4.3	4.3
Flow parameters:		
Mainstream temperature, T_m	340	340
Coolant temperature, T_c	260	260
Mainstream total pressure, P_{t_inlet}	101,820	101,820
Mainstream pressure, P_{s_inlet} [Pa]	100,475	100,475
Flared/diffused angle, γ [^{o}]	0	3 and 6

The uncertainty in the calculation of the blowing ratios is estimated to be less than 1% over the range tested/studied in the experiments. The adiabatic wall temperature values obtained with TSP were used to calculate effectiveness values in each case. The estimated uncertainty in temperature measurements using TSP is ± 1°C. Average effectiveness was calculated between the centerline streamlines of selected film holes. Two cases were chosen to represent low and high *BR*s corresponding to 1.0 and 1.5. Results showed that a decrease in blowing ratio is accompanied by a increase in uncertainty in the discharge coefficient. Also, the uncertainty in the effectiveness values was on average less than 5%, while the highest value was calculated to be less than 10%. All the reported uncertainties were estimated following the procedure described by Kline and McClintock (1953).

III.3.2 Flow Test and Discharge Coefficient Data

Flow tests were performed to determine the effective area of any film cooling holes, and the discharge coefficient (C_d) is defined as the ratio of the actual amount of coolant (which goes through a hole) to the amount of the ideal coolant (predicted by the ideal compressible flow equation). It has been known that this ratio is less than 1, since real fluid flows exhibit a vena contracta. The vena contracta, in effect, restricts the amount of fluid passing through a geometry (in this case a cylindrical-shaped hole inlet) and makes the fluid behave as if it is going through a smaller opening. Once the discharge coefficients were obtained for each testing configuration, the next step was to use this obtained data to extract the *PR*s for the N_2 tests that yield the desired blowing ratios (*BR*s) in the film cooling tests. The data was then processed with the relation in Equation 3.1. Figure 25 shows discharge coefficient curves for CYL, CON3 and CON6.

$$\mathrm{Cd} = \frac{\dfrac{\dot{\mathrm{m}}_{\mathrm{a}}}{\mathrm{N}}}{\left(\dfrac{\pi}{4}\mathrm{D}^2\right)\mathrm{P_c}\left(\dfrac{\mathrm{P_m}}{\mathrm{P_c}}\right)^{\frac{\gamma+1}{2\gamma}}\sqrt{\dfrac{2\gamma}{\gamma-1}\dfrac{1}{\mathrm{RT_c}}\left[\left(\dfrac{\mathrm{P_c}}{\mathrm{P_m}}\right)^{\frac{\gamma-1}{\gamma}}-1\right]}} \tag{3.1}$$

III.3.3 Film Cooling Effectiveness

Blowing ratios of 1.0 and 1.5 were selected for the experimental testing on CYL, CON3 and CON6 coupons. From the temperature distribution on the downstream surface, obtained from the TSP analysis, FCE distribution were calculated by using Equation 2.9: where T_c is the coolant exit temperature, T_r is the recovery temperature which is measured on the downstream surface which is not affected by the coolant jet, and T_m is the hot mainstream temperature and is measured by Omega handheld thermometer (thermocouple reader). FCE is plotted in Figure 26. Spanwise-averaged FCE curves were also extracted from the temperature distribution by using Equation 2.10.

III.3.4 Computational Modeling and Solutions

Grid structure and turbulence model:

The 3-Dimensional conjugate model used in numerical analysis (Figure 27) was formed to imitate the realistic conditions of the experimental testing facility. Both cylindrical and conical geometries were constructed in completely hexahedral topologies (Figure 28). The GAMBIT (2009) mesh generation software was utilized in the creation of all meshes. For both cylindrical and conical-shaped hole coupons, a nominal diameter of D=3 mm was set at the coolant holes entrance with an inclination angle of 30°. The expansion angle of the conical hole was 3°, analogous to the CON3 configuration. The pitch *p* was 3 diameters and the length of the coolant holes *L* was 4.3 diameters in both cases.

The space considered in the meshed model included 25 diameters upstream of the hole, in order to allow the boundary layer to develop, and 50 diameters downstream of the hole, in order to capture temperature data up to x/D=50. In order to limit the needed size of the mesh, a symmetry boundary condition was applied 8.5 diameters above the surface. At the no-slip walls, dimensionless wall distance $y+$ values less than 20 were used to set the boundary layer mesh size. Only one half-pitch was modeled, with symmetric boundary conditions on both sides in the lateral *y* direction.

At the inlet and outlet for the hot mainstream, a pressure boundary condition was set to imitate the actual experimental operating conditions. The pressure at the inlet to the coolant plenum was then set in order to produce the desired blowing ratios. Incompressible air was used for both the hot mainstream and coolant flows, resulting in a fixed density ratio of 1. The temperatures of the mainstream and coolant inlets were 340 K and 260 K, respectively. The upstream wall consisted of acrylic (k=0.2 $\mathrm{Wm^{-1}K^{-1}}$) and the downstream 'adiabatic wall' surface was modeled after balsa wood (k=0.05 $\mathrm{Wm^{-1}K^{-1}}$). A steel plate was inserted underneath both the upstream and downstream surfaces. The coupon containing the coolant holes which was set to k = 0.2 $\mathrm{Wm^{-1}K^{-1}}$. For the sake of comparison, all geometric parameters of the coupons are kept the same in the numerical model. Material properties and boundary conditions are listed in Table 5.

The meshed model, which was obtained from Gambit (2009), was imported into Fluent (2009) for the flow solution. The realizable k-ε (RKE) turbulence model was employed. The inlet turbulent kinetic energy and dissipation rate were calculated from the hydraulic diameter of the model and estimated turbulence intensity. Enhanced wall treatment was also used, since the main temperature measurements for the problem were along the downstream wall.

Rodriguez (2008) studied the comparison between different schemes and found that RKE is a better predictor of film cooling effectiveness (Figure 29). Literature has also shown that standard *k-ω* may over-predict the diffusion of jets, which explains the high effectiveness value at higher *x*/*D*. For this reason, the authors employed RKE model as a turbulence model for predicting film cooling effectiveness for the current numerical study for this conical-shaped film cooling performance investigation.

Table 5 Material properties and boundary conditions

Parameters / Shape hole	Cylindrical (CYL)	Conical (CON)
Thermal conductivities, $Wm^{-1}K^{-1}$		
Balsa wood	0.05	0.05
SLA coupon	0.2	0.2
Plexiglas wall	0.2	0.2
Metal	17	17
Blowing ratio, *BR*	0.75, 1.0, 1.5	1.0, 1.5
Density ratio, *DR*	1	1
Mainstream temperature, T_m [K]	340	340
Cool-stream temperature, T_c [K]	260	260
Mainstream total pressure, P_{t_inlet} [Pa]	102,303	102,303
Mainstream pressure, P_{s_inlet} [Pa]	100,450	100,450

Grid study and solution process:

For both cylindrical and conical shaped models, grid convergence studies were performed over five mesh sizes, from 100,000 to 500,000 elements. The different mesh sizes were generated by systematically refining the size of the individual elements in the fluid zones of the model. Figures 30a and 30b show surface temperature values over the different mesh sizes at three downstream set points for cylindrical and conical-shaped hole geometries. Temperature change between grid sizes at the points analyzed was less than 1 K after 300,000 volumes. Therefore, all of the following solutions were obtained from meshes of this size.

The solution was obtained using the Reynolds Averaged Navier Stokes coupled with the realizable k-ε turbulence model with enhanced wall treatment. Convergence was set with a residual criterion of 1E-6. Iterative convergence was also monitored for the mass flow at the mainstream outlet and the temperature at the points specified in the grid independence study above. After obtaining a converged solution, global mass and energy conservation equations were applied at the macroscopic level. The errors in mass conservation were found to be many orders of magnitude below the mass flow rate of the coolant inlet. Similarly, the errors in energy conservation were verified to less than 1% of the coolant mass and energy flows (less than 0.5 % in most cases). The noticeably higher error in overall energy balance is due to the added complexity of the conjugation. Temperature and mass flow data was extracted and analyzed for the 300,000 cell grids, according to the findings of the grid study.

After obtaining a converged solution, the blowing ratio was verified and the temperature data was extracted from the downstream (balsa wood) wall and inserted into Equation 1, 2 and 3. The discharge coefficient was also calculated using Equation 3.1. For further analysis, the cooling uniformity coefficient, which express how uniform the temperature distribution is on the downstream surface. CUC (or laterally-averaged CUC) and spatially-averaged CUC are calculated for each *x/D* and the entire downstream area using Equation 3.2 and Equation 3.3 repectivelly.

$$CUC(x) = 1 - \frac{\left| \eta_{CL}(x) - \bar{\eta}(x) \right|}{\eta_{CL}(x)} \tag{3.2}$$

$$\overline{\overline{CUC}} = \frac{\int CUC(x)\,dx}{\int dx} \tag{3.3}$$

Numerical Model Validation:

Again, the current computational fluid dynamic study (CFD) takes into consideration the fluid domains as well as all relevant solid zones in order to reduce the thermal conductivity error associated with a non-conjugate simulation. Figure 31 demonstrates comparison between the conjugate heat transfer model versus non-conjugate heat transfer for both cylindrical film holes as well as conical-shaped film holes. From there, it can be seen that laterally averaged FCE will be lower than the non-conjugate model. This is an important result that shows that the CHT model helps reduce the over-prediction in FCE of the centerline, which is usually seen in any numerical analysis when compared to the corresponding experimental data.

It is interesting to note the agreement between experimental and numerical discharge coefficients. Figure 32 contains a discharge curve obtained from three numerical runs (three blowing ratios: 0.5, 1.0 and 1.5) compared with in-house experimental data as well as data taken from Taslim and Ugarte (2004). All of the coupon configurations used in the discharge coefficient C_d comparison are summarized in Table 6 for convenience purpose. It can be seen that numerical and experimental data for the C_d are closely related. The similarity between the two adds confidence to the numerical solution. C_d data from Taslim and Ugarte (2004) has higher values than CON3 data because their area ratios (ratio between the cross section area at the exit and the cross section area at the inlet) are much larger and *L/D* is much shorter than the current investigation (2.54 versus 5.0). Therefore the conical effect is enhanced and produces a difference of up to 25 % (Figure 32).

Finally, in terms of laterally-averaged FCE, Figures 33a and 33b were created to validate the conjugate CFD model against the in-house experimental data as well as data from Waye and Bogard (2006).

Table 6 Summary of all case Configurations for Cd Comparison Validation

Parameter / Cases	CON3	Taslim & Ugarte (12)
D_{inlet} [mm]	3	3.76
L/D_{inlet}	5	2.54
α [^{o}]	30	30
γ [^{o}]	3	7

III.3.4 Cylindrical and Conical-Shaped Film Hole Comparison Using CHT-CFD Model

Center Line FCE:

Figure 34 presents the centerline effectiveness versus x/D for all nine main numerical test cases. At all three blowing ratios (0.5, 1.0 and 1.5), conical-shaped holes clearly outperform their cylindrical equivalents. For the CYL and CON3 geometries, the lowest blowing ratio starts with the highest centerline effectiveness at 5 diameters downstream. Here, the blowing ratio has an inverse relationship with effectiveness. As it progresses further downstream, for the CON3 and CON6, the three curves cross and the highest blowing ratio ends up with the highest effectiveness. Toward the end of the sampled data in each case, an increase in blowing ratio leads to an increase in effectiveness, which is opposite of the trend at lower x/D values. At the lowest BR (0.5), the effectiveness for all 3 geometries (CYL, CON3 and CON6) converges as x/D increases. This is due to the small amount of coolant which doesn't have much momentum and is easily washed out into the mainstream. At the highest BR (1.5), one can easily note that CON6 performs better than CON3, and these two also perform better than CYL for entire $5<x/D<45$. The same trend was seen for the middle level of BR (1.0) in all three geometries.

Laterally And Spatially Averaged FCE:

Likewise, Figure 35a presents laterally-averaged effectiveness results for the three blowing ratios, both cylindrical and conical geometries. The results follow the same trends as the centerline results above. Once again, the lowest *BR* shows a similar effectiveness further downstream regardless of hole geometry. It is interesting to note that for CYL *BR* = 1.5, the effect of jet lift-off and gradual re-attachment is evident in the increasing of FCE further downstream.

For comparison, the spatially-averaged effectiveness for the nine cases is plotted in Figure 35b. For CYL, the lowest blowing ratio performs the best. For conical geometries, however, the middle blowing ratio performs the best while the lowest blowing ration performs the worst.

Laterally And Spatially Averaged CUC:

Effectiveness is not the only important parameter for judging the performance of a film cooling system. The uniformity of cooling, which is studied quantitatively by means of the CUC, should also be considered. Figure 36a shows CUC vs. *x/D* for the nine numerical test cases. There is a general upward trend of the CUC as the jets spread out in the main flow. Once again, conical outperforms cylindrical, except for the highest blowing ratio, which is by far the worst of the nine cases in effectiveness.

For a more comprehensive look at uniformity, the CUC data for *x/D* from 5 to 45 has been averaged to collapse all the data into nine points, representing a spatially averaged uniformity seen in Figure 36b. It is seen that there is a general trend of decreasing uniformity as *BR* increases, except in the cylindrical case of lift-off at the highest blowing ratio.

III.3.5 Summary and Conclusions

Two conical-shaped film holes, CON3 and CON6, with a diffusion angle γ of 3^o and 6^o respectively, were investigated both experimentally and numerically. Provided the same nominal diameter, higher discharge coefficients were found on conical-shaped holes compared to cylindrical-shaped holes due to the weakening of the vena contracta effect for the flared hole. The discharge coefficient tends to be proportional to the diffusion angle (at least for γ ranges from 0^o up to 6^o).

Spanwise-averaged FCE of cylindrical-shaped holes decreases with an increase in the *BR* due to the inability of the coolant jet to fully reattach in downstream region; this is not the case for the conical hole. The spanwise-averaged FCE reaches its maximum at a *BR* of 1.0 and minimum at the low value of *BR* (0.5). In general, conical-shaped holes always perform better than cylindrical-shaped ones in terms of spanwise-averaged FCE. This is a result of the lateral spreading of the coolant jet momentum, thus reducing its vertical penetration into the mainstream which helps to keep the coolant “blanket” attached to the downstream surface. It is important to note that spanwise-averaged FCE gains its maximum value at the medium-level *BR* (1.0), while cylinder-shaped hole gains its max spanwise-averaged FCE at low-level *BR* (0.5).

Superior performance of the conical-shaped hole over the cylindrical-shaped one is also reflected in the spatially-averaged FCE (Figure 35b). Again, the middle *BR* (1.0) will generate the best film effectiveness and the lowest *BR* (0.5) produces the worst film cooling performance.

To obtain an overall picture of conical-shaped film hole performance, CUC was also considered. The lower-level of *BR* gave the best uniformity, in terms of both CUC and spatial-averaged CUC as seen in Figure 36a and 36b. Again, the conical-shaped film holes performed better than cylindrical-shaped film hole in both effectiveness and temperature uniformity on the downstream surface.

III.4 CFD Validated against BFC Test - Trenched versus No-trenched Film Cooling

III.4.1 The trench coupon test:

The coupon configuration and test conditions are listed in Table 7. The uncertainty in the calculation of the blowing ratios is estimated to be less than 1% over the range of investigations. The adiabatic wall temperature values obtained with TSP were used to calculate effectiveness values in each case. The uncertainty in the effectiveness values was on an average less than 3%, while the highest value were calculated to be less than 9%. The uncertainties reported were estimated following the procedure described by Kline and McClintock (1953) as stated previously

Table 7 The Experiment Parameters

Hole Geometrical Parameters	
Coolant hole shape	Trenched Cylinder
D [in | m]	0.0783 | 2E-3
p/D	3.5
s/D	0.8
L/D	7.8
α [degree]	35
Main Flow Condition	
T_m [^{o}C | K]	67 | 340
P_{t_inlet} [Pa]	102,527
P_{s_inlet} [Pa]	101,118
P_{s_outlet} [Pa]	101,118
Coolant Flow Condition	
T_c [^{o}C | K]	-16 | 258
DR	1.263
Coolant stream mass flow rate, m [kg/s]	8.45e-5

III.4.2 Experimental results:

From the temperature distribution obtained by the TSP technique, an adiabatic-wall film cooling effectiveness is then generated using Equation 2.9, where T_c is the coolant temperature, T_r is the recovery temperature of the free stream and T_{aw} is the temperature on the surface at the downstream area of the end wall. Figure 38 depicts typical effectiveness distribution on the downstream area for four blowing ratios. It is common to many other experimental data which there are discrepancies due to control leakage, surface roughness, plenum of the coolant, leakage, etc. That is the reasons which the right hole has slightly better performance than the left hole as seen in the Figure 37. The uncertainty of all experimental results of film cooling effectiveness is less than or equal to 5%.

III.4.3 Computational modeling and solution - the numerical CHT model:

The 3D conjugate-heat-transfer (CHT) model used in this sensitivity analysis was built to imitate the actual conditions of the experimental testing facility. The GAMBIT mesh generation software was utilized to create a mesh using all hexahedral topologies. The coolant hole entrance had an inclination angle of 35°. The space considered in the meshed model included 25 diameters upstream of the hole, in order to allow the boundary layer to develop, and 50 diameters downstream of the hole, in order to capture temperature data up to x/d=50. In order to limit the needed size of the mesh, a symmetry boundary condition was applied 8.5 diameters above the surface. At the no-slip walls, y^+ values less than unity were used to set the boundary layer mesh size. Only the one half-pitch was modeled, with symmetric boundary conditions on both sides in the lateral direction.

At the inlet and outlet for the hot mainstream, a pressure boundary condition was set to imitate the actual experimental operating conditions. The pressure at the inlet to the coolant plenum was then set in order to produce the desired blowing ratios. The temperatures of the mainstream and coolant inlets were 340 K and 258 K, respectively. The upstream wall consisted of acrylic and the downstream 'adiabatic wall' surface was modeled after balsa wood.

III.4.4 Computational Modeling and Solution - The Grid Independence Study:

A grid convergence study was performed over six mesh sizes, from 100,000 to 600,000 volumes. The different mesh sizes were generated by systematically refining the size of the individual elements in the fluid zones of the model. Figures 38 shows temperature values over the different mesh sizes at four set points. Curve "x/D= 20" show the averaged temperature value of the surface at the distance "x/D" of 20 after the cooling holes. Same for "x/D= 40" and "x/D= 60". Temperature change between grid sizes at the points of "x/D" analyzed was less than 1 K after the 300,000-volumes model. Therefore, all of the later solutions in this study were obtained from meshes of 302,534 hexahedral cells and typical mesh structure is shown in Figure 39. The meshed model was imported into Fluent (2009) for flow analysis which takes about 5-6 hours per run to get convergence down to less than at least to 1e-6.

The literature has shown that standard k-ω numerical viscous model (SKW) may over-predict the diffusion of jets, which explained the high effectiveness value at higher *x/D*. For this reason, the authors decided to employ RKE model as a turbulence viscous model for predicting film cooling effectiveness for the current numerical study of the sensitivity design. Figure 40 shows a typical temperature distribution.

III.4.5 Computational Modeling and Solution - Validation the Numerical Model:

To validate the 3D model, two typical numerical solutions (case 13 and case 14) were compared to the in-house experimental data as well as the literature. Since the cylindrical-trenched film hole performance may be governed by many parameters, appropriate data from literature was carefully selected. Case 17 from the work of Dorrington and Bogard (2007) and the second configuration from Waye and Bogard (2006) were chosen for this validation purpose. Details of all the cases are listed in Table 3. As seen in Figure 41, numerical data shows the same trend as the experiment results and Waye and Bogard (2006) data, which is that a higher BR will give a higher laterally-averaged FCE. It is also well known that numerical results sometimes overpredict the adiabatic film effectiveness when compared to the experimental. This is due to assumptions associated with numerical modeling. This explains why case 13 agrees with Waye and Bogard (2006) (BR = 0.5).

Table 8 The Experimental Configurations of Case 13 and Case 14

Parameters \ Source	Case 13	Case 14	In-house Experiment	Dorrington and Bogard (2007) (Case 17)	Waye and Bogard (2006) (Configuration 2)	
D [mm]	1.52		2	4.11	4.11	
p/D	4		3.5	2.78	2.78	
s/D	0.75		0.8	1	0.5	
L/D	7.5		7.8	6.7	5.7	
α [°]	35		35	30	30	
BR	0.5	1.0	0 1.0 1.5 2.0	1.0	0.5	1.0

The 17th case from Dorrington and Bogard (2007) has lower *p/D* which yields higher laterally-averaged film effectiveness at the same blowing ratio compared to the current case 14.

In terms of order of magnitude, the numerical curves are relatively correlated to the in-house experimental curves as well as literature. The authors were confident to proceed to the sensitivity analysis.

III.5 Sensitivity Analysis and Optimization for Trenched Film Cooling

Four factors (effects), which include the flow and geometrical parameters, were considered in this sensitivity study. Table 4 summarizes the ranges of those factors. They were also coded so that each factor has three levels: low/mid/high that corresponds to -1/0/+1 respectively by using Equation 3.2.

$$X_{\text{coded}} = \frac{X - \frac{X_{\max} + X_{\min}}{2}}{\frac{X_{\max} - X_{\min}}{2}} \tag{3.4}$$

The advantage of DOE analysis is the ability to study the nonlinear behavior of those factors on film performance which produce interesting results. At least 3 levels of each factor must be adopted. If the authors used the classical full factorial $3^{k=4}$ design, an excessive number of design points would need to be run which is impracticable and inefficient in terms of time consumption and truly an inefficient way of studying of parameters. Central Composite Design (CCD) would be better choice since it does not require knowledge of safety operation zone (known safety range of each factor). With CCD, the number of runs can be reduced from 81 down to 16, but at least two or more replicates are needed for the axial point (central point). Unfortunately, with the numerical simulation tool or any commercial CFD software, only one data point can be generated. There is another design that any numerical-based researcher can employ for their study, which is the Box-Behnken design.

III.5.1 The Box-Behnken design:

In 1960, Box and Behnken generated a very creative design matrix, known as Box-Behnken design (Myers et al., 2009). This design is used for studying second-order response surfaces which is based on the balanced incomplete block designs. In other words, the Box-Behnken design matrix is an alternative tool to study four involved factors which each one have three levels of fluctuation. In detail, the Box-Behnken matrix is given in Table 10.

III.5.2 Sensitivity analysis procedure:

Based on Table 10, 25 cases/runs are needed for the sensitivity analysis. In each case, the levels of each factor are also assigned accordingly. Again, Gambit (2009) and Fluent (2009) are utilized for generating temperature distributions on the downstream surface corresponding to every case. Equation 1 and 3 were used to extract 25 spatially-averaged FCE values. The results then were imported into statistical software for the sensitivity analysis, which will be discussed next.

III.5.3 Summary of results

Commercial software (Minitab, 2009)) was employed for the sensitivity analysis. Table 6 shows the coefficients of each factor in the regression equation. The contribution percentage of each factor is also generated. It is logical to assume that the 3-way and 4-way interaction factors are not statistically important. Again, to judge the performance of any particular film cooling configuration, the uniformity of the effectiveness, the laterally effectiveness and the spatially averaged film cooling effectiveness should be looked at. These relationships can be approximated and regressed as the following second order polynomial model, as shown in Equation 3.5.

Table 9 Input Variable Ranges

Studied Factors (Effects)	**Natural main factors**				**Coded main factors**			
	Symbols	**Low**	**Middle**	**High**	**Symbols**	**Low**	**Middle**	**High**
Pitch-to-diameter ratio, p/D	(*p/D*)	1.5	4	6.5	X_1 or (*p/D*)	-1	0	1
Trench depth-to-diameter,	(*s/D*)	0.1	0.55	1.0	X_2 or (*s/D*)	-1	0	1
Blowing ratio, BR	(*BR*)	0.5	1.0	1.5	X_3 or (*BR*)	-1	0	1
Density ratio, DR	(*DR*)	1.0	1.5	2.0	X_4 or (*DR*)	-1	0	1

Table 10 The Box-Behnken Design Matrix

Standard Order	**Coded Factors**				**FCE**
	X_1 or (*p/D*)	**X_2 or (*s/D*)**	**X_3 or (*BR*)**	**X_4 or (*DR*)**	
1	-1	-1	0	0	0.049
2	1	-1	0	0	0.587
3	-1	1	0	0	0.488
4	1	1	0	0	0.257
5	0	0	-1	-1	0.451
6	0	0	1	-1	0.131
7	0	0	-1	1	0.071
8	0	0	1	1	0.140
9	-1	0	0	-1	0.515
10	1	0	0	-1	0.314
11	-1	0	0	1	0.564
12	1	0	0	1	0.124
13	0	-1	-1	0	0.283
14	0	1	-1	0	0.359
15	0	-1	1	0	0.563
16	0	1	1	0	0.359
17	-1	0	-1	0	0.188
18	1	0	-1	0	0.212
19	-1	0	1	0	0.258
20	1	0	1	0	0.132
21	0	-1	0	-1	0.252
22	0	1	0	-1	0.169
23	0	-1	0	1	0.137
24	0	1	0	1	0.246
25	0	0	0	0	0.321

$$\bar{\bar{\eta}} = \beta_o + \left[\beta_1(p/D) + \beta_2(s/D) + \beta_3(BR) + \beta_4(DR)\right] + \begin{bmatrix}\beta_{11}(p/D)\times(p/D) + \beta_{22}(s/D)\times(s/D) + \\ \beta_{33}(BR)\times(BR) + \beta_{44}(DR)\times(DR)\end{bmatrix} + \begin{bmatrix}\beta_{12}(p/D)\times(s/D) + \beta_{13}(p/D)\times(BR) + \\ \beta_{14}(p/D)\times(DR) + \beta_{23}(s/D)\times(BR) + \\ \beta_{24}(s/D)\times(DR) + \beta_{34}(BR)\times(DR)\end{bmatrix} \tag{3.5}$$

The weight (absolute value) of the coefficient as shown in Table 11 indicates the importance of the corresponding factor. For example, factor (*p/D*) plays the most important role in the spatially-averaged film effectiveness (coefficient of -0.1639). In other words, it has the most contribution (around 25%) in deciding the performance of the film cooling.

Table 11 Percentage contribution of all factors to spatially-averaged FCE

Term	**Coefficients**		**Contribution [%]**
Constant	β_0	0.24522	
(p/D)	β_1	-0.16391	24.9
(s/D)	β_2	0.04454	6.8
(BR)	β_3	0.00254	0.4
(DR)	β_4	-0.03261	4.9
(p/D) (p/D)*	β_{11}	0.06378	9.7
(s/D) (s/D)*	β_{22}	-0.01009	1.5
(BR) (BR)*	β_{33}	-0.05570	8.5
(DR) (DR)*	β_{44}	0.02131	3.2
(p/D) (s/D)*	β_{12}	-0.02498	3.8
(p/D) (BR)*	β_{13}	-0.03846	5.8
(p/D) (DR)*	β_{14}	0.02429	3.7
(s/D) (BR)*	β_{23}	0.04384	6.7
(s/D) (DR)*	β_{24}	0.08491	12.9
(BR) (DR)*	β_{34}	0.04807	7.3
		SUMMATION	**100%**

It is interesting to study each main factor individually. Then, additional cases were run in order to plot those Figure 42.a to Figure 45.a. It is worth to note that the Figure 42.b was plot to study the factor *p/D*, where all other factors were kept at their middle level. The same token was performed for the Figure 43.b, 44.b and 45.b.

It can be seen from Figure 42, if one chose to set (*p/D*) at minimum level, it can help to bring spatially-averaged FCE up to 253% of the result obtained from (*p/D*) at maximum value. It seems so high that spatially-averaged FCE reaches 0.46 for *p/D* = 1.5 case. However, one should note here that the maximum value of laterally-averaged FCE must always equal to reciprocal of *p/D* ratio (in the case of non-trenched film cooling). Hence spatially-averaged FCE will be much smaller than the maximum value of laterally-averaged FCE. However, that rule is not applied where traverse slot exists across the row of film holes. Since there is the trench that forces the coolant flow to spread laterally onto two sides as soon as it hits the vertical wall of the trench. In other words, the maximum laterally-averaged FCE could be higher than *p/D*, and hence spatially-averaged FCE value could much higher that the one in the non-trenched film cooling. Again, as mentioned above, the higher value of *p/D* corresponds to the lesser spatially-averaged FCE since there is more area to cover. This is shown in Figure 42a where *p/D* is at high level at the top and *p/D* at low level in the bottom.

Figure 43 is designated for the second studied factor, (*s/D*). One can improve the performance of the trenched film cooling (from 0.2 up to 0.3, i.e. an increase of 50% in spatially-averaged film effectiveness) by increasing s/D from 0.1 to 1.0. This means that the deeper the trench, the better the film performance will be, since the coolant has had enough time to spread out laterally thus, forming a better blanket to cover the stream-wise area. It is important to note here about the non-linear behavior of spatially-averaged FCE with respect to *s/D*: for *s/D* from 0.1 to 0.55, the slope is stiffer than the one when *s/D* moves from 0.55 to 1.0 (Figure 43.b). This suggests that one can achieve a better improvement of film performance when increasing *s/D* from 0.1 to 0.55 than at the higher level. This result agrees with conclusions from Dorrington and Bogard (2006). In their study, they varied the trench depth at three levels (0.5*D*, 0.75*D*, and 1.0*D*) and found that the trench depth of 0.75*D* gave optimum film effectiveness, with little improvement in performance for trench depths greater than this. Figure 43.a also strongly supports this statement where we can see that the film covers much more area when *s/D* moves from the low case to the middle case. However, this is only a slight increase in coverage from the middle case to the high case.

From Figure 44, one can see that film effectiveness varies nonlinearly with respect to *BR*, and this is clearly consistent with the results from Nguyen *et al.* (2009) where they concluded that neither low *BR* nor high *BR* gives the best film performance, but it is the middle level. Due to the current range of the *BR* in this study, we can not be sure to say that *BR* = 1.0 gives the best performance. However, the authors are still able to infer that there is a value between 1.0 and 1.5 with an optimum value of *BR* that gives the maximum film performance. It would also be useful to know that we can improve spatially-averaged FCE up to 50% if we set the *BR* at the middle level rather than the lower or higher level. Again, one can easily visualize this change in Figure 44b.

The behavior of film performance versus *DR* can be seen in Figure 45. It is well known from the literature that the effect of *DR* on film performance is hard to predict as observed from the study of Sinha et al. (1991). Essentially, in the current case, Figure 45.b was plot when *BR* is kept at middle level (1.0). Since *BR* is proportional to *DR* and the V_c/V_m ratio, when *DR* decreases from

2.0 to 1.0, it will lead to an increase of V_c/V_m as well as an increasing of *MR* from 0.5 to 1.0. At the result, this helps the coolant jets get enough momentum to form a better blanket-like film. In other words, while detachment can occur initially right after the exit of the film hole, reattachment is formed quickly on the downstream area. Thus, the coolant can effectively cover more area in the downstream; hence spatially-averaged FCE is increased when *DR* decreases from 2.0 to 1.0. Additionally, spatially-averaged effectiveness behaves lightly nonlinear with respect to *DR* factor.

Finally, decision of setting the level of one factor is not absolutely independent to the decision of setting the level of the other factor in terms of affecting the film performance. It is well known as the 2-way-interaction characteristic of many practical design of experiment problem (3-way-interaction or higher order are practically and logically ignored in the current topic). Without performing a statistical analysis, one would hardly obtain the overall understanding the effect of those contribution factors and their cross-interaction effect on the film performance. Extremely useful information about the interaction effects are depicted in Figure 46 where the vertical axis is the spatially-averaged film effectiveness and the horizontal lines are the coded level of each corresponding factor. With a proper choice of combination effects, one could increase spatially-averaged FCE up to 400%, as shown in the (*s/D*)*(*DR*) sub plot. In detail, if one only looks at the behavior of the main factors (effects), one would easily prefer to set value of (*s/D*) as high as possible to achieve a high spatially-averaged FCE. However, even with (*s/D*) at a minimum value, if one keeps (*DR*) at also a minimum value (-1), then we can increase the spatially-averaged FCE from 0.1 up to 0.5. That makes the 2-way-interaction effect (*s/D*)*(*DR*) the second-largest contribution factor (effect) on the spatially-averaged FCE (12.9%) as shown in Table 11.

III.5.4 Summary and Conclusions

Factor (*p/D*) is also the most important (or influential) factor among the four studied factors in this work. Factor (*p/D*) confirms that the larger distance between the holes, the smaller film effectiveness will be. However, the decreasing rate of spatially-averaged FCE is absolutely not uniform. This conclusion could not be reached without performing the sensitive analysis. In fact, the decreasing rate of spatially-averaged FCE when (*p/D*) goes from low-level to mid-level is about 3.5 times higher than the rate when (*p/D*) goes from mid-level to high-level. In other words, the drop in spatially-averaged FCE when (*p/D*) go from mid-level to low-level is much less than the drop in spatially-averaged FCE when (*p/D*) goes from high-level to mid-level.

Increasing the trench depth (high *s/D*) gives higher film effectiveness. However, change in film effectiveness is also nonlinear with respect to this factor.

Similar to study from Nguyen et al. (2009), Sinha et al. (1991) and Goldstein et al. (1968), very strong non-linear behavior of blowing ratio is observed in this study. Specifically, the middle blowing ratio gives the maximum value of film effectiveness. It is still unclear about the effect of density ratio on film performance. In this current study where density ratio varies from 1.0 to 2.0, higher density ratio gives lower values of spatially-averaged film effectiveness.

Figures

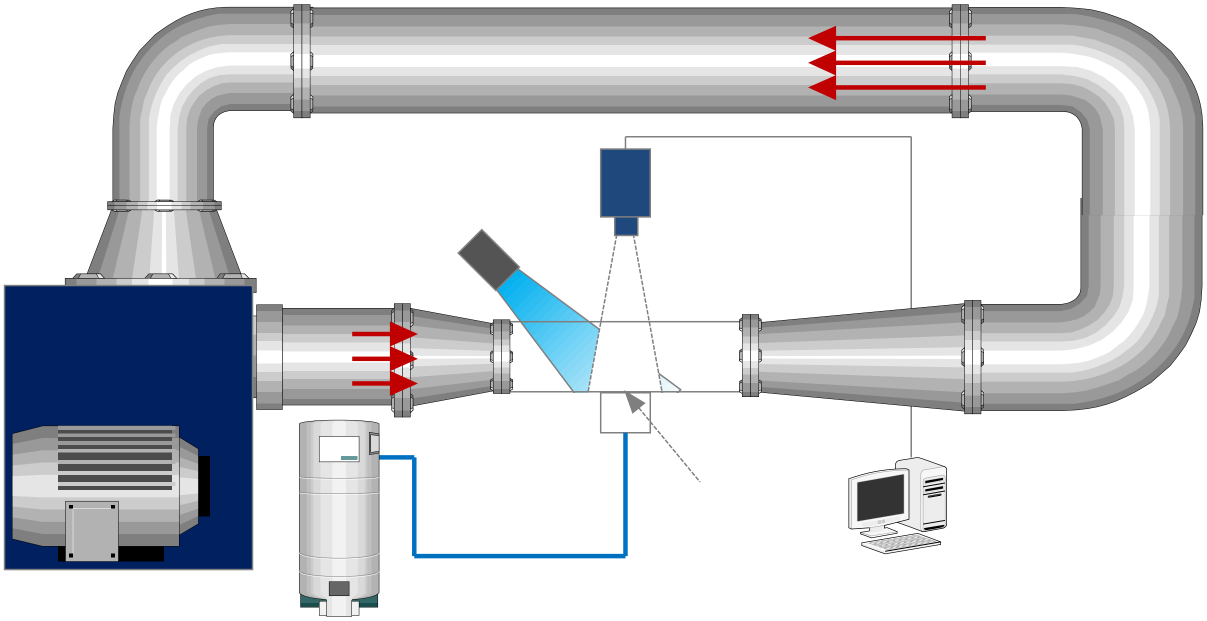

Figure 20 The basic film cooling vertical subsonic wind tunnel

LIGHT
SOURCE

PLENUM

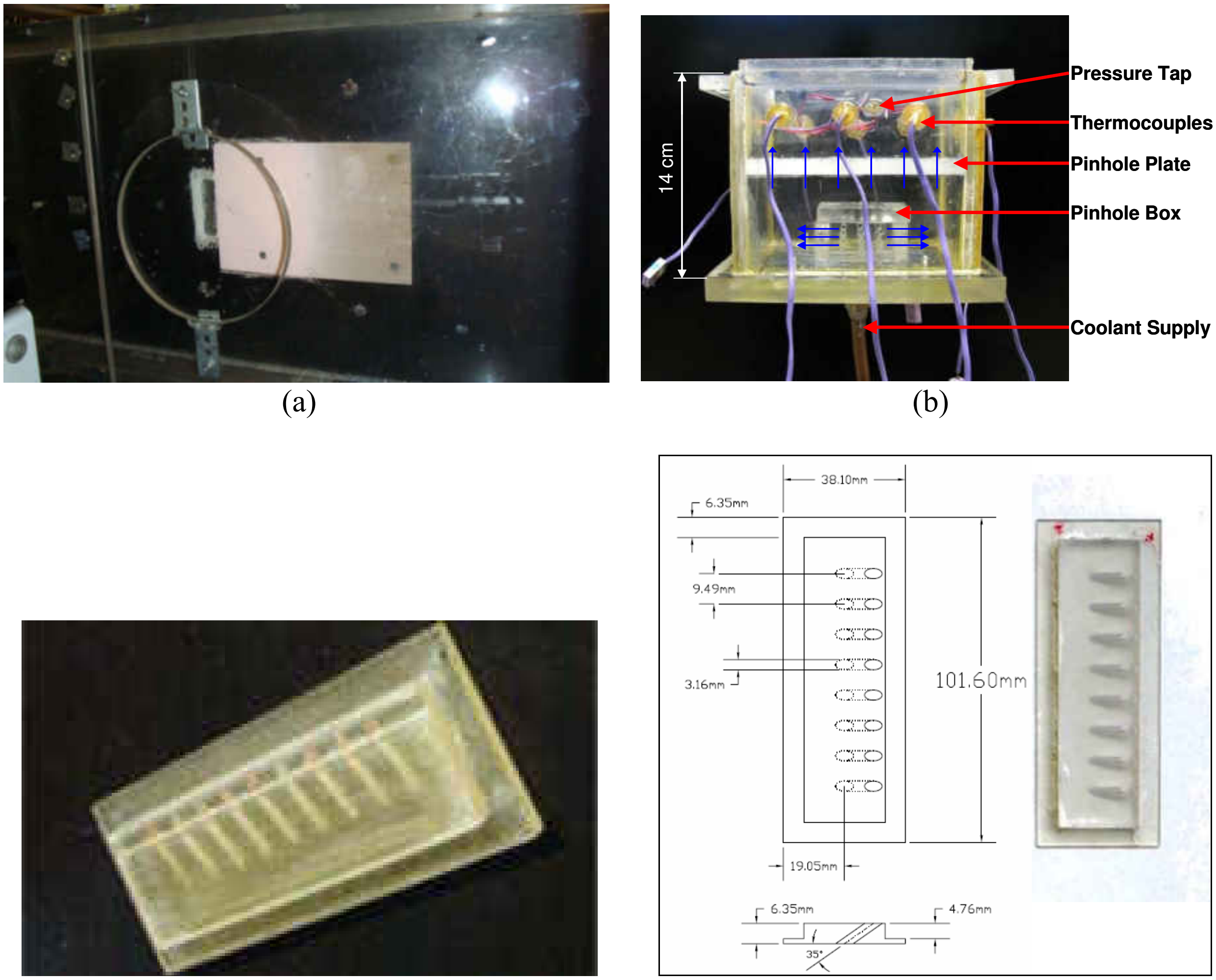

(a) (b)

(c) (d)

Figure 21 (a) basal-wood downstream test section looking through an annealed glass, (b) the coolant plenum, (c) a typical SLA test coupon, and (d) the coupon geometries

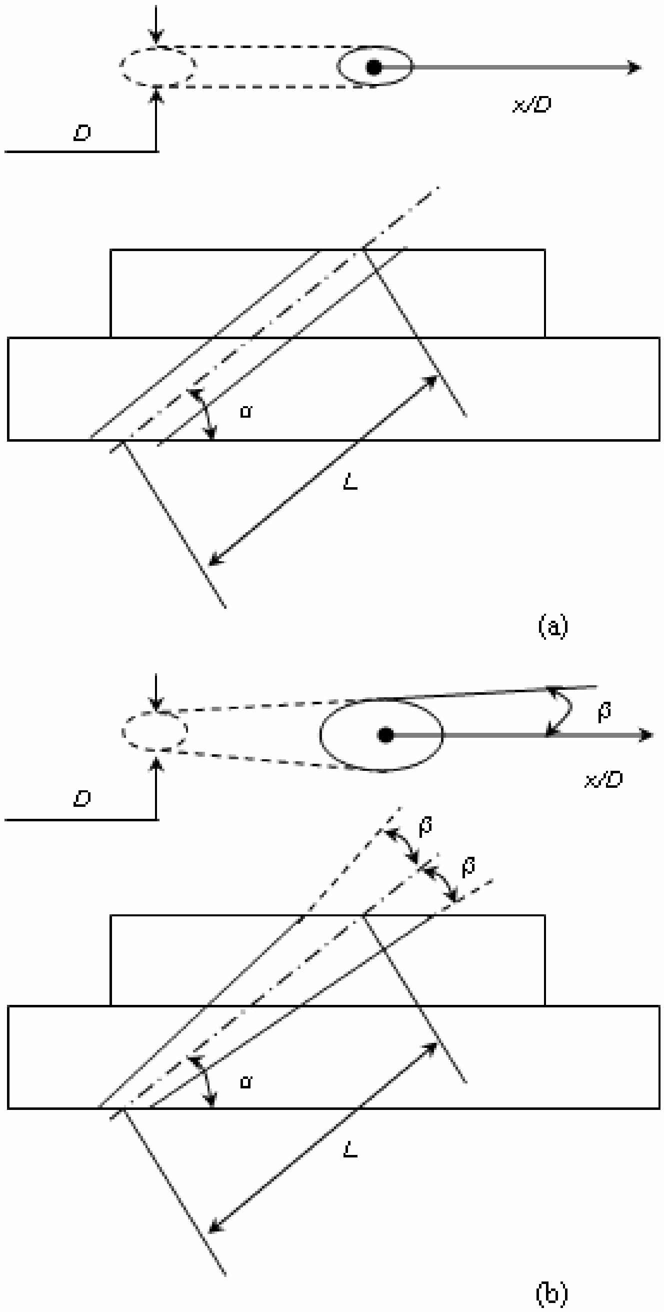

Figure 22 Coupons used in the experiment: (a) cylindrical-shaped hole and (b) conical-shaped hole

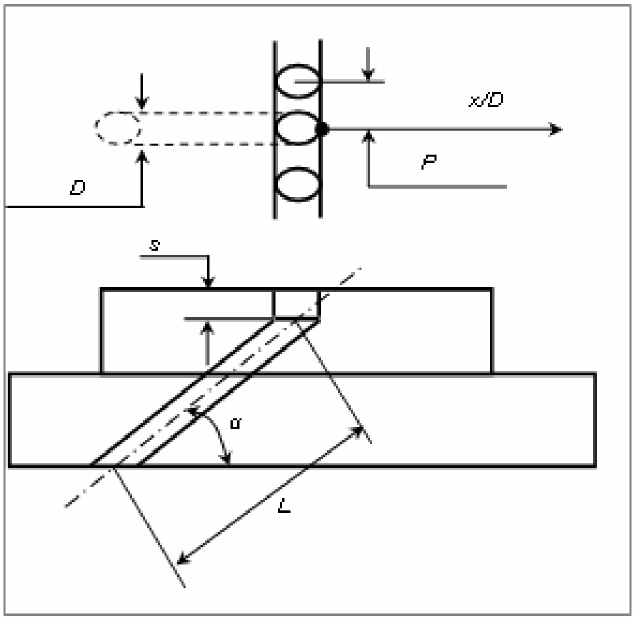

Figure 23 A sketch of Trenched Film Cooling Coupon (not draw to scale)

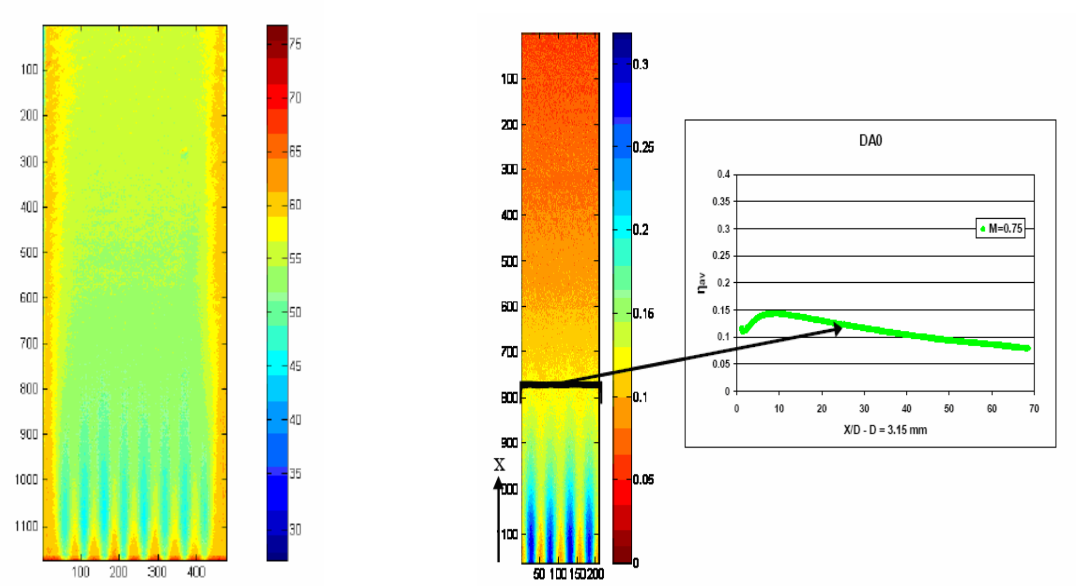

Figure 24 Demonstration of the TSP technique (Adapted from Rodriguez, 2008)

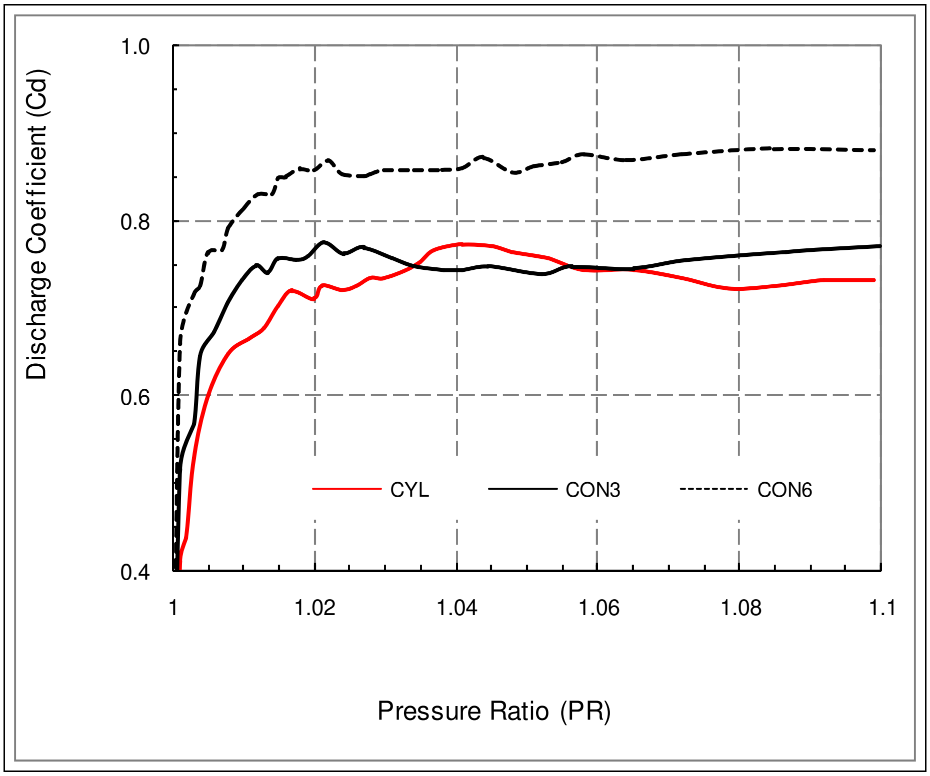

Figure 25 Experiment Cd Curves of CYL, CON3 and CON6

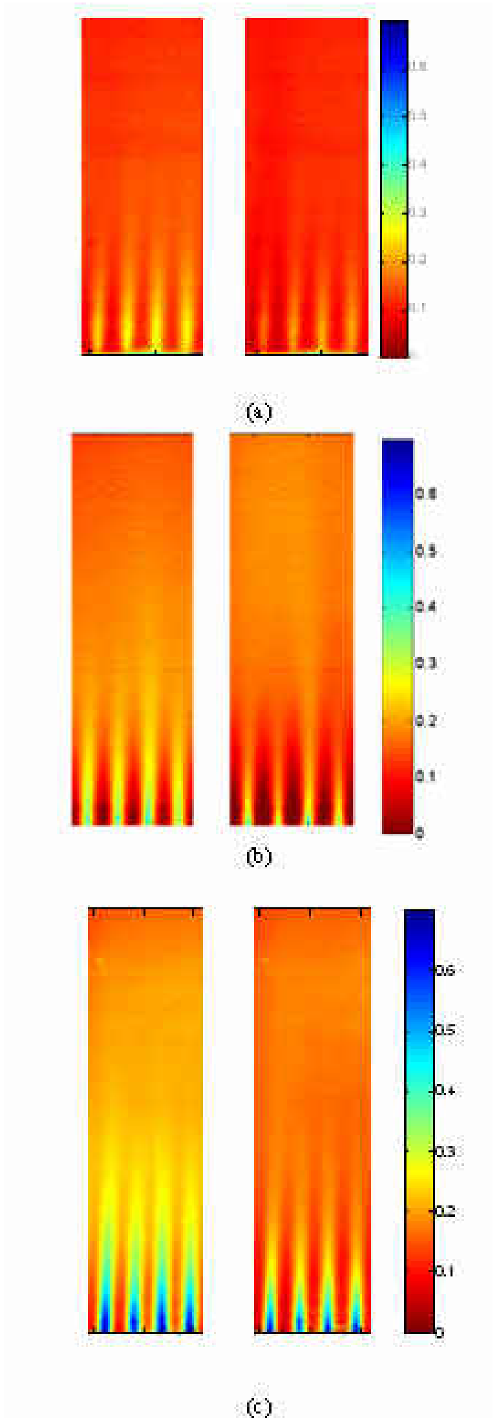

Figure 26 Experimental FCE Data at BR = 1.0 (left) and BR = 1.5 (right) for (a) CYL, (b) CON3 and (c) CON6

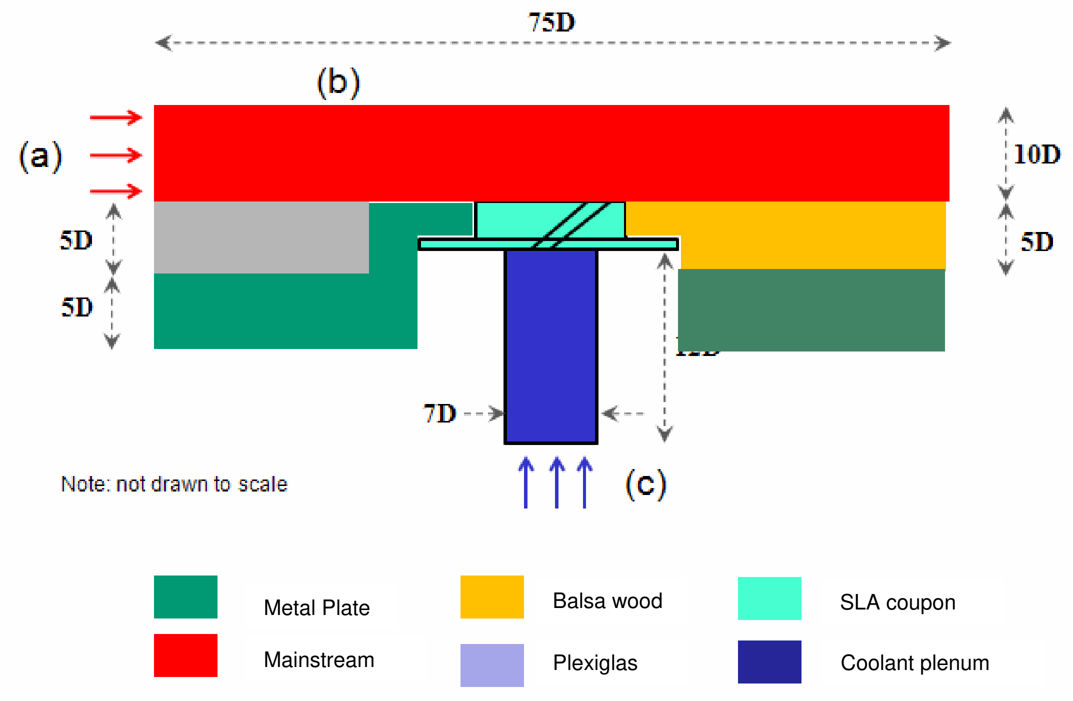

Figure 27 The CHT 3D Numerical Model

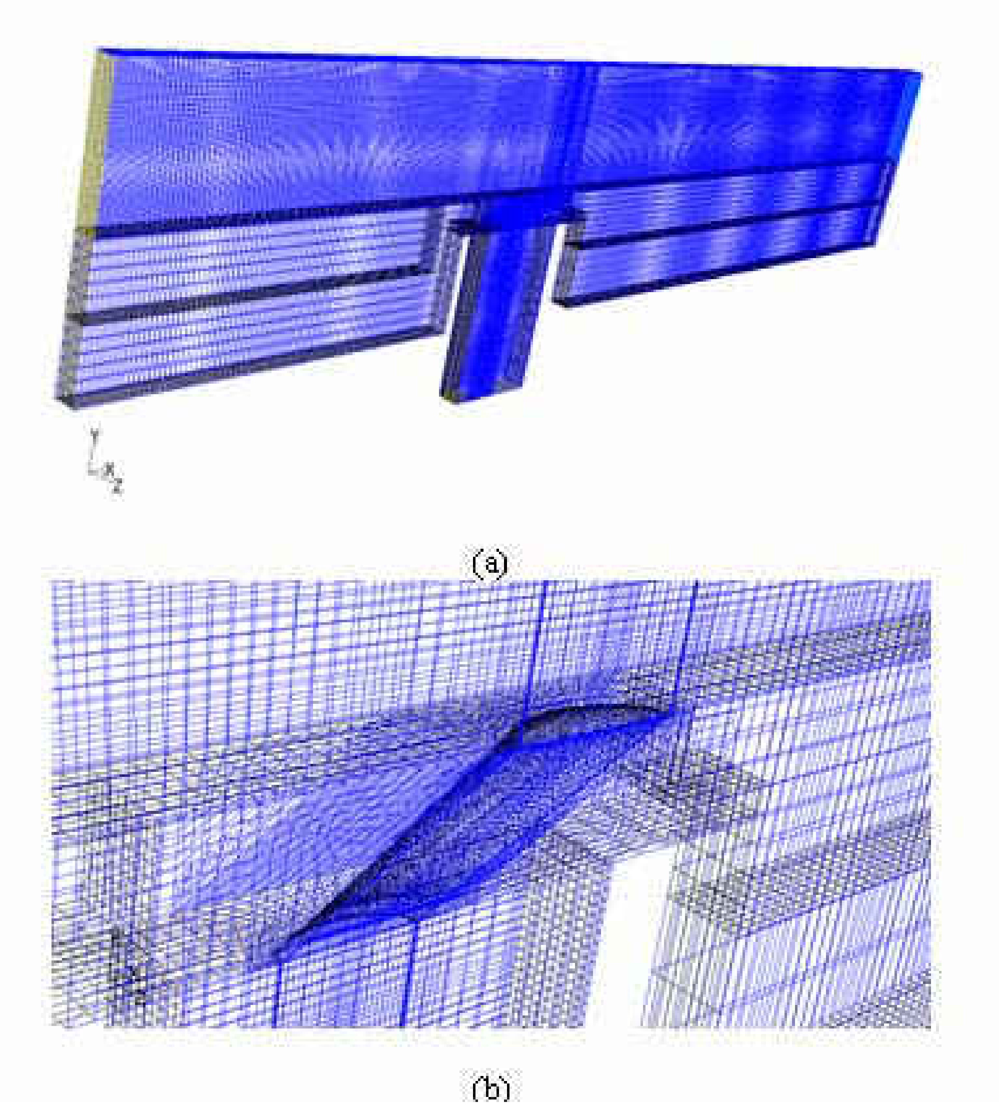

(a)

(b)

Figure 28 Grid Structure of the CHT model (CON3 is Selected to Show): (a) Overall View and (b) Close-up View

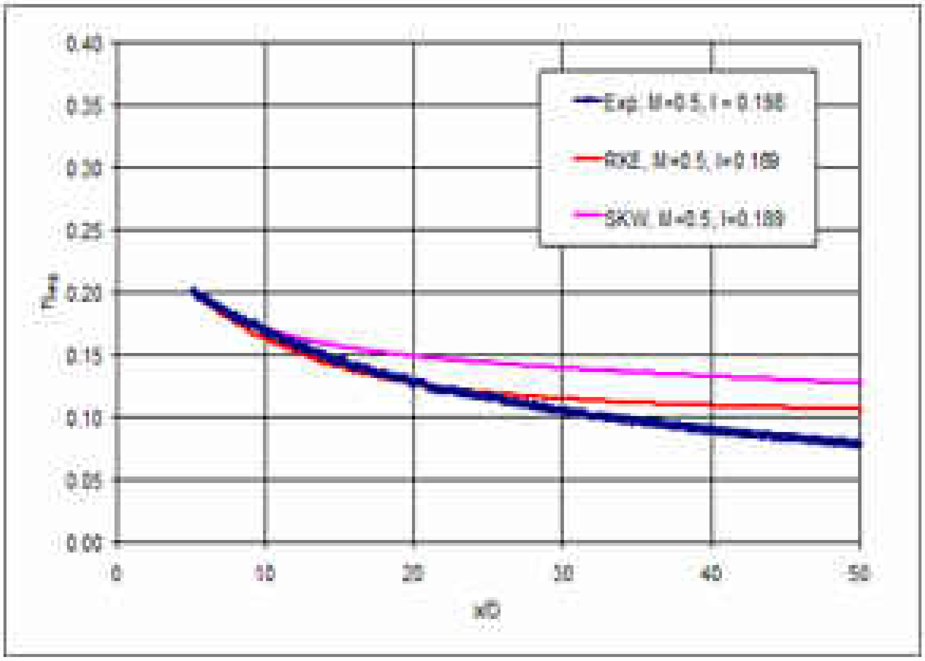

Figure 29 Two Turbulent Schemes versus Experimental Data (Reproduced from Rodriguez, 2008)

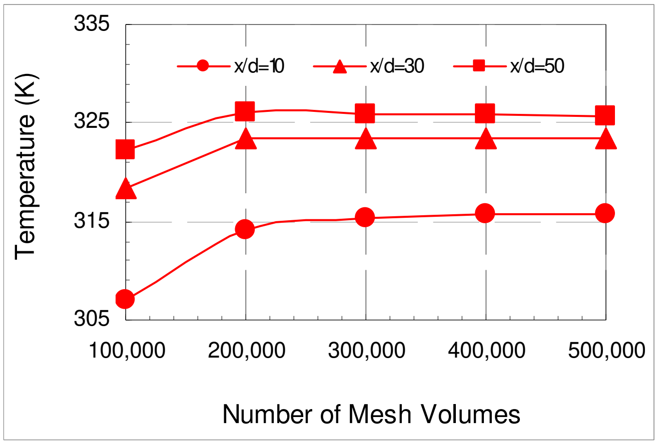

(a)

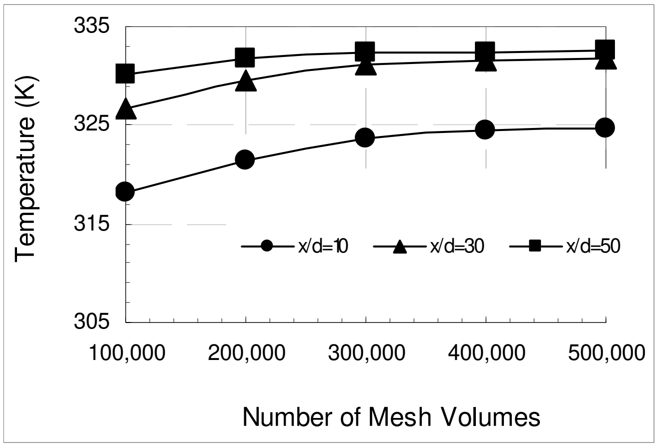

(b)

Figure 30 Grid Independent Study for the 3D numerical Model: Temperature Monitored at Three Set Points x/d= 0, 30 and 50 for (a) CYL and (b) CON3

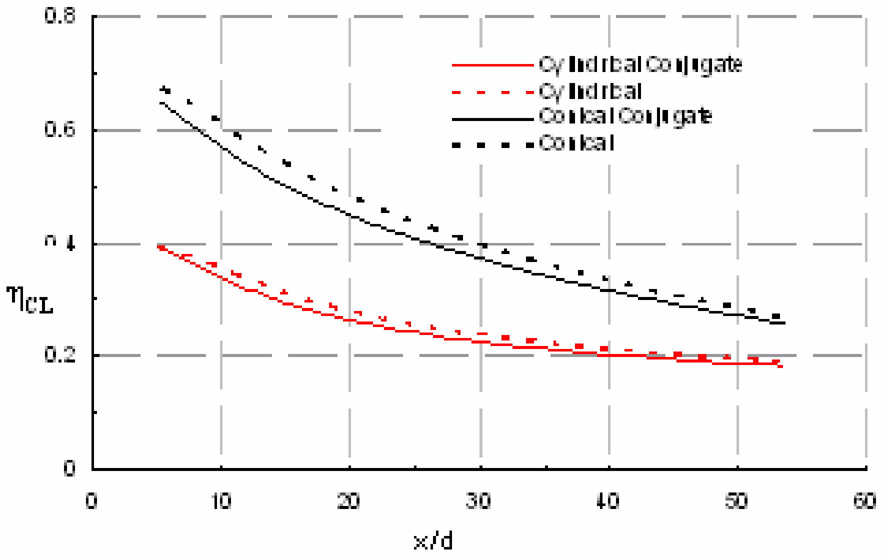

Figure 31 Traditional CFD versus CHT CFD Comparison for Cylindrical and Conical-shaped Film Hole

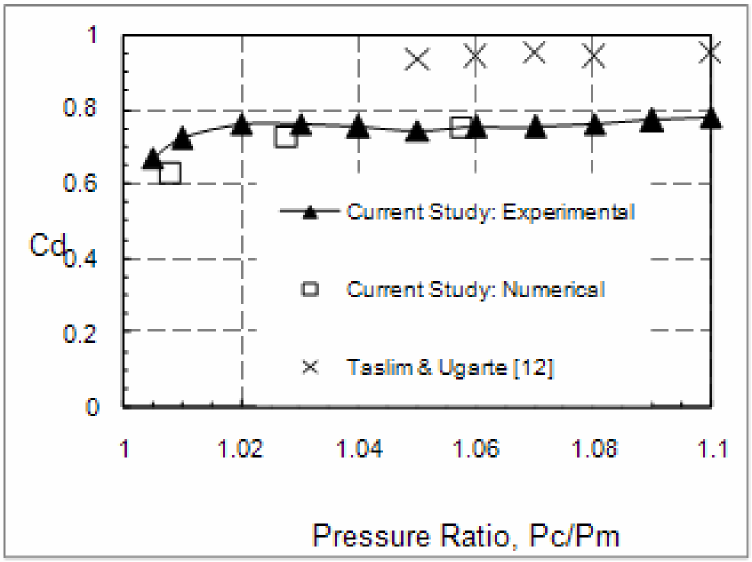

Figure 32 C_d comparison between Numerical (CON3), Experimental (CON3) and Literature

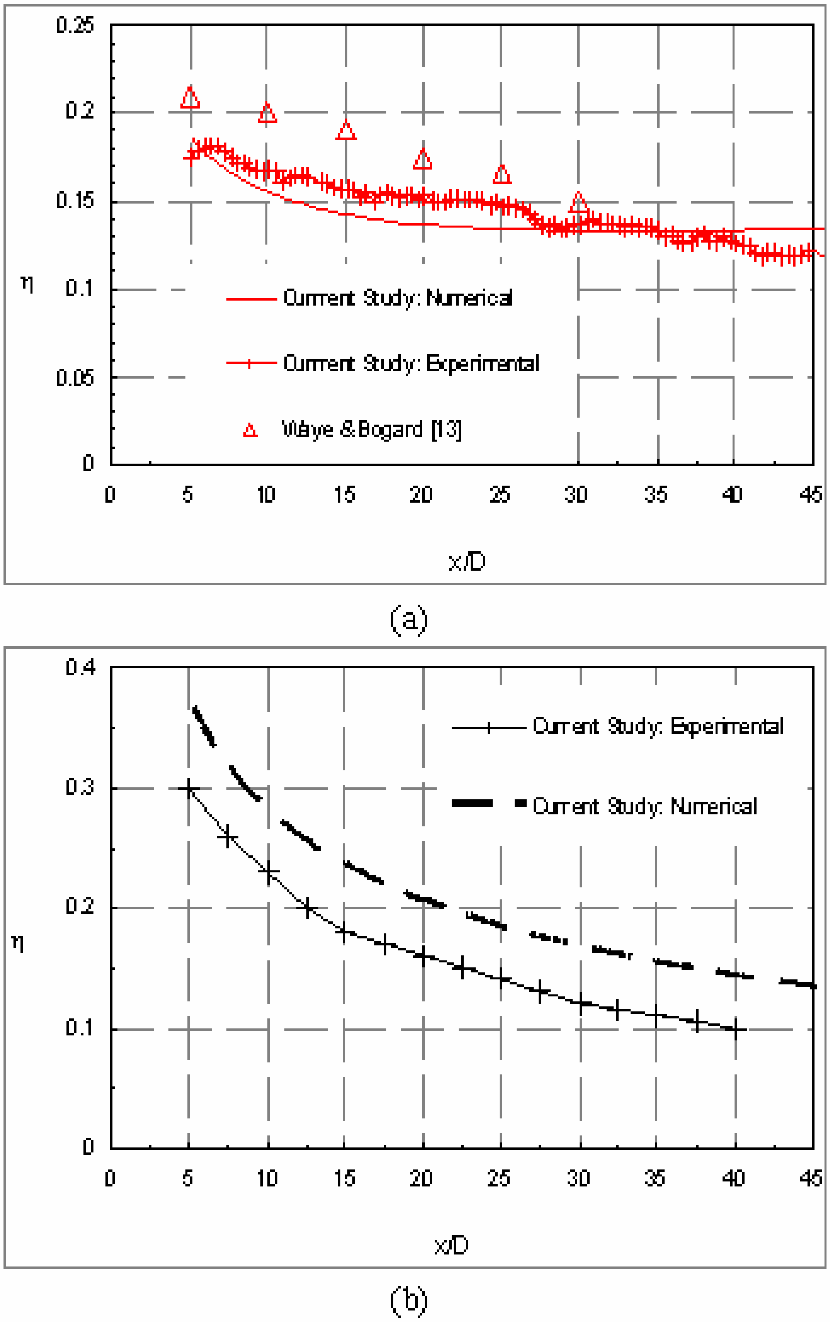

Figure 33 Numerical versus Experimental Comparison on Local FCE: (a) CYL (BR=1.0) and (b) CON3 (BR = 0.5)

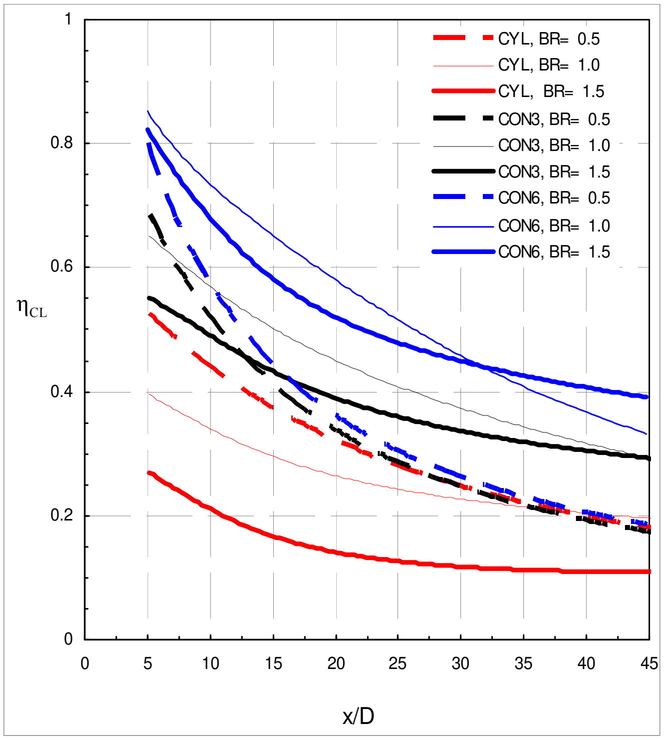

Figure 34 Conical vs. Cylindrical on centerline FCE

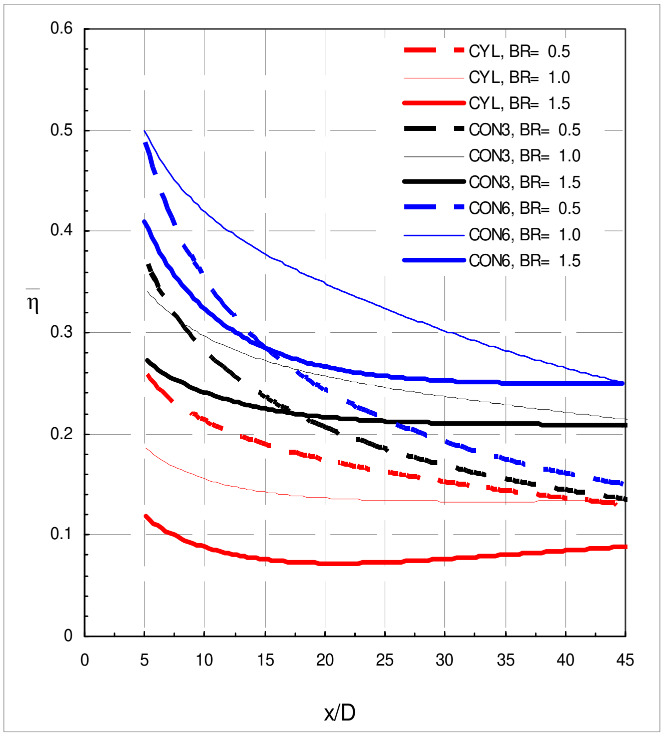

(a)

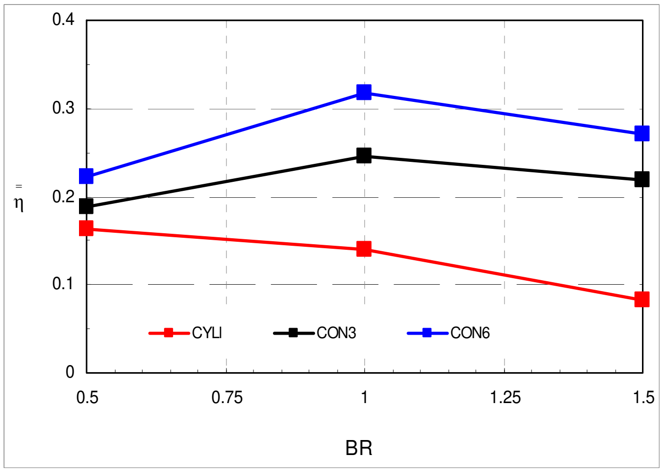

(b)

Figure 35 Conical vs. Cylindrical on: (a) Laterally-averaged FCE and (b) Spatially-averaged FCE

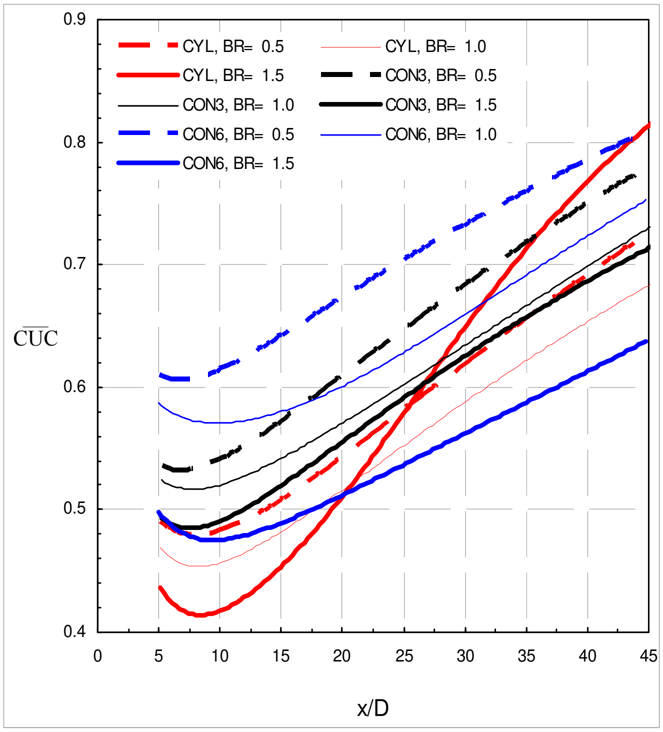

(a)

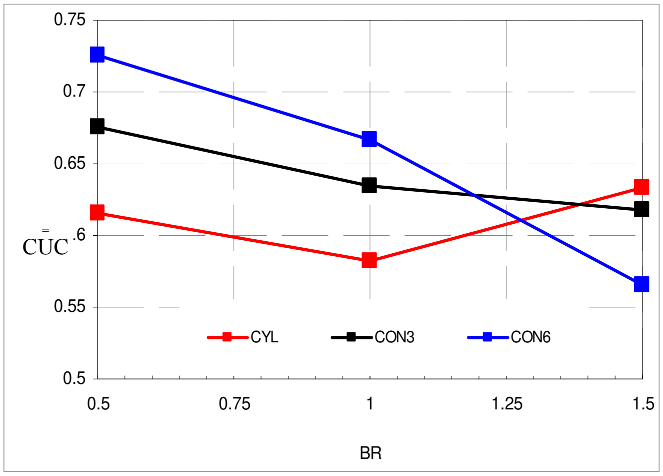

(b)

Figure 36 Conical vs. Cylindrical on: (a) Laterally-averaged CUC and (b) Spatially-averaged CUC

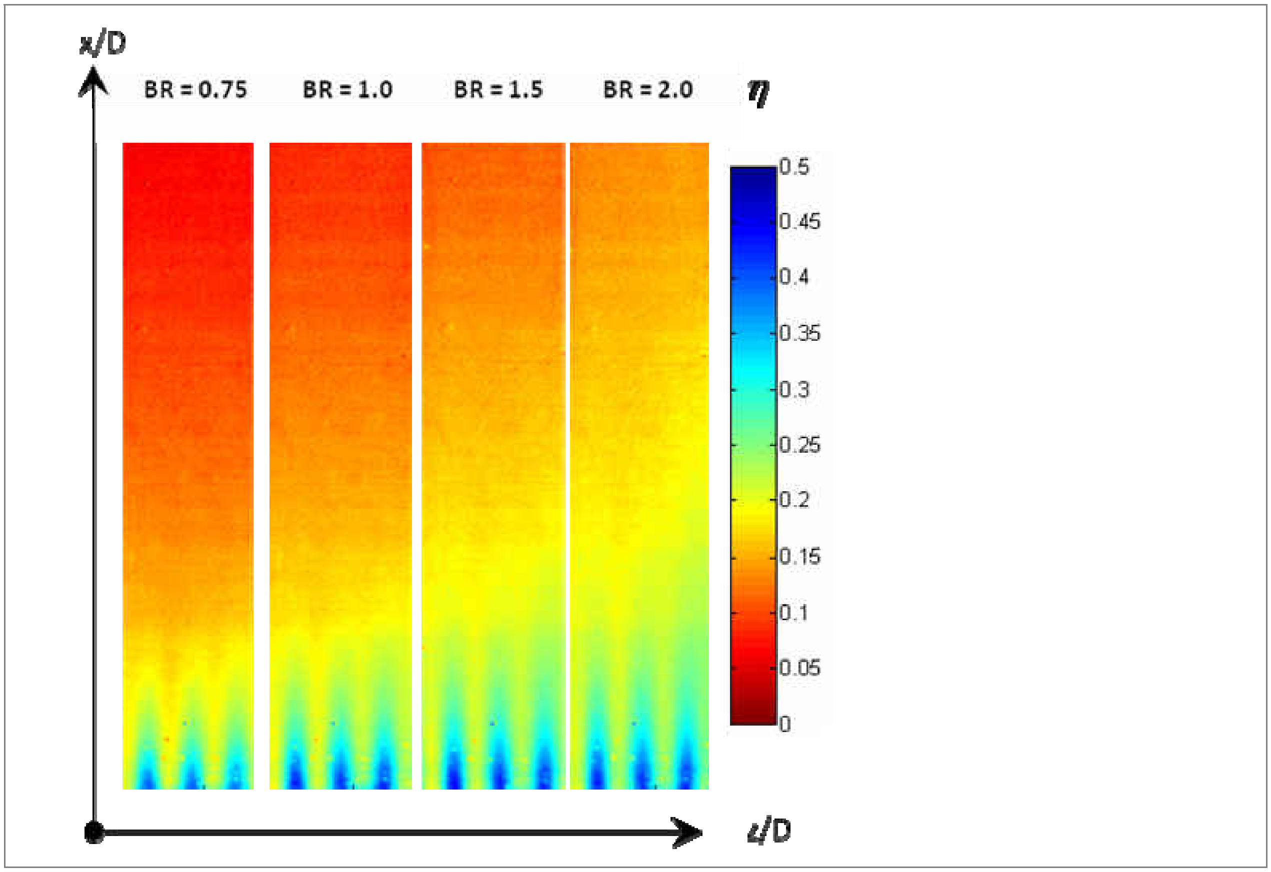

Figure 37 Film Effectiveness Obtained from Experimental

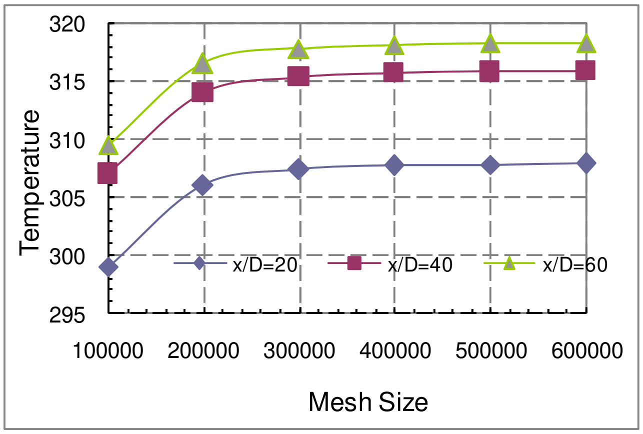

Figure 38 Grid Independent Study

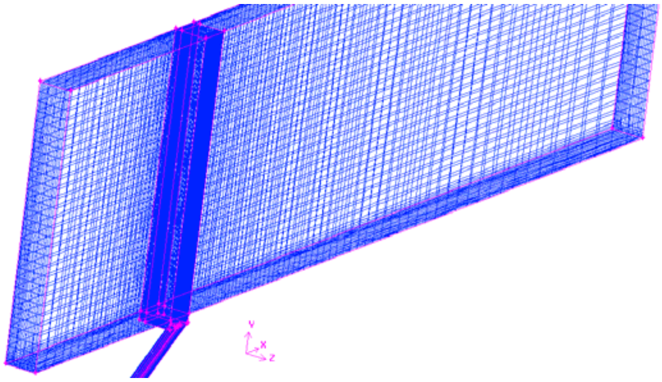

(a)

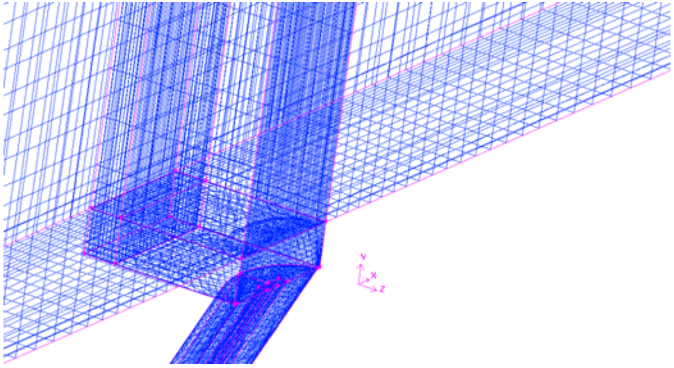

(b)

Figure 39 A Typical Mesh Model: (a) a Whole Domain and (b) Close-up View at the Traverse Slot

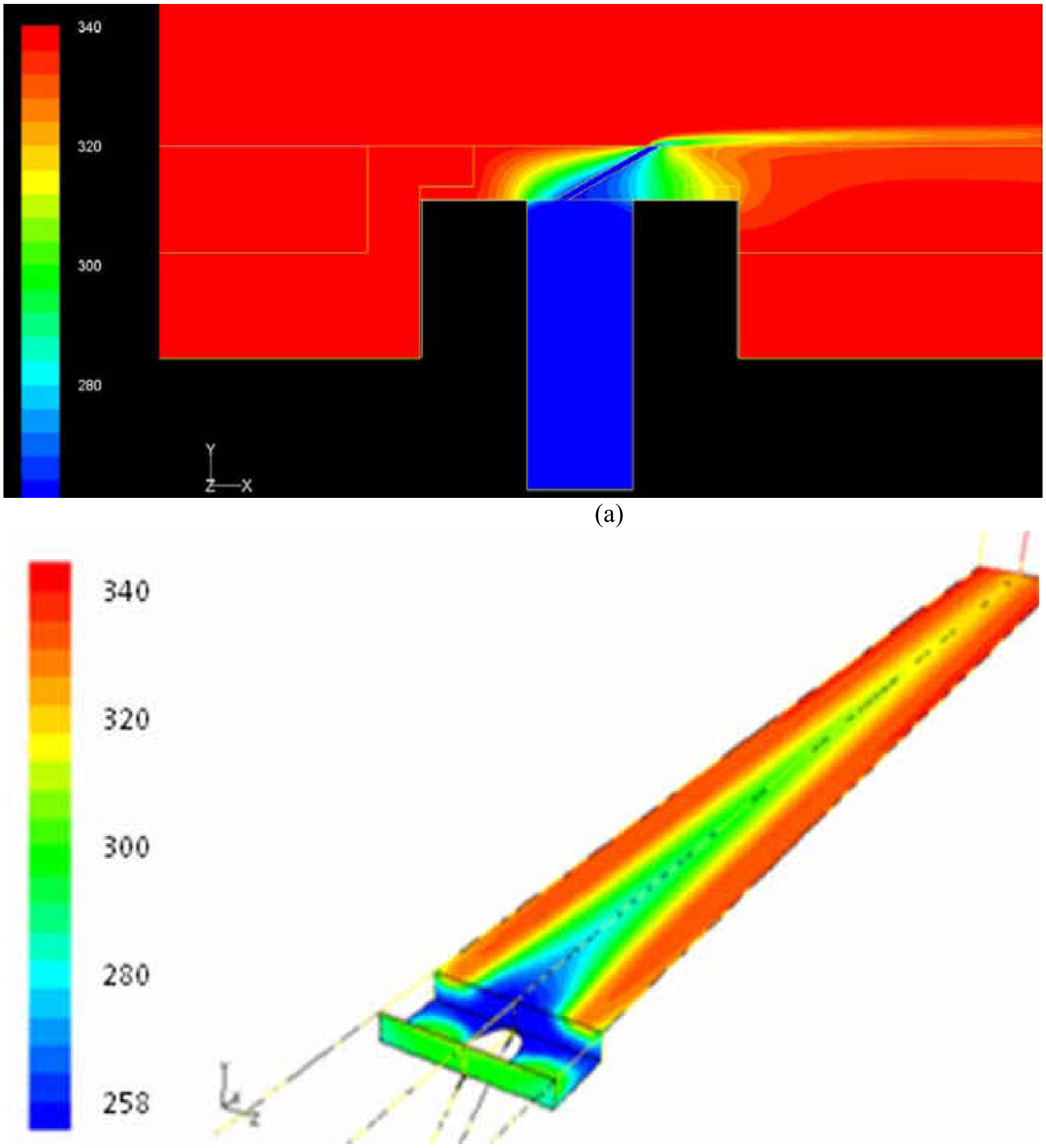

(a)

(b)

Figure 40 Typical Temperature Distribution from Numerical Solution (a) Overall View and (b) Downstream Surface

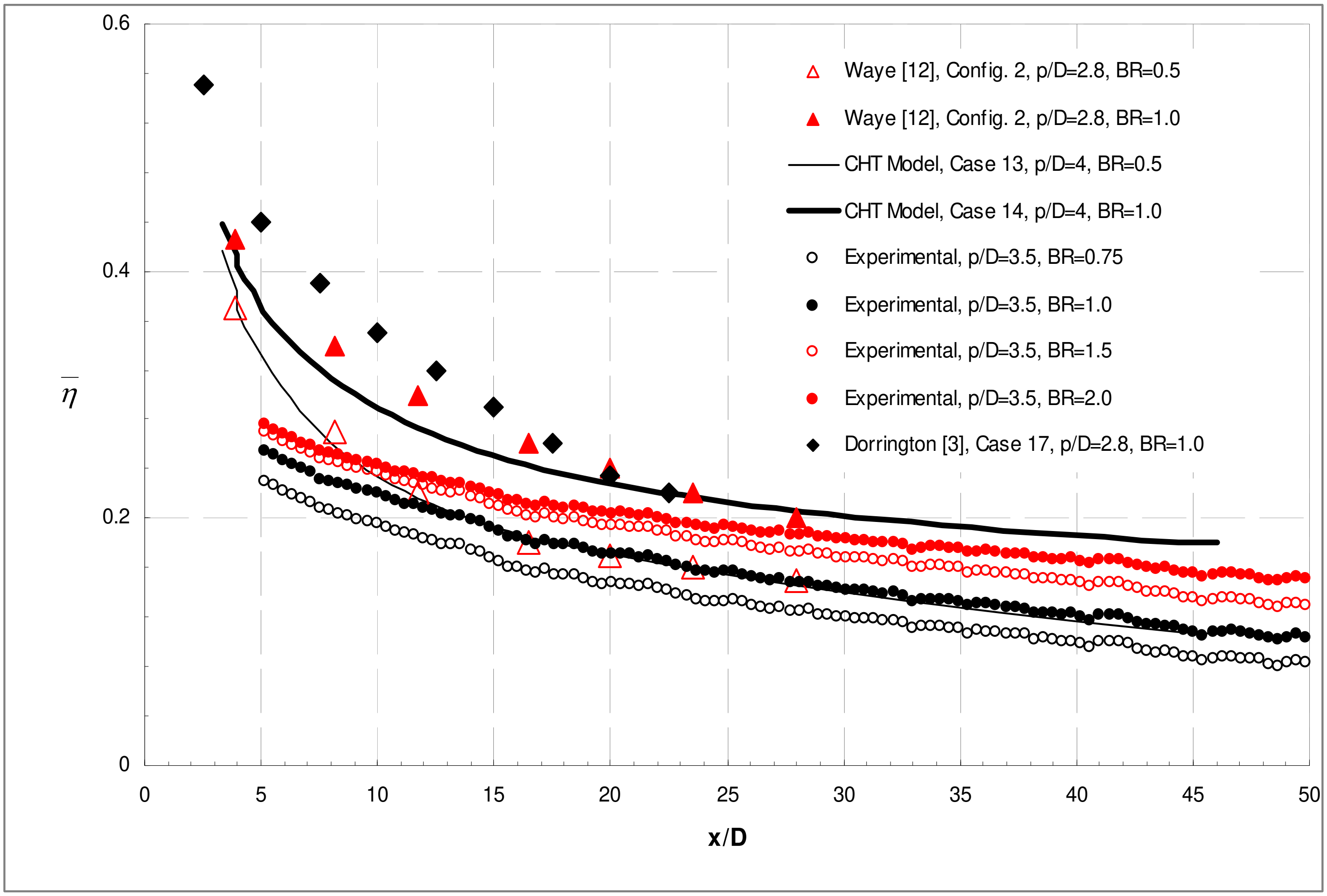

Figure 41 Validation of the CHT Numerical Model with In-house Data and Literature

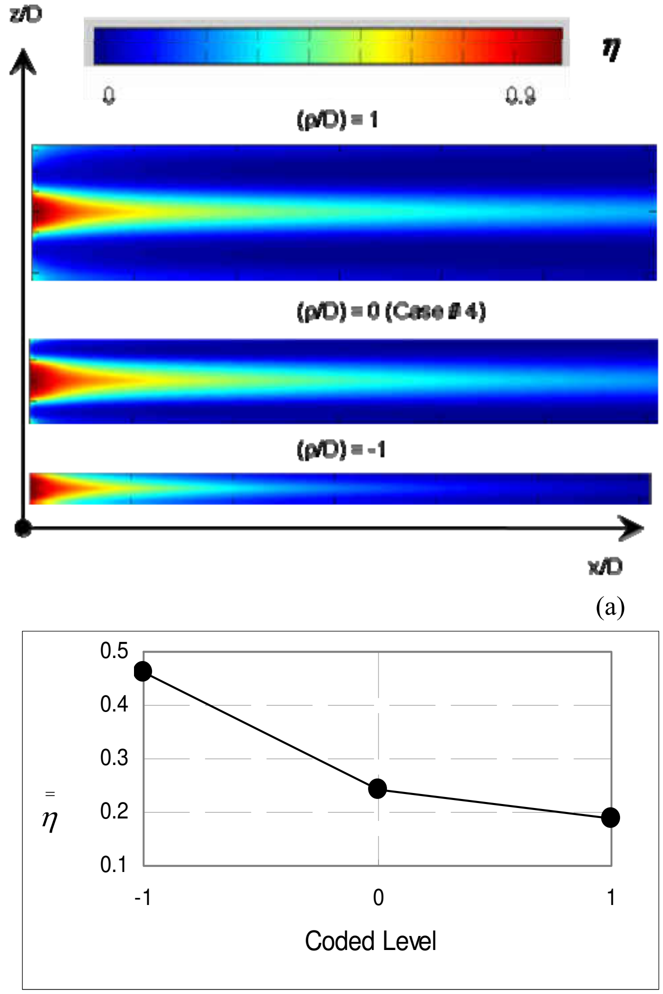

(b)

Figure 42 Effect of (p/D) on: (a) Laterally-averaged Effectiveness and (b) Spatially-averaged Effectiveness

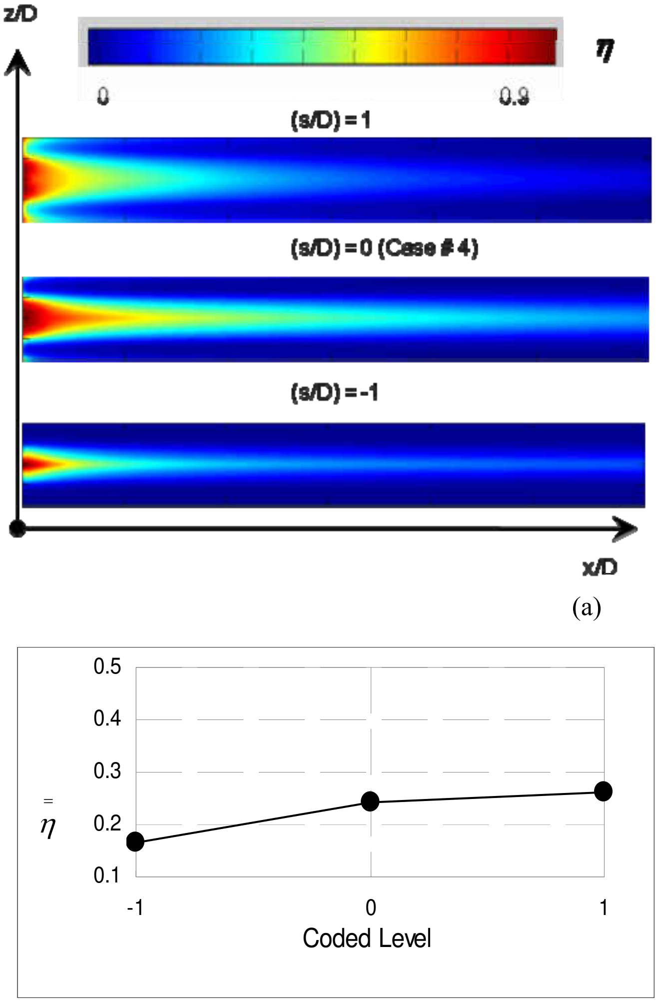

(a)

(b)

Figure 43 Effect of (s/D) on: (a) Laterally-averaged Effectiveness and (b) Spatially-averaged Effectiveness

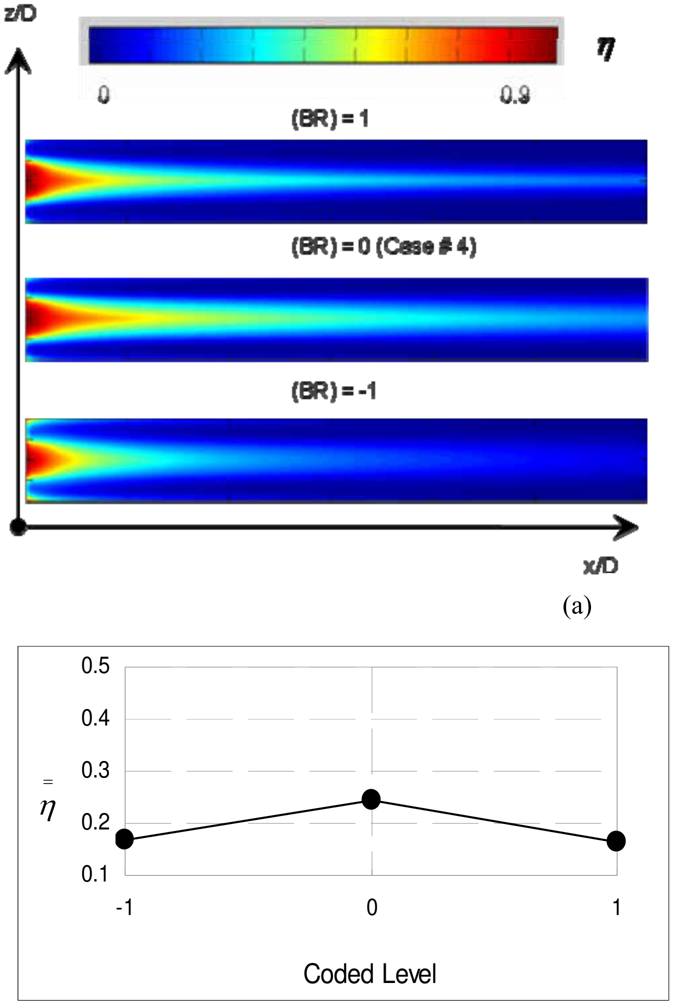

(a)

(b)

Figure 44 Effect of (BR) on: (a) Laterally-averaged Effectiveness and (b) Spatially-averaged Effectiveness

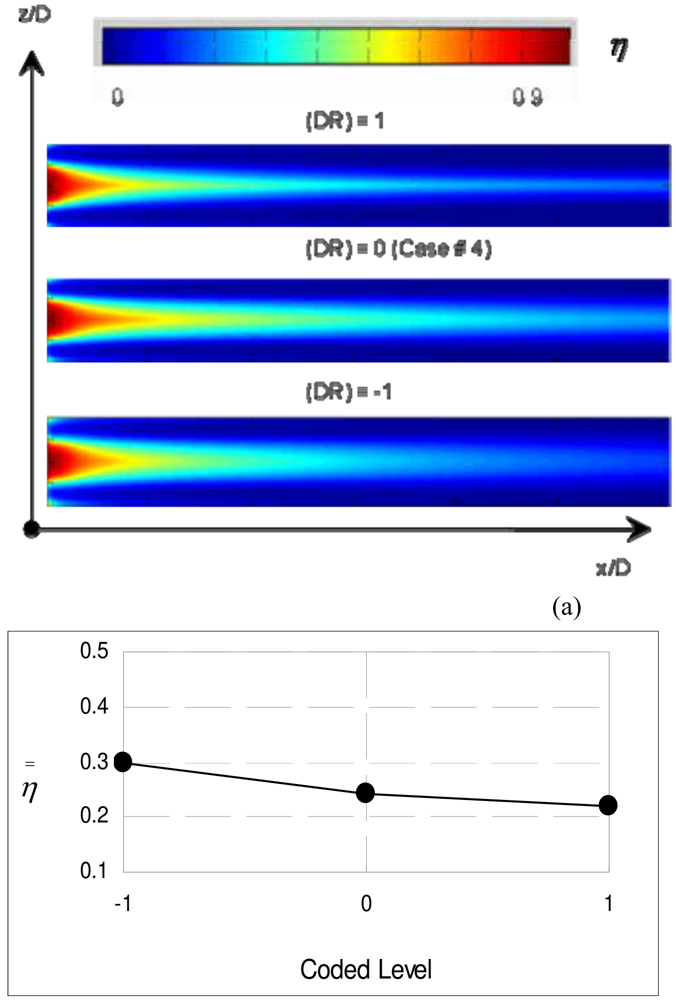

(a)

(b)

Figure 45 Effect of (DR) on: (a) Laterally-averaged Effectiveness and (b) Spatially-averaged Effectiveness

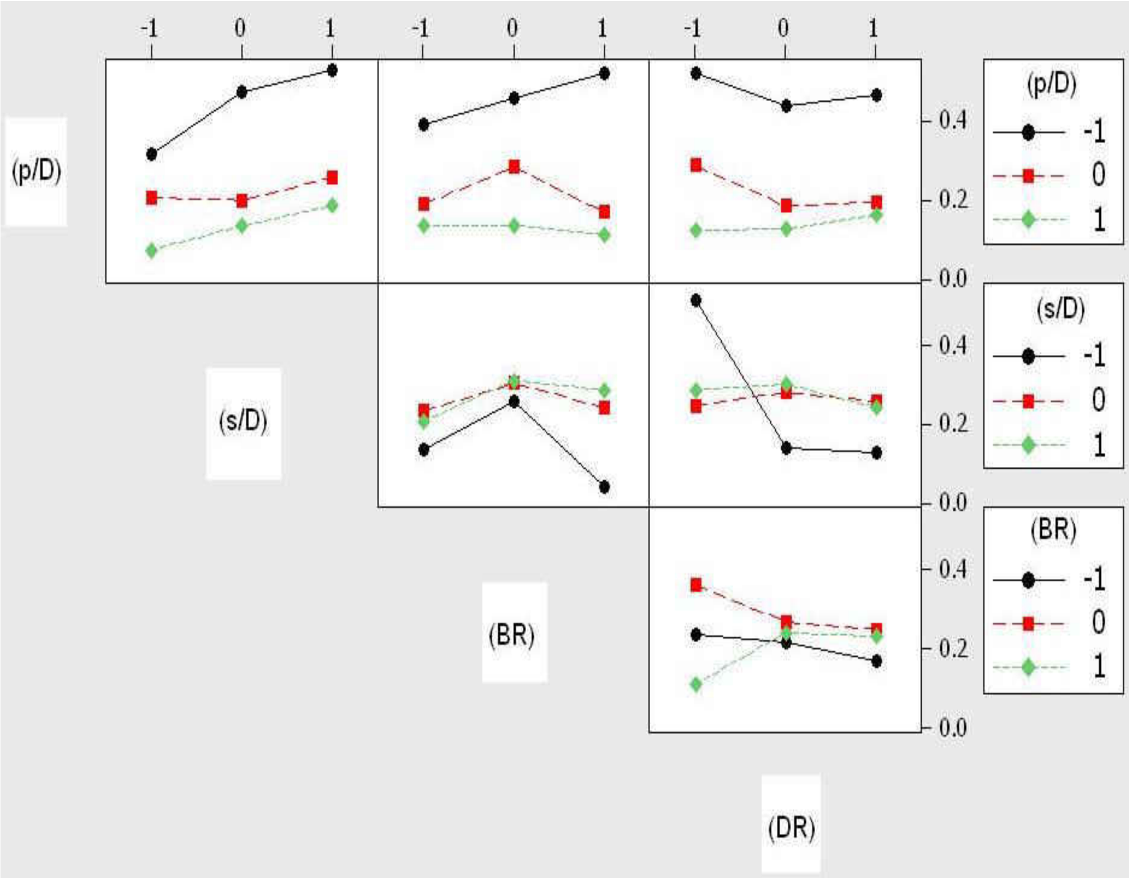

Figure 46 Film Performance $\overline{\overline{\eta}}$ versus 2-way Interaction Effects (Note: Vertical Axis is Spatially-averaged FCE and Horizontal is the Corresponding Coded Factor Level)

CHAPTER IV. ANNULAR CASCADE PLATFORM: CFD VALIDATED AGAINST AERO E^3 EXPERIMENTAL DATA

Once we have preliminary data and an understanding of film cooling performance on a flat plate, then we can move forward to film cooling on an annular cascade where film cooling is injected onto the hub endwall. The film cooling holes are distributed at the stagnation region (in the front of blade leading edge area). This chapter will validate the CFD model versus experimental data and literature.

IV.1 Annular Cascade Test Rig

IV.1.1 Test Rig Overview

The blade geometry from NASA E3 1st-stage turbine was adopted to build the test rig for this current study. This test rig was an academic project funded by NASA through UCF. The NASA/GE Energy Efficient Engine (E^3) Component Development and Integration program were initialized in 1978. The purpose of this program was to increase the efficiency of the Flight Propulsion system for commercial aircraft ($Ma<1$) for the time period of late 1980's to early 1990's. Among the desired improvement, aerodynamic performance of the airfoil needs to be improved, while one also needs to look at film cooling performance. Great endwall film cooling performance uses the least amount of coolant while still providing an uniform protection for the downstream surface. It also will not significantly increase the total pressure loss due to interaction between film flows and secondary flows inside the cascade. To gain in deeper knowledge of this interesting topic, a testing rig was built in the CATER facility starting Fall 2008 and has been successfully finished.

Figure 47 shows the overall view of the GE-E3 transonic close-loop wind tunnel with an exploded view of the test section and cross sections of the GE-E3 blades. The new rig was designed to interface with an existing wind tunnel at the Laboratory for Turbine Heat Transfer and Aerodynamics, part of the Center for Advanced Turbines and Energy Research (CATER). This imposes more design constraints, like the potency of the blower and locations of the new ductwork's inlet and outlet. The wind tunnel is meant to be closed-loop, as opposed to open-loop, meaning that it constantly circulates the same air which will produce hot main flow of around 80^{o} Celsius. Furthermore, it is a transonic wind tunnel, therefore it is capable of having flow speeds near Mach one (the speed of sound).

IV.1.2 Heat Exchanger

A closed loop fluid cooling system used a heat exchanger to cool the flow before it entered the test section as shown in Figure 48. The system was an industrial closed loop fluid cooling system made by Air Tak Compressed Air System Products in Worthington, Pennsylvania. The setup consisted of a pump station, a set of two fans outdoors to cool the fluid as it moved through copper coils, and the heat exchanger itself inside the tunnel. The heat exchanger was a series of rows of copper pipes that laid from one side of the tunnel to the other. Both ends of the heat exchanger had a pipe connected to it, one end had incoming fluid and the other end had outgoing fluid. The fluid used was water, although glycol could have been substituted if freezing was an issue. The pump station consisted of a 3 horse power motor, ball valves to make the flow rate adjustable, relief valves to prevent over pressurization of the system, and electrical equipment to run and maintain the system.

The heat exchanger system was a vital component to the overall system because it made it accessible to run the experiment more often as it rapidly cooled the tunnel down during and after each run. Without the use of the heat exchanger the amount of experimental runs that could be conducted in a single day would greatly decrease.

IV.1.4 Operating Modes and Parameters

In summary, the GE-E3 test section is has been designed to compromise with floor space already occupied by rooms and other wind tunnels in the building. Equipped with a 350 horsepower blower, whose function is to generate the movement of air in the direction also shown in Figure 47. A heat exchanger, which removes some of the heat added to the flow by the blower and maintains the flow at a desired temperature (about 80° Celsius in typical testing condition). The heat exchanger's outlet is to connect to the inlet of our new rig which has a 70 degree turning duct. There are splitters inside this duct for uniform flow distribution. The blower's diffuser (in blue color), is used to slow down the flow before it again passes through the blower. This will be where the test section's exit reconnects to the pre-existing rig. Figure 49 show the existing completed test rig which is currently located in the CATER lab.

Two operation models can be run in this testing facility: open loop and closed loop. For validation the numerical model, the test rig was run as open loop configuration and pressure tap at the the inlet and outlet with respect to the annular cascade were measured. A five hole probe (FHP) was also used to measure the static and total pressure at inlet and outlet.

IV.1.5 Fidelity of the Experimental Test Rig

To check the periodicity of the flow fed into each passage, static pressure taps were installed upstream and downstream of the airfoils on both ID and OD surfaces. Static pressure distributions are plotted in Figure 50. From the data, it is reasonable to state that a periodic condition was established for the middle passage of the annular test rig. A FHP was used to measure the static pressure as well as Mach number at several cross locations: 0% chord, 50% chord and 75% chord surfaces. Obtained data is displayed in Figure 50 a, b, c and d for the inlet ID, inlet OD, outlet ID and outlet OD respectively. It is obvious that we achieve the periodic condition for the middle three passages where almost three static pressure curves of three middle passages almost fall on top of each other. The author is confident enough with these results to move on with the next stage of experimental testing as well as CFD models to cross check the fidelity of the taken data.

IV.2 The CFD Models

Commercial meshing software, Gambit (2009) was used to generate a mesh model which is shown in Figure 52. Hexahedral elements were used to fill all parts of the domain while properly refined element layers are assigned around inlet, outlet, and solid surfaces to capture the high rates of change of momentum and heat transfer that exist there. In each element, velocity components, pressure, and temperature are approximated leading to a set of algebraic equations defining the discretized continuum. A segregated algorithm is used to solve the nonlinear system of finite algebraic equations. The iterative procedure for the solution is considered converged when the norm of the relative errors of the solution between iterative steps is less than a tolerance of 1e-6. The numerical solution includes the values of three velocity components, pressure, and temperature at every nodal point of the computational domain.

IV.2.1 The Complete Domain CFD Model

In order to achieve the confidentiality of the CFD model, a top down approach was taken into consideration. It means that a full domain from the inlet of transitional duct 1, to the outlet of the transitional duct 2 was considered and validated against the experimental test data. Figure 51 was sketched to show the full domain. A coarse grid was then generated using the commercial Gambit package. The grid has 3.1 million tetrahedral cells as shown in Figure 52. The purpose of this is to validate the computational model to the obtained experimental data from FHP measurement. The grid was then imported into Fluent to solve for the flow parameters using *k-ε* model with boundary conditions tabulated in Table 12. The inlet total and static pressure were obtained from Pitot tube data and applied to the CFD problem. Temperature was also measured using thermocouples which indicate the room temperature (in open loop)

Table 12 Boundary condition and Fluent setup for complete domain analysis

Inlet	
Boundary condition type	Pressure inlet (constant)
P_t [Pa]	101383
P_s [Pa]	96982
T [K]	296
I [%] and D_h [m]	3 and 0.9
Direction	Normal to boundary surface
Outlet	
Boundary condition type	Pressure outlet
P_s [Pa]	85000
Direction	Normal to boundary surface
Radial equilibrium	Yes
Temperature, T_m [^{o}C | K]	296
Solver algorithm	Simple
Viscous Model	k-ε
Material	Compressible ideal air

Convergence criteria were set to be less than 1E-5 for all the flow parameters, turbulence transport components (k and ε) except 1E-6 for the energy. From Figure 53, we can see that the periodicity was obtained for the three passages in the middle while the two half passage on the left and right play as a flow conditioning. The numerical results then validate with in-house FHP and Pitot tube data as discussed in the next section to validate the current CFD model. Figure 54 sketches a contour of Mach number on both ID and OD platforms and Figure 55 displays a contour of pressure distribution on both hub and tip endwalls.

IV.2.2 The Single Passage Domain CFD Model

An overall study was performed using a coarse grid to construct a full domain to simulate the full test section as in the previous section. In fact, the obtained numerical results are very favorably correlated to the in-house test data as well as literature. To prepare for the film cooling analysis in next chapter, and based on our computational capability/ resources, one passage is constructed and simulated using inherited boundary condition and boundary profiles for the inlet as well as the outlet in this section. The geometry is selected in the way that there is 85% chord of the upstream section and 130% downstream section of the annular duct are adopted for the sake of flow simulation accuracy while it does not consume much of the computer resources. Figure 56 demonstrates the single passage with corresponding boundary conditions on the surfaces.

Gambit mesh package was used to generate an all-hexahedral-cell mesh as shown in Figure 57. Grid independent study was also conducted for this annular single cascade without film hole for the validation purpose which is the main focus of this chapter. Boundary layer thickness and pressure profiles are extracted from the full-domain CFD model in the previous section and applied at the inlet surface of the current model. Plots of velocity and total pressure profiles at the mainstream inlet were prepared in Figure 58.

Fluent again is used to carry out the flow analysis. Table 13 is tabulated for all applied boundary conditions as well as parameter setup in Fluent for the sake of completeness. A commercial CFD packet, Fluent (2009) was chosen to carry out the flow analysis. The realizable *k-ε* was again chosen to be the turbulence transport for the RANS viscous model. The turbulence model has been proven to provide great results versus experimental tests Rodriguez (2008) and Nguyen et al. (2010).

Table 13 Boundary Condition and Fluent Setup for the Single Domain Analysis

Inlet	
Boundary condition type	Pressure inlet (profile)
P_t [Pa]	PROFILE
P_s [Pa]	PROFILE
T [K]	PROFILE
I [%] and D_h [m]	PROFILE
Direction	PROFILE
Outlet	
Boundary condition type	Pressure outlet (profile)
P_s [Pa]	PROFILE
Direction	PROFILE
Radial equilibrium	Yes
Temperature, T_m [^{o}C | K]	PROFILE
Solver algorithm	Simple
Viscous Model	k-epsilon
Material	Compressible ideal air

Typical results of total pressures are shown in Figure 59 at several axial cross section where we can obviously see that there are horse-shoe and passage vortex cores formed a little away from ID and OD surfaces. These vortices cores, which formed right after the leading section, get traversed downstream until after the trailing edge section and gradually wash out at the exit surface.

GRID INDEPENDENT STUDY

Before we move on to the validation between numerical simulation data, a study on the integrity of the grid was conducted with several gird sizes: 0.57, 1.1, 2.16 and 4.2 million cells were created. Pressure and velocity of two locations inside the passage are reported. Detail of the grid independent study is shown in Figure 60.

IV.3 Validation of Single Domain CFD Model

IV.3.1 CFD versus In-house Experiment

Figure 61 serves as a comparison of the static pressure and Mach number between the *k*-*ε* CFD numerical solution and experimental data. Both Mach number and static pressure experimental curves are plotted at four axial locations where 0% is at the inlet (leading edge surface) and 100% is at the trailing edge surface. There is a missing value for the 100% location of the experimental due to a space constraint. The area-weighted values are presented for the CFD curves. From there, it can be seen that the CFD relatively agrees with experimental data. Hence, in terms of order of magnitude, the authors are confident to move on to next phase.

IV.3.2 CFD versus Experiment from Literature

Validate against Freidrich (1997) and Harrison (1989) on ζ and ζ_1:

Selected axial planes selectively were created for demonstration and data extraction in this section. There are several ways to define the pressure loss coefficient. Equation 4.1 and 4.2 are two typical ways which have been defined in the literature for ζ and ζ_1:

$$\zeta = \frac{{}^{\infty}P_{t,\,i}^{mavg} - {}^{\infty}P_{t,\,o}^{mavg}}{{}^{\infty}P_{t,\,i}^{mavg} - {}^{\infty}P_{s,o}^{mavg}} \tag{4.1}$$

$$\zeta_1 = \frac{{}^{\infty}P_{t,\,i}^{mavg} - {}^{\infty}P_{t,\,o}^{mavg}}{{}^{\infty}P_{t,\,i}^{mavg}} \tag{4.2}$$

Detail of each plane is shown in Figure 63. Mass-averaged pressure loss coefficient ζ is calculated and listed in Table 14. It is worthwhile to note that the max value of ζ_1 in the studied region is 2.70, which is the same order of magnitude as the work from Harrison (1989), where he measured a mass averaged loss coefficient of 4.8%; and as the one from Friedrichs (1997), which is 4.7%. ζ and ζ_1 contours at selected axial cross sections were plotted in Figure 64.

Table 14 Mass-weighted average pressure loss coefficient, ζ and ζ_1 at several planes

Surface	ζ_1 [%]	ζ [%]
Inlet	0.00	0
1	0.04	0.9
2	0.36	2.8
3	0.79	4.3
4	1.37	10.1
5	1.52	11.0
6	1.71	12.0
7	2.03	14.3
8	2.24	15.8
9	2.49	17.6
Outlet	2.70	19.1

With Kopper (1981) on Spanwise Distribution of Total Pressure Loss:

Base on Table 14 and Figure 64 we can see that it is the surface #6 (or x/D=1.27) where the passage vortex core (center core) appears most clearly. Hence, this surface was selected to extract data to validate with the spanwise pressure loss distribution reported by Kopper (1981). They conducted a planar wall cascade with a linear profile airfoil. Figure 65 was prepared for this comparison purpose.

With Chappell et al. [2010] and Boyle and Senyitko (2003):

Each study group has different definition of pressure loss coefficient, for example Boyle and Senyitko (2003) and Chappell et al. (2010) have a definition of pressure loss coefficient as follows as in Equation 4.3

$$\zeta_A = \frac{{}^{\infty}P_{t,i}^{aavg} - {}^{\infty}P_{t,o}^{aavg}}{{}^{\infty}P_{t,i}^{aavg} - {}^{\infty}P_{s,o}^{aavg}} \tag{4.3}$$

In Equation 4.3, the numerator is the difference between the area-weighted average total pressure at the inlet and the outlet; the denominator is difference between the area-weighted average inlet total pressure and the area-weighted average outlet static pressure. Figure 66 shows a comparison the data extracted from the current study to those from Boyle and Senyitko (2003) and Chappell et al. (2010). From there we can see that the current study (available only at turbulence intensity of 3%) fall within the lines from those two studies which makes us confident about our model and allows us to move on the next chapter.

IV.4 Discussions

A full domain model was simulated and analyzed to validate the in-house experiment. Selected data was extracted to apply for a single domain model (one passage). The obtained CFD data was validated against the literature both numerically and experimentally, and it shows very good agreement in terms of pressure loss coefficients ζ , ζ_1, and ζ_A.

Figures

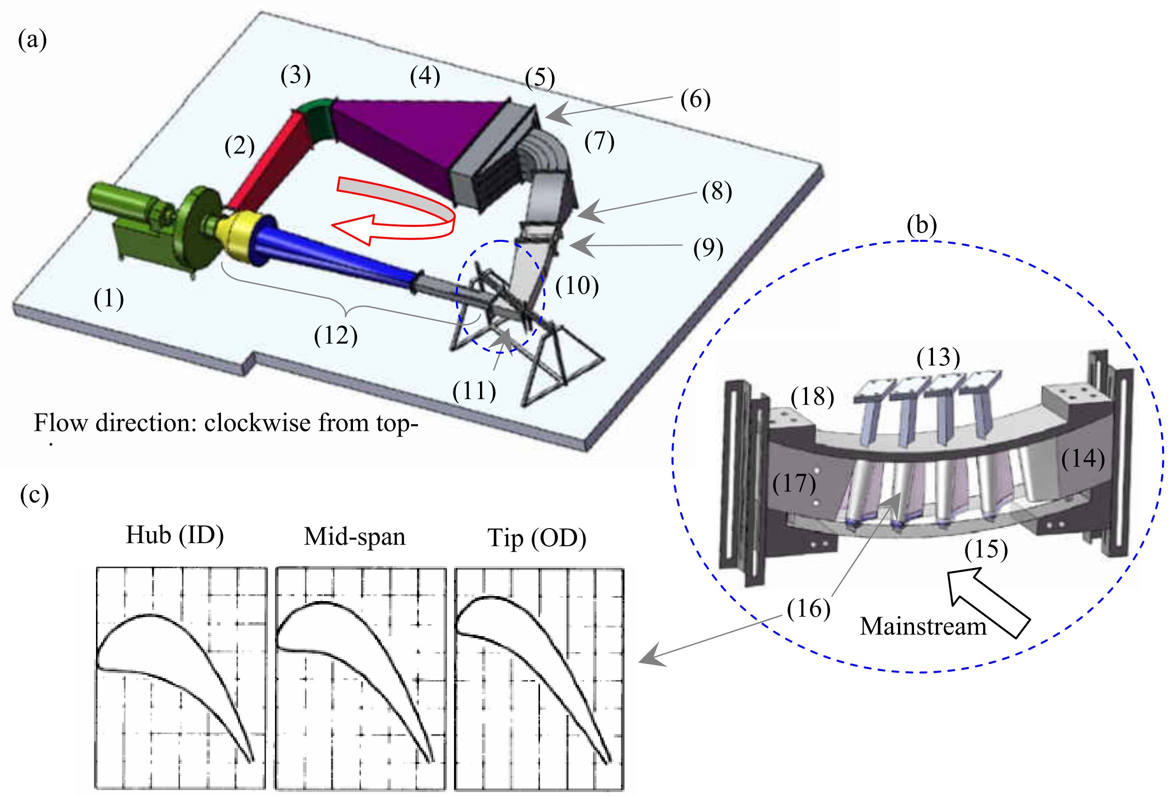

(1) High pressure blower generated by a 350HP motor
(2) Extension duct
(3) 90° turning duct
(4) Big diffuser duct before heat exchanger system
(5) Heat exchanger system
(6) Elevation duct with splitters inside
(7) 70° turning duct
(8) Contraction duct
(9) Extension box with honey comb and screens
(10) Rectangle-to-annular duct
(11) Annular-to-rectangle duct
(12) Diffuser ducts before the blower
(13) Support-steel cores (4)
(14) The right-half-airfoil block
(15) Outer diameter (OD) platform
(16) GE-E3 1st-stage turbine blades (4)
(17) The left-half-airfoil block
(18) Inner diameter (ID) platform

Figure 47 (a) Layout of the GE-E3 transonic wind tunnel at CATER facility, (b) a close-look on the annular testing cascade, and (b) the cross section of the GE-E3 1st stage rotor (Note: pitch in (c) represents mid-span in this study)

(a

(b)

(a) Heat exchanger cooler unit (b) Pumping station-Mixing valve unit (c) Heat exchanger (seen with upstream make-up air module).

Figure 48 Heat Exchanger unit

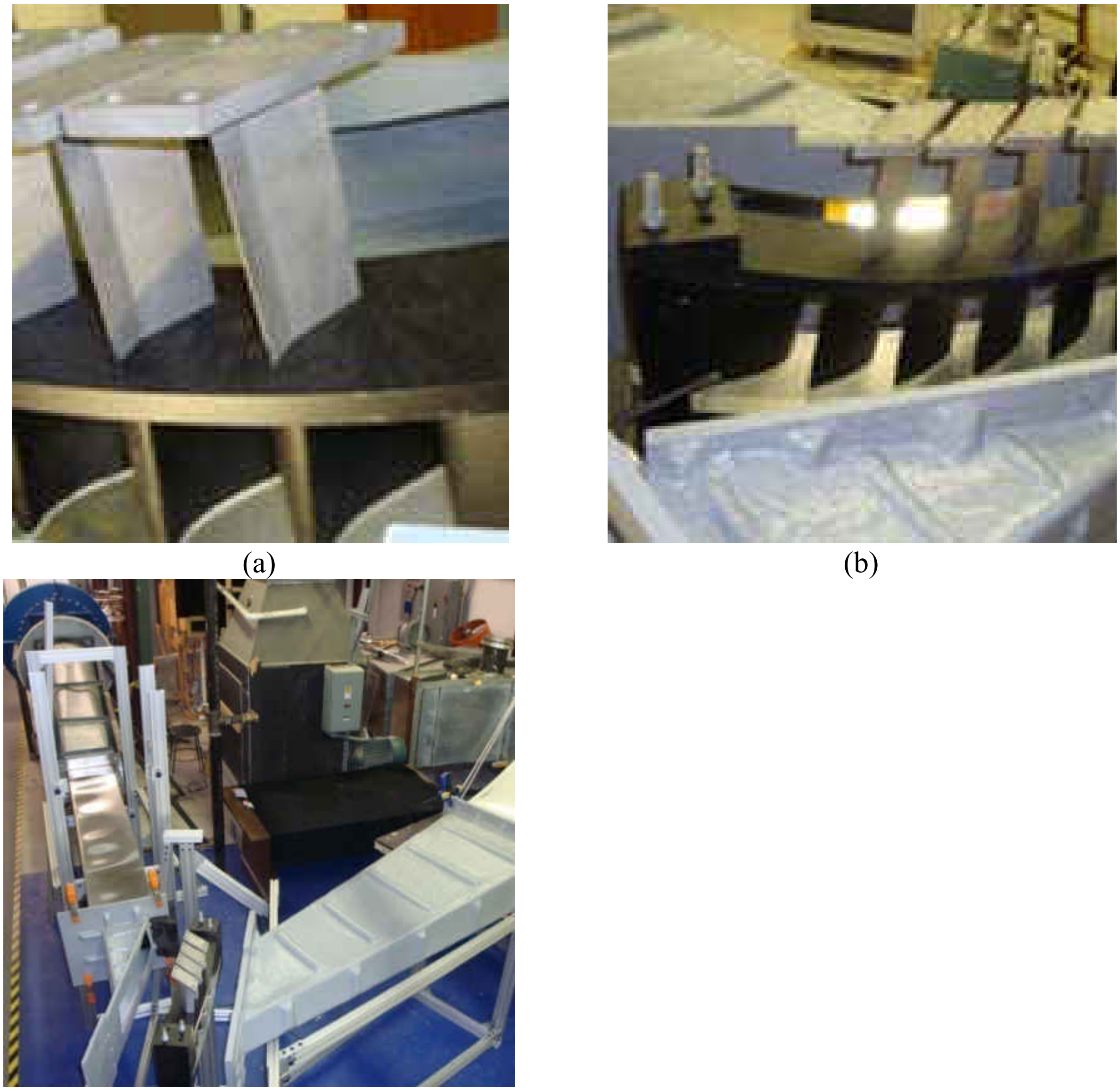

(a) (b)

(c)

Figure 49 Photographs of the current E3 rig: a view from the (a) upstream, (b) downstream, and (c) overall.

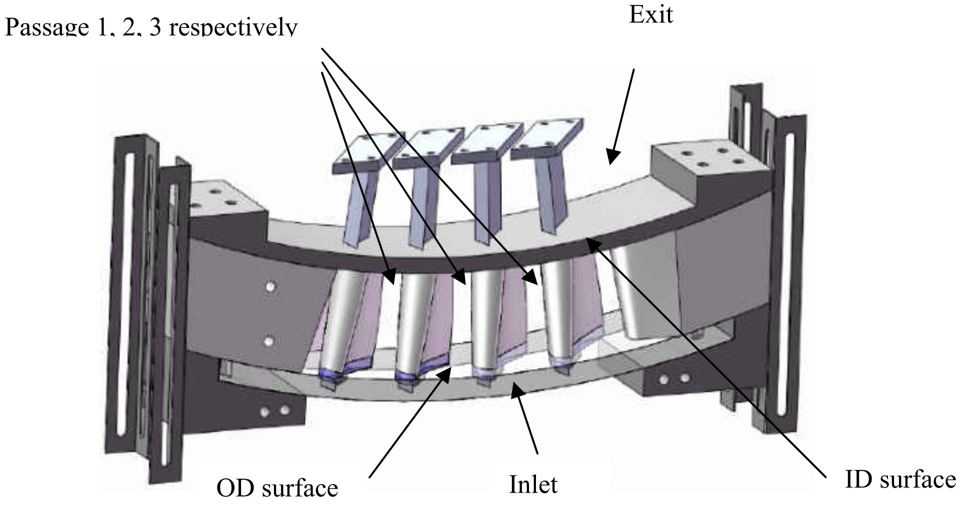

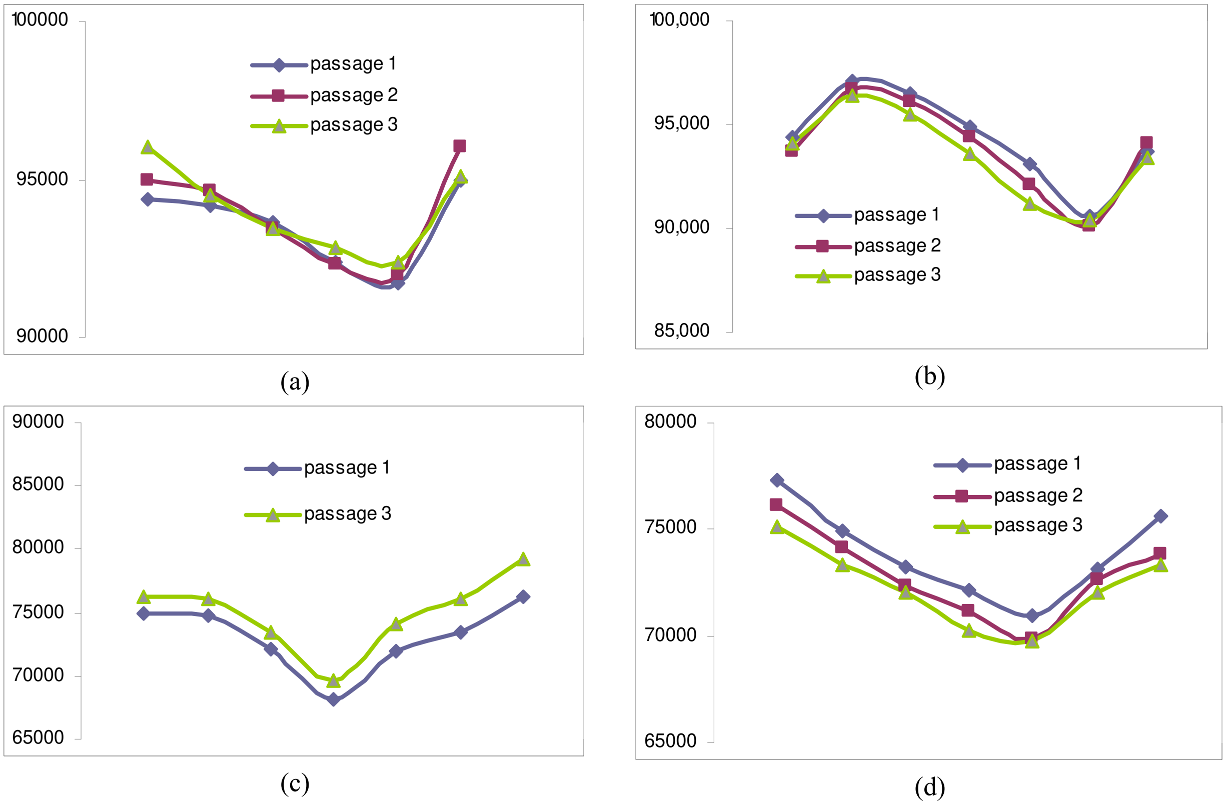

Figure 50 Static pressure distribution on (a) inlet ID surface, (b) inlet OD surface, (c) outlet ID surface and (d) outlet OD surface (Note: horizontal axis are pitch [0 – 100 %]; unit: Nm-2)

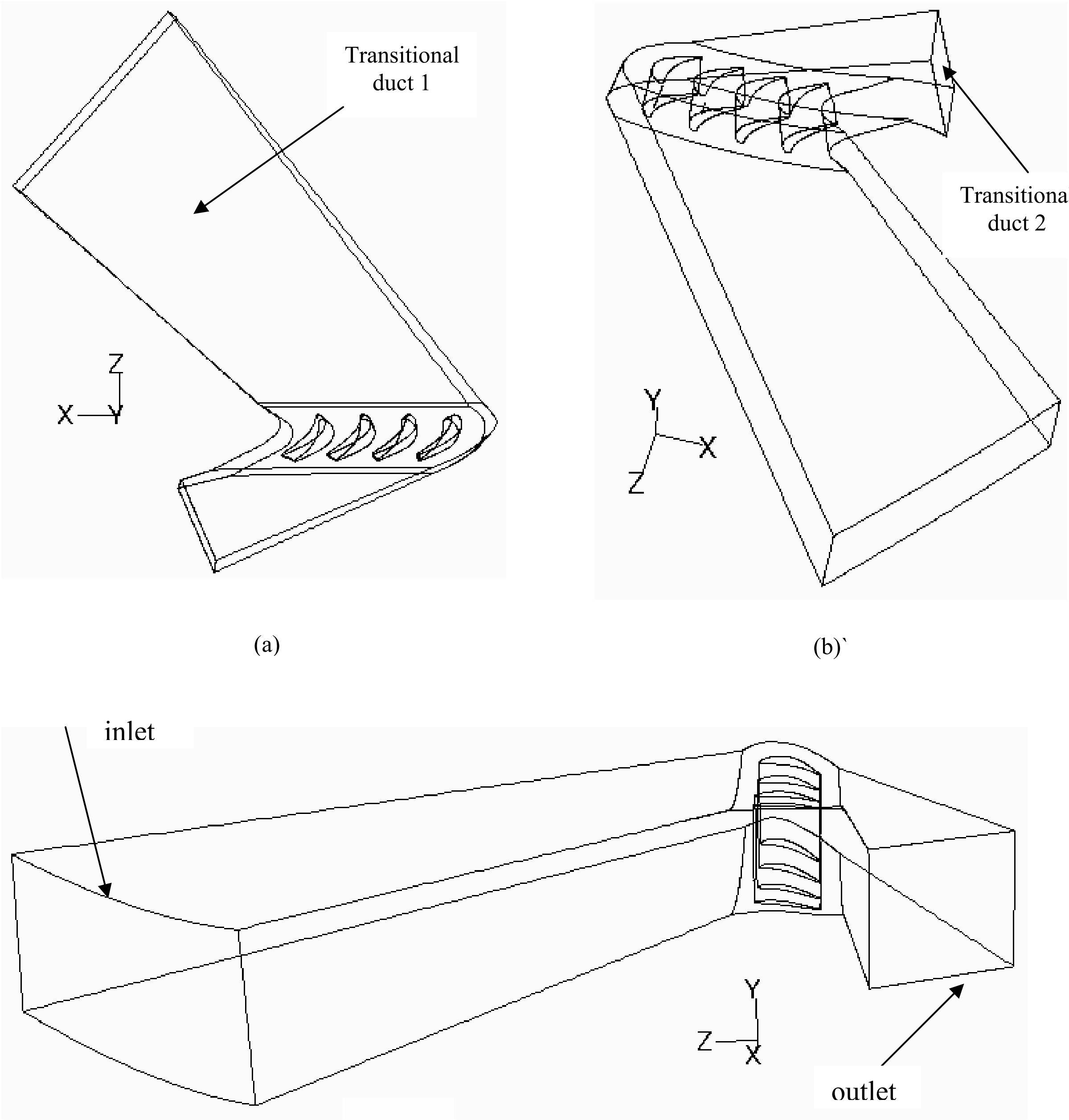

(a)

(b)`

(c)

Figure 51 (a) and (b) Sketch of a complete domain and (c) 3.1 million tetrahedral cell mesh

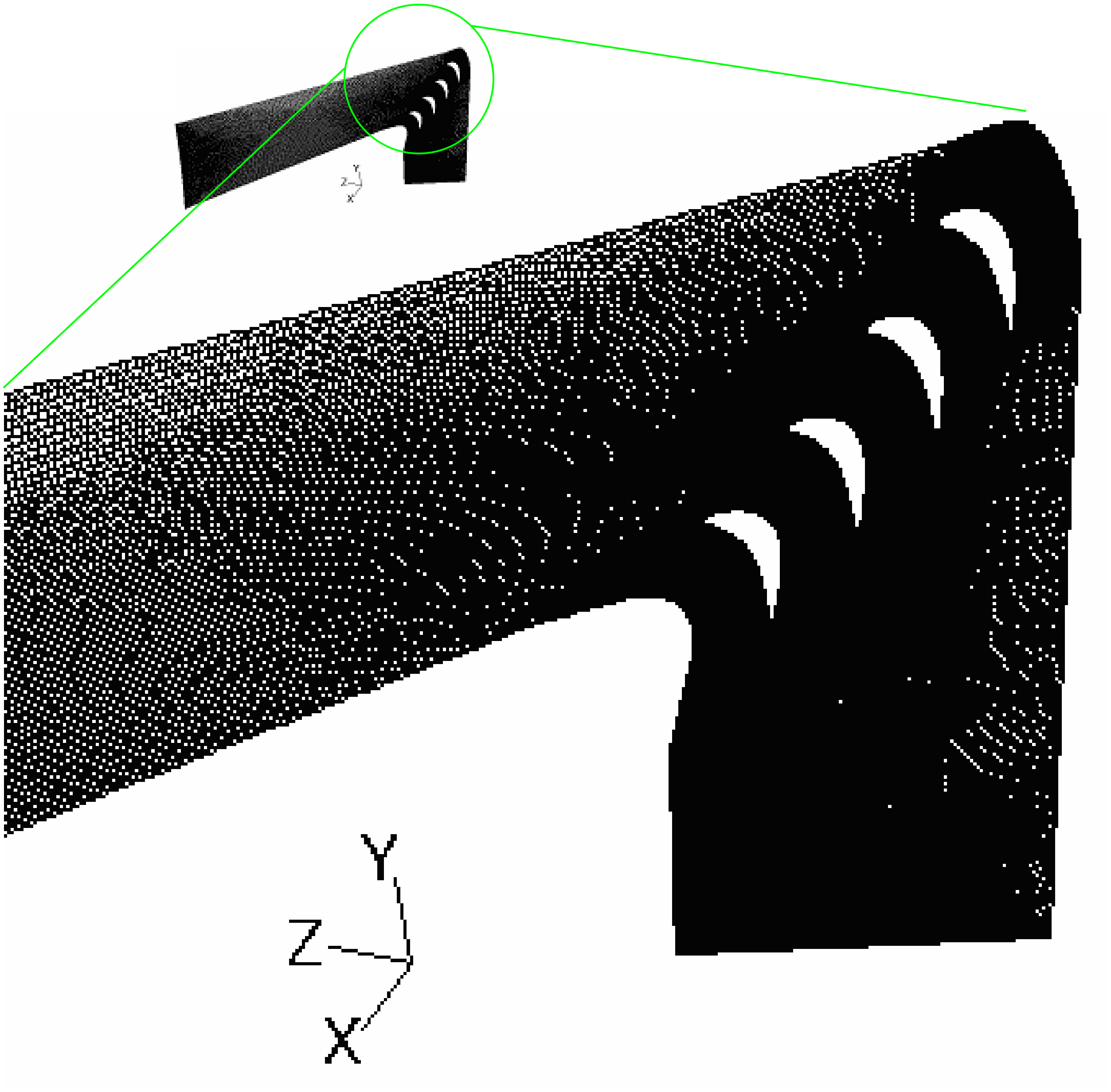

Figure 52 The 3.1 million tetrahedral cell mesh

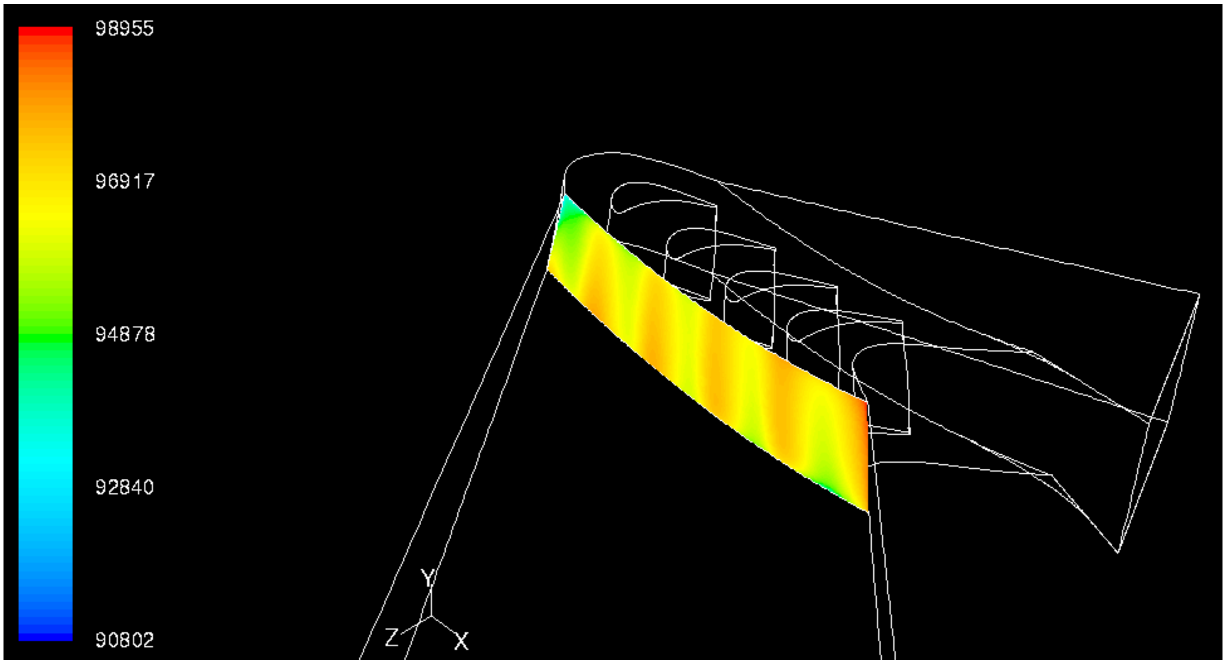

Figure 53 Static Pressure Distribution at the Inlet of the Cascade

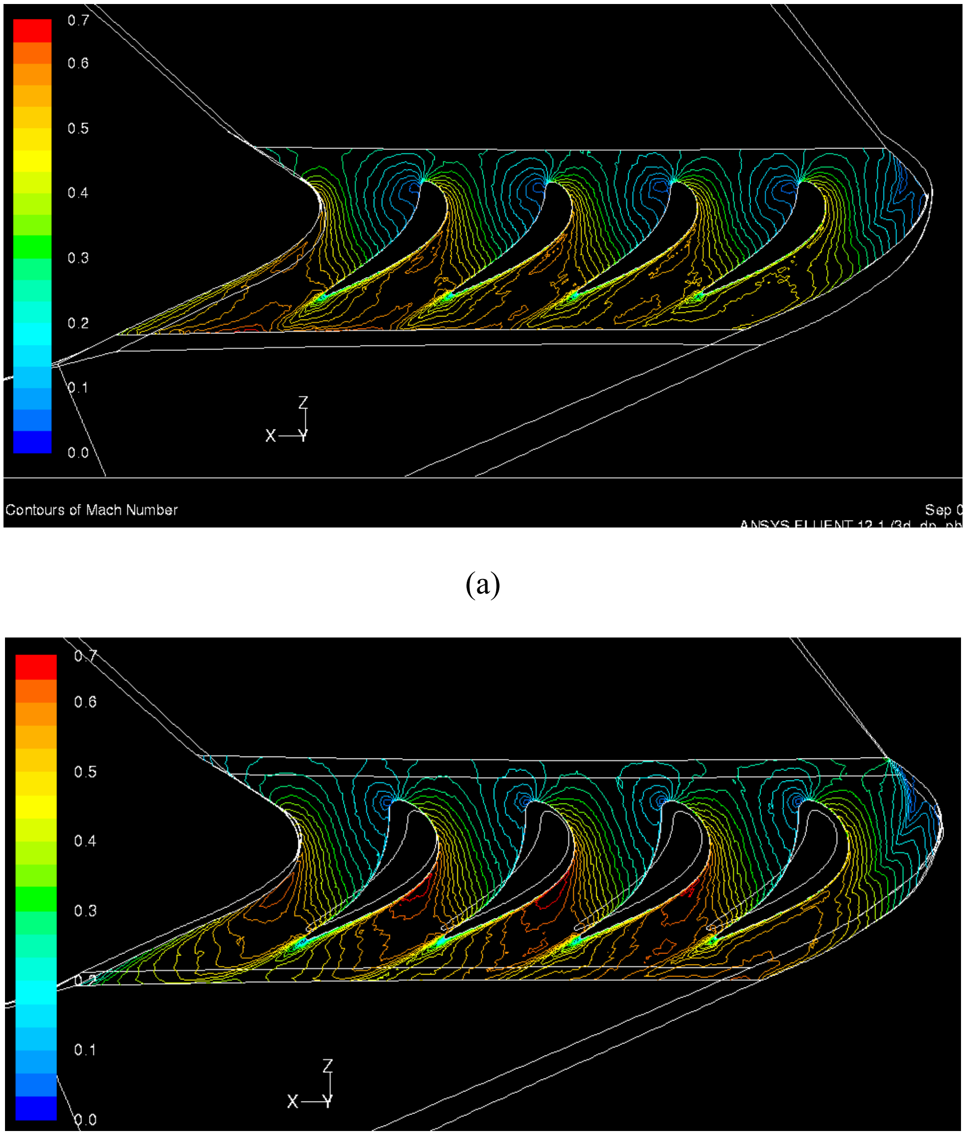

(a)

(b)

Figure 54 Contour of Mach distribution on endwall platform: ID (a) and OD (b)

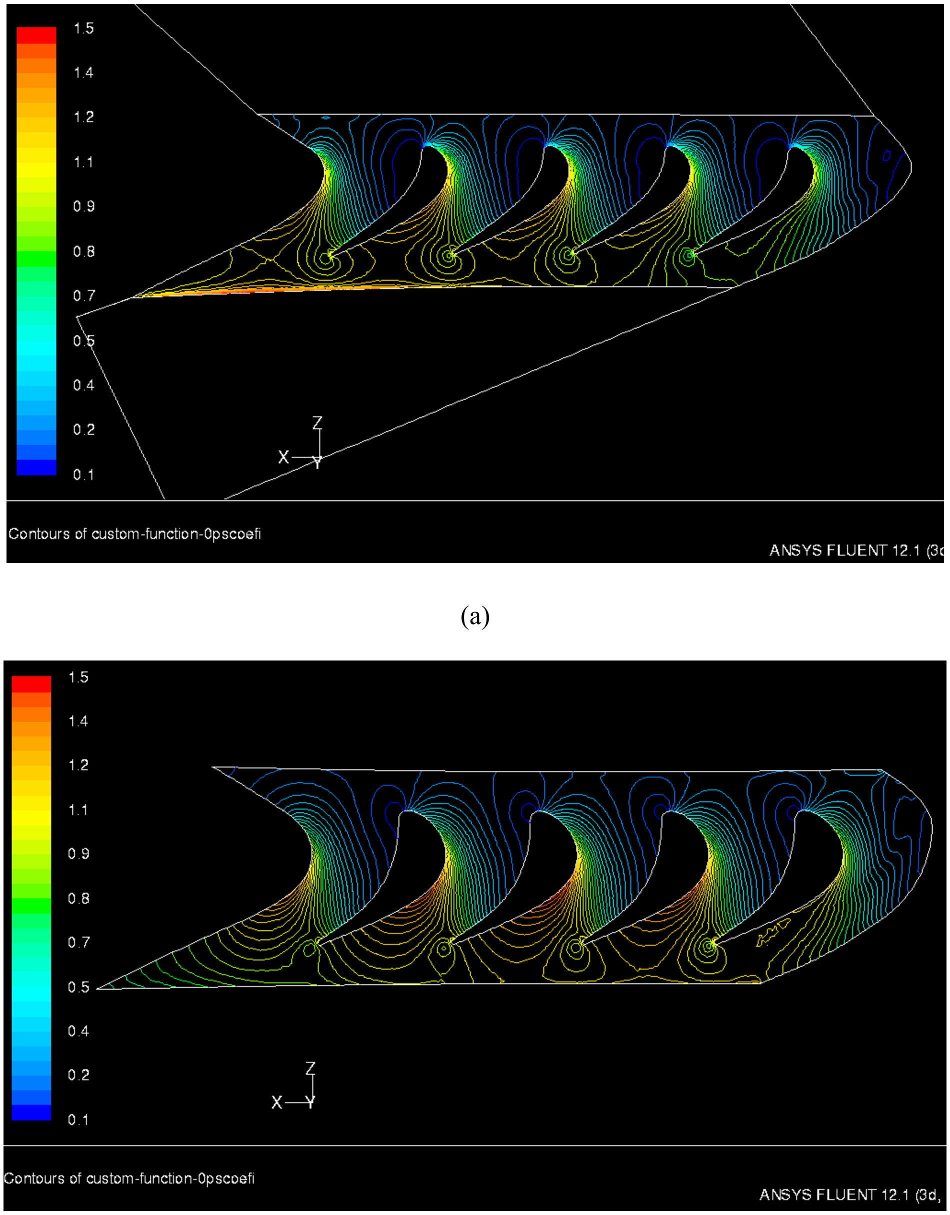

(a)

(b)

Figure 55 Contour of pressure coefficient on endwall platform: ID (a) and OD (b)

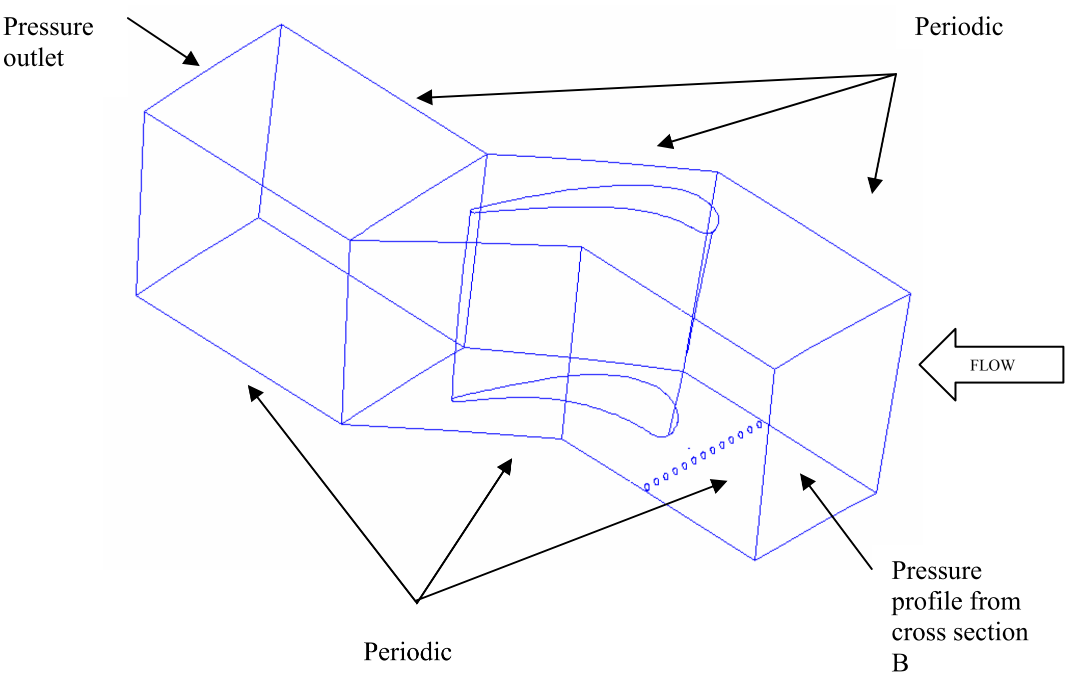

Figure 56 Boundary conditions for the studied domain (without film cooling injection)

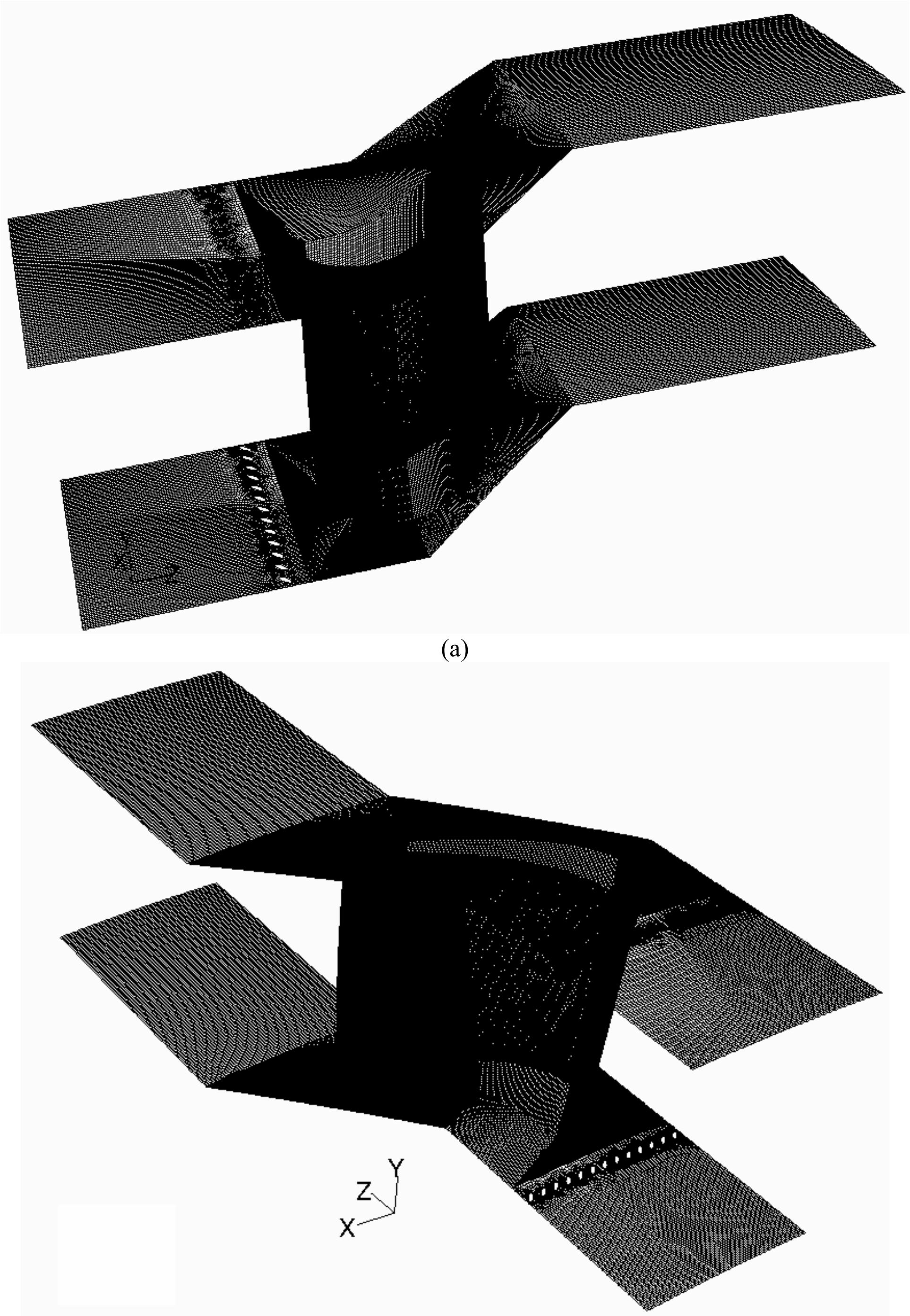

(a)

(b)

Figure 57 Overall view of the hexahedral meshed model (no cool holes): (a) view from pressure side and (b) view from suction side (2.6 million-cell grid is selected to shown here)

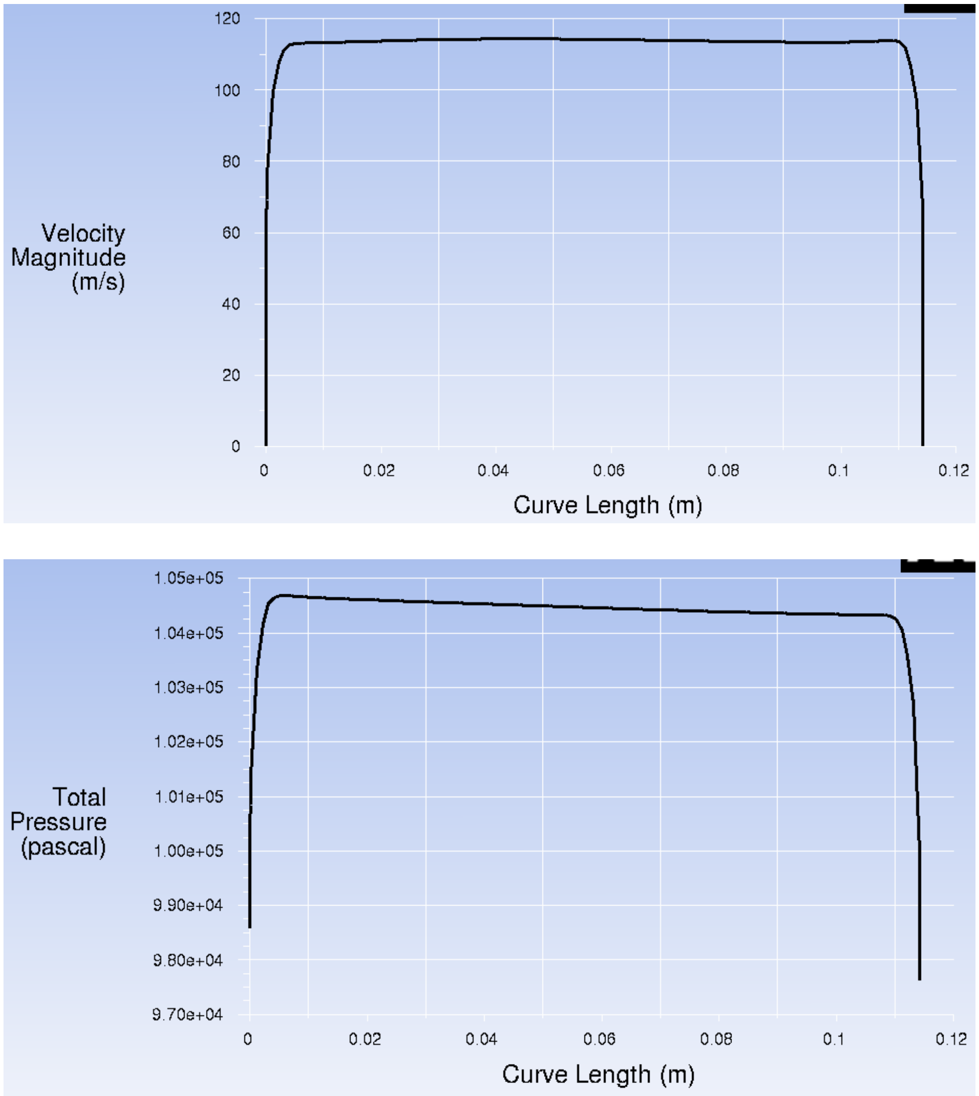

Figure 58 Boundary condition at the inlet versus span-wise direction (note ID: curve length = 0 and OD: curve length = 0.1143m)

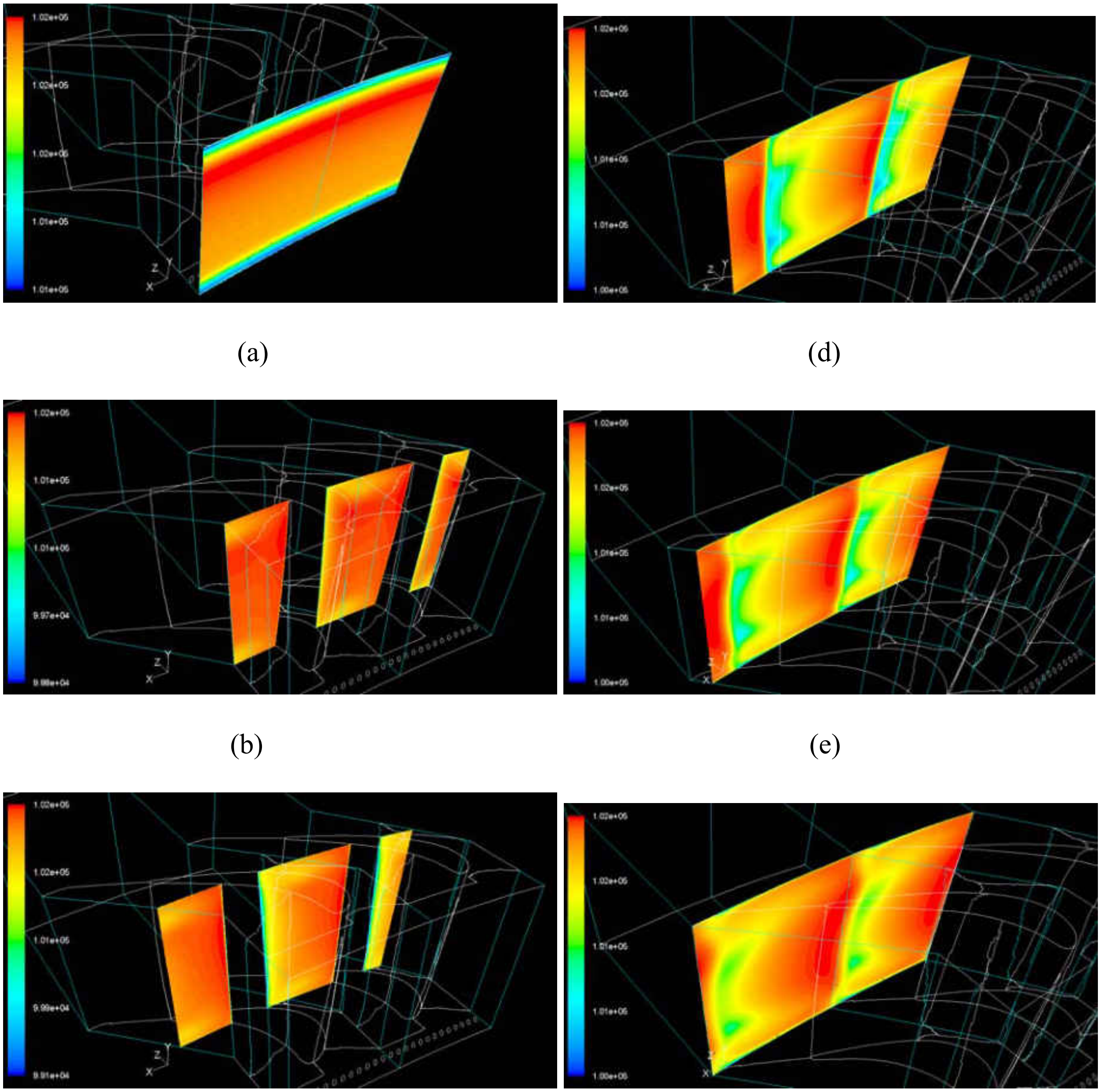

(a) (d)

(b) (e)

(c) (f)

Figure 59 Typical CFD results for the single domain, selected figures obtained from 4.2 million cells case for total pressure loss at several stream-wise locations

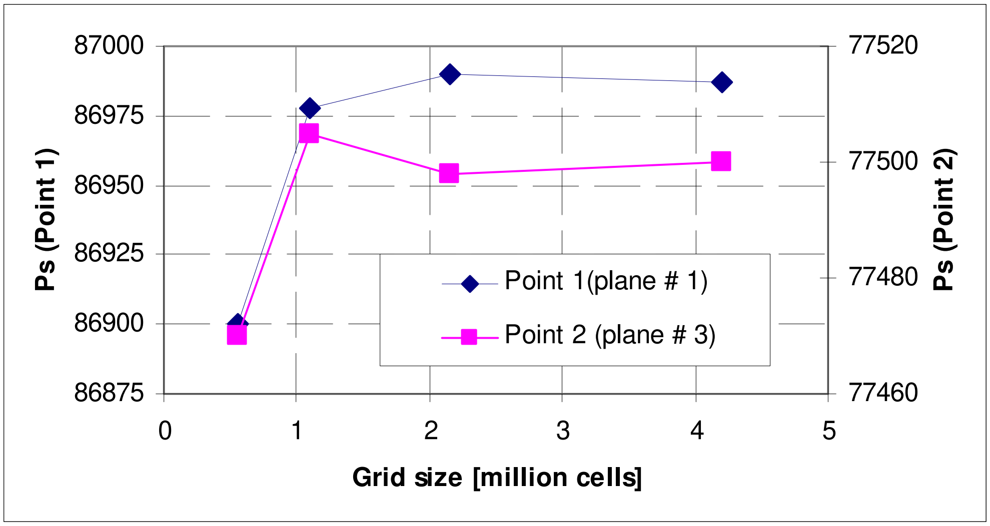

Figure 60 Grid independence study for annular cascade without film hole at several grid sizes

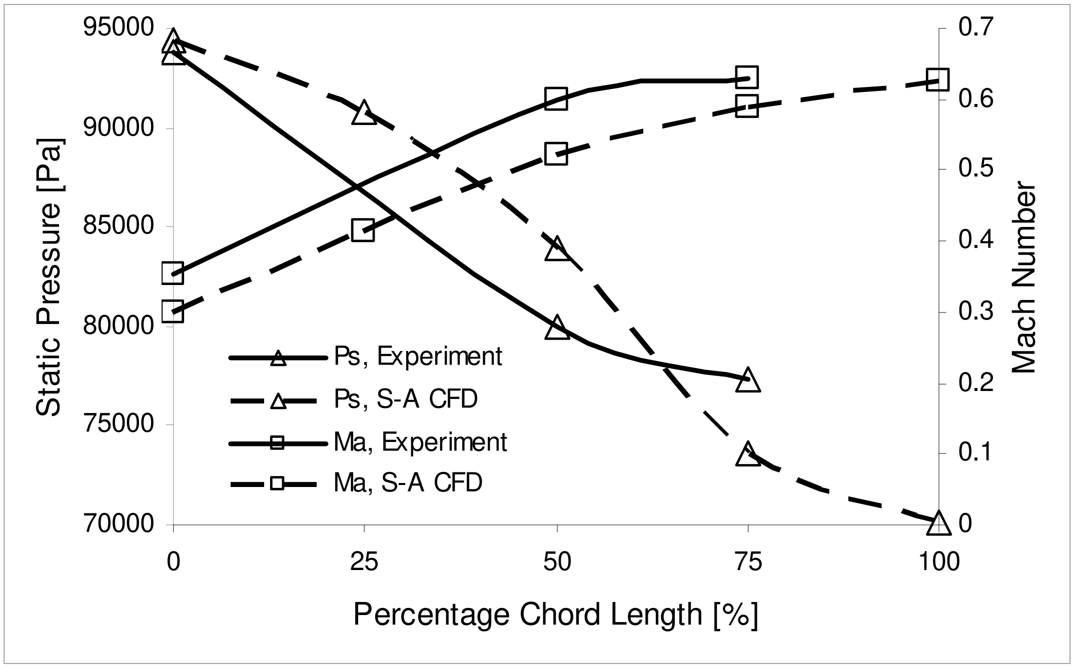

Figure 61 Numerical and experimental comparison on static pressure and Ma number at several streamline locations

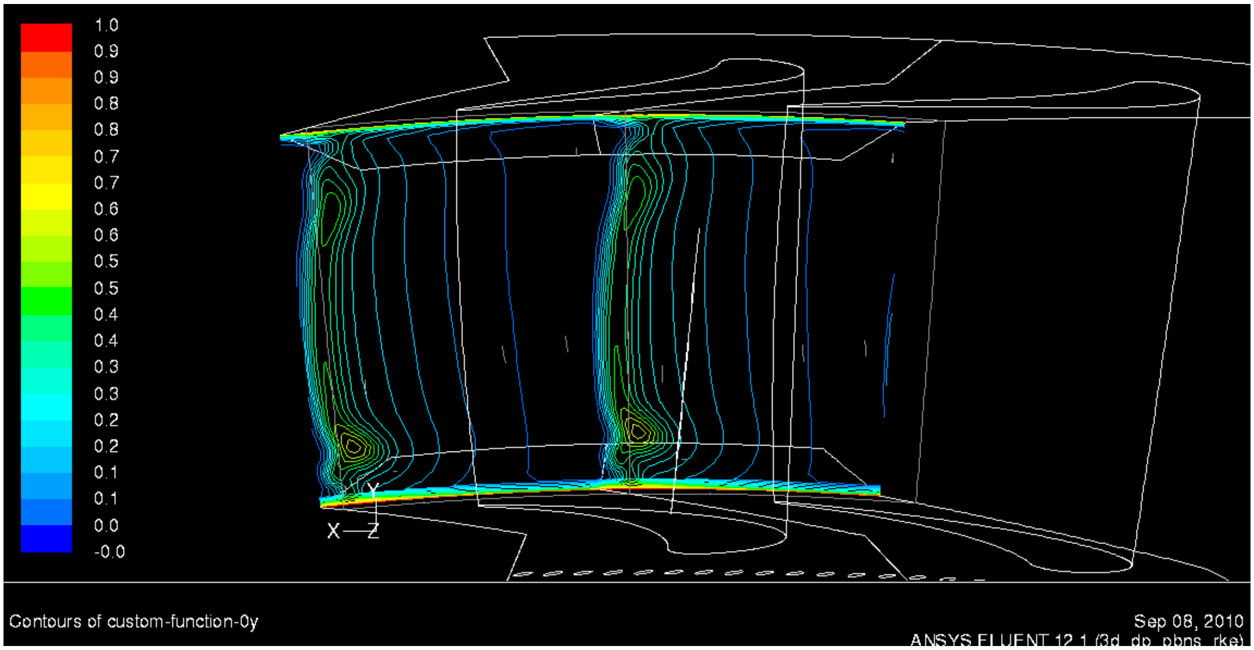

Figure 62 ζ at surface of z/C_a=1.27 or at the location of 27% after the trailing edge (TE)

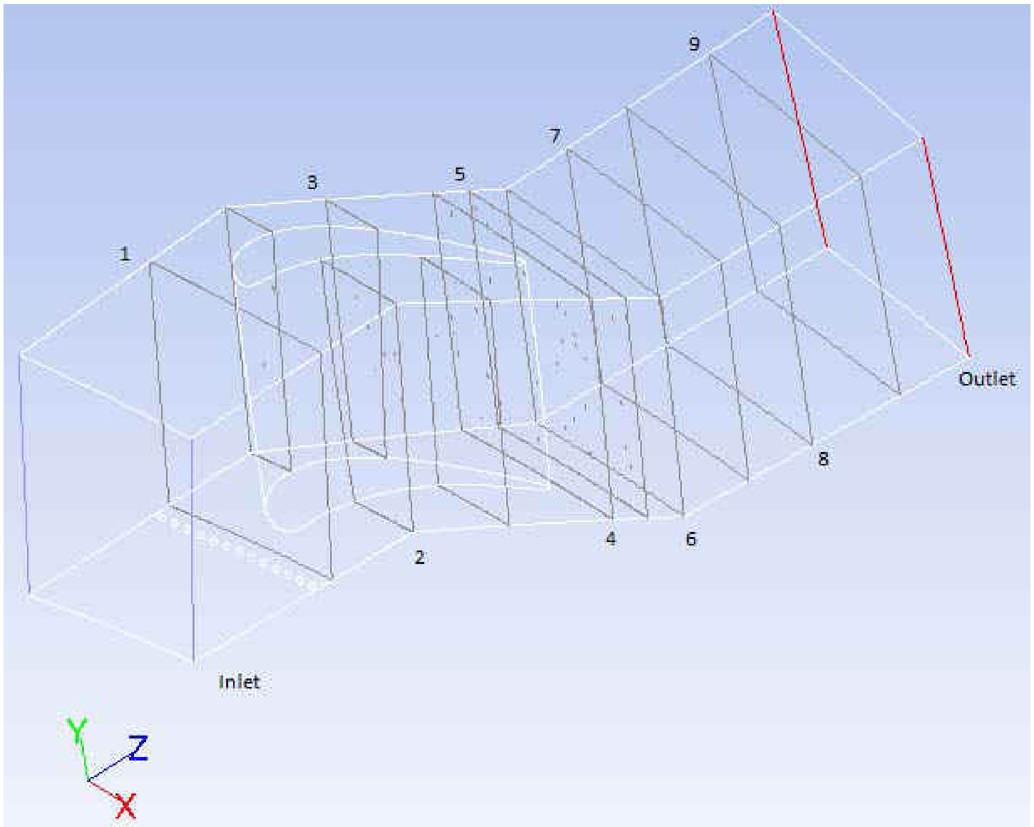

Surface	*z/Ca*	%
Inlet	-1.08	108% upstream
1	0.15	15% axial chord
2	0.36	36% axial chord
3	0.69	69% axial chord
4	1.03	3% downstream
5	1.15	15% downstream
6	1.27	27% downstream
7	1.71	71% downstream
8	2.07	107% downstream
9	2.48	148% downstream
Outlet	2.81	181% downstream

Figure 63 Definition of several selected axial planes for data extraction

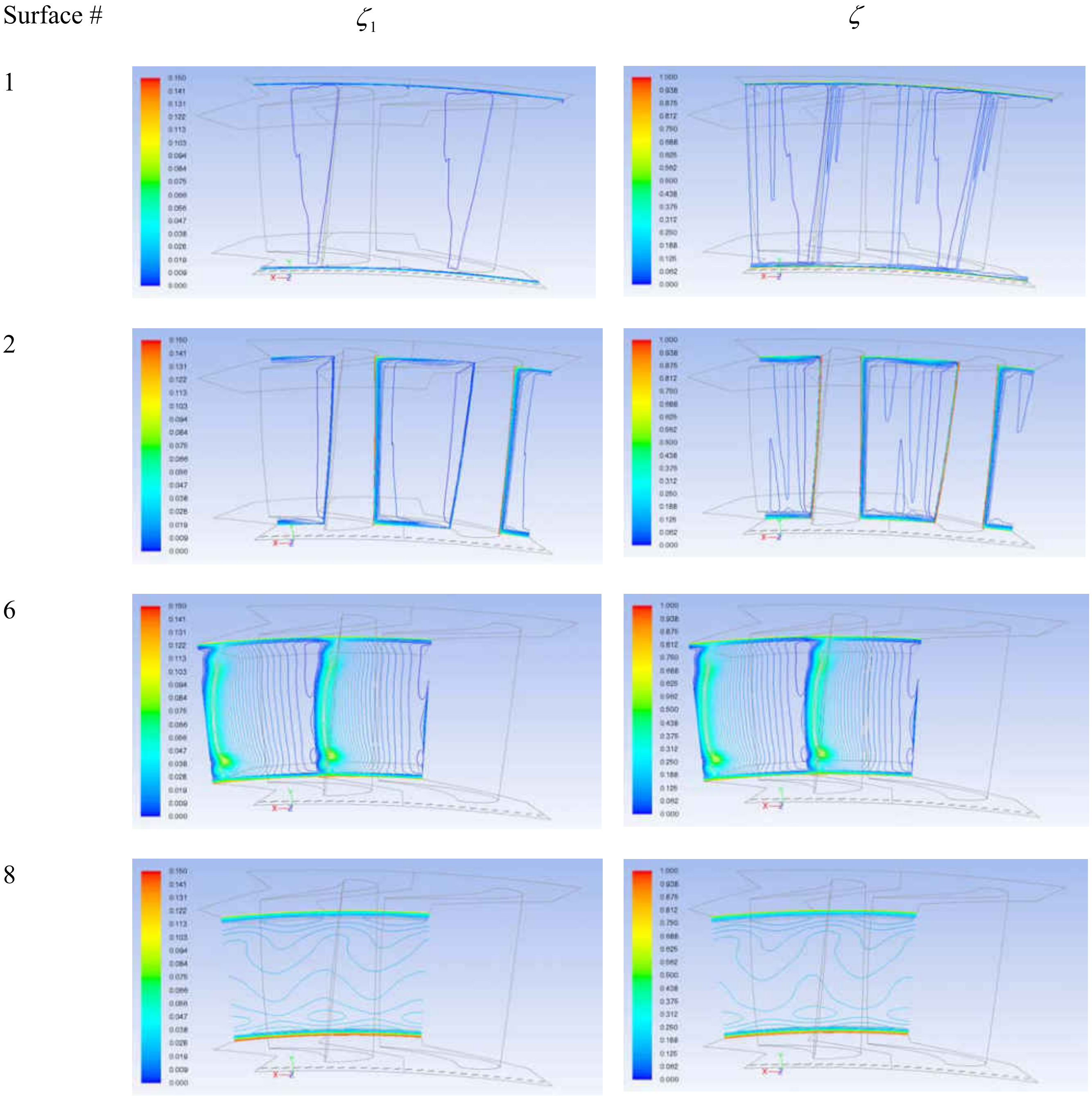

Figure 64 Plots of ζ and ζ_1 at several selected axial planes (refer to Figure 63 for actual location)

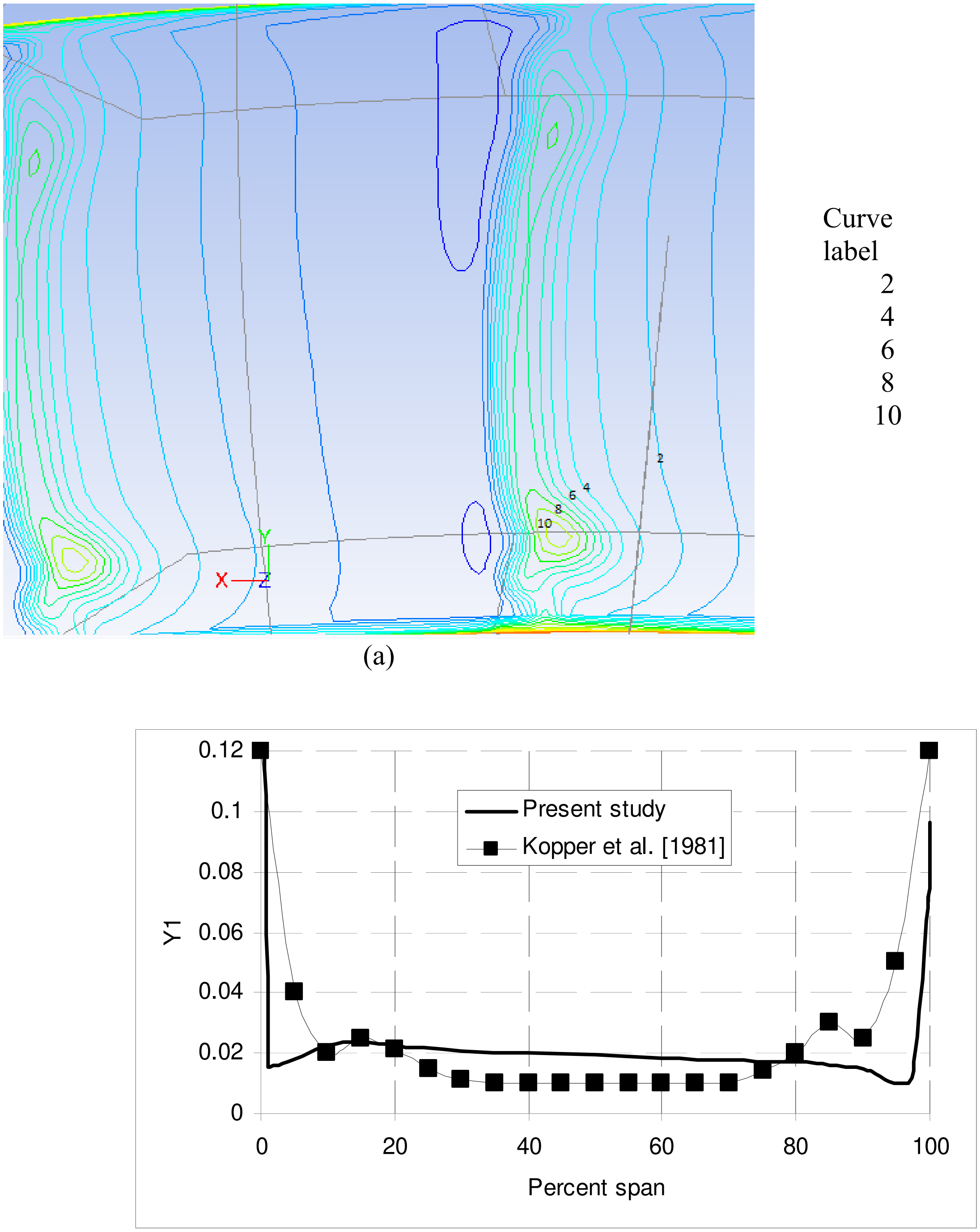

Curve label	
2	.0225
4	.0375
6	.0525
8	.0675
10	.0825

(a)

(b)

Figure 65 Comparison with literature experimental data: loss contour plot (a) and spanwise distribution of total pressure loss (b)

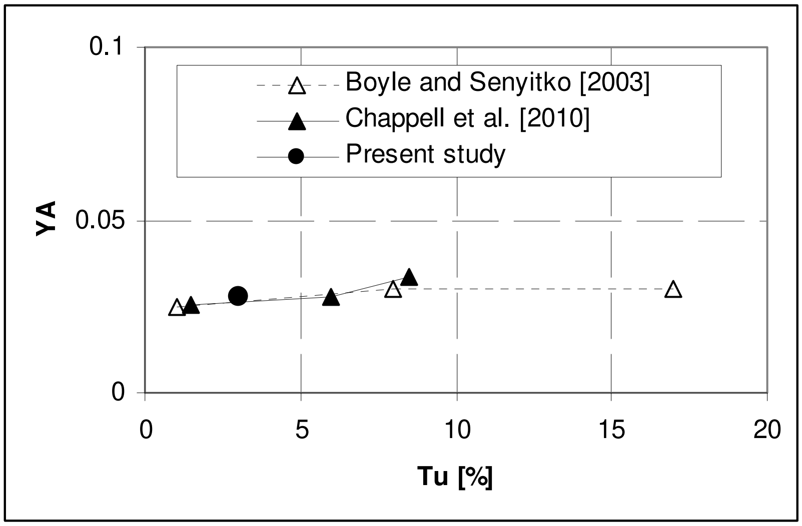

Figure 66 Comparison of area-averaged loss coefficients with values from Boyle and Senyitko (2003) and Chappell et al. (2010)

CHAPTER V. FILM COOLING ON ANNULAR CASCADE PLATFORM: PREDICTION OF SECONDARY FLOW AND FILM COOLING FLOW INTERACTION

The CFD model has been validated against in-house experimental data as well as literature in the previous chapter. Investigation of interaction between film cooling flow and secondary flow inside an annular cascade passage in terms of film cooling performance and aerodynamic loss will be finally discussed in this chapter.

V.1 Problem Description

Again film cooling has been industrially employed on the stagnation region of the stator as shown in Figure 67. To employ film cooling in the low-pressure drop combustor gas turbine is risky since it was believed that the cooling hole in the stagnation region would cause back fires plash, and the hot mainstream may fight with the coolant and actually get into the coolant hole and hence there will be damages. Also, film cooling in the stagnation region is risky since the coolant that comes out of the holes will be washed out by the strong horse-shoe vortices at the leading edges. So to have a better understanding for the impact of secondary flow on the performance of film cooling it is a must that film cooling should be employed in the way that gives least impact on the aerodynamic performance of the cascade.

It is worthwhile to note here that in this current chapter, we simulate film cooling on the hub platform (ID) surface with the hot incoming mainstream (closed loop) wind tunnel. To study the impact film cooling jet on aerodynamics, four blowing ratios, *BR*=0.43, 1.0, 1.9, and 2.4 are selected which cover a practical range in industry practice. Again, blowing ratio is the ratio of mass flux of the coolant over the mainstream mass flux at the axial plane located at the exit of the film hole. In all case mass flux of the mainstream is kept constant and equal to the mainstream mass flow rate in Chapter 5 (0.7154kg/s). So the mass flow rate of the coolant is varied accordingly to the blowing ratio. On the other hand, to study the impact of aerodynamic on the film cooling performance, three midspan flow angles, Φ=33^{o}, 43^{o} and 53^{o} with respect to the midspan airfoil profile (or corresponding to three midspan incident angle, i=-10^{o}, 0^{o}, +10^{o}), have been investigated. Table 15 shows the test matrix which will be focused on in this chapter.

Table 15 List of all case in this study

Flow Angle, Φ_{ms} (midspan incident angle, i_{ms}) Blowing ratio, *BR* (*MFR* %)	33^{o} (-10^{o})	43^{o} (0^{o})	53^{o} (+10^{o})
0 (0 %)	M00A33	M00A43	M00A53
0.43 (0.447%)	- - -	M10A43	- - -
1.0 (1.03%)	M10A33	M10A43	M10A53
1.9 (1.96%)	- - -	M19A43	- - -
2.4 (2.5%)	M24A33	M24A43	M24A53

V.2 The CFD Model and Solution

V.2.1. Choice of design variables

The film cooling model is developed and based on the one which was constructed and validated from the previous chapter. Again, the model represents only one annular segment out of 72 in total (5^o circumferential angle segment). Each passage has 13 film holes which are oriented 43^o with respect to the axial direction (also known as a compound angle, β) and 30^o of inclination (or injection, α) angle. The film cooling hole with D=2.0 mm has a length-to-diameter, L/D=10 and pitch-to-diameter, p/D=3.0 as typical aircraft film cooling application from Kapat (2009).

Distance from the cooling row to the leading edge (LE), δ is selected inside a practical range. As shown in Figure 68a, it is practical in gas turbine engine that δ/D is about 1*d*-2*d* upstream relative to the blade leading edge, Kapat (2009). Hence, δ is selected from 1*d* to 2*d* (with *d*~14.3mm). In this current study, a row of film holes is assigned at z/C_a=26.8% upstream (or z/Ca=-0.268), are injected at 30^o injection angle and oriented at 43^o compound angle with respect to the axial direction.

A coolant box is also included to capture the contraction effect at the entrance of coolant (at the inlet into the cooling channel). Johnson et al. (2010) had a sensitivity study on the coolant box parameters and found that the coolant is extremely important so that each CFD model should include the coolant box. They varied the box height (direction from coolant box inlet to the coolant entrance to the film channel) from 4D, 8D, and 12 D; and box length (axial direction) also from 4D, 8D, and 12D. They concluded that there is not much different on film cooling performance when these 2 factors were varied from low level to high level. However, the cooling box has to be modeled, since film cooling performance is changed tremendously from the with-cooling-box case compare to the without-cooling-box case.

The author decided to select 12D for the coolant box height and length for the sake of safety factor (note: the width of the coolant box is the same as 1 pitch long as the cascade segment). Figure 69 depicts all the parameter for overall hub (ID) endwall film cooling model. Main flows parameters are kept the same as in Chapter 5

V.2.2 The Mesh Model and Solutions

In this present study, the turbulence realizable *k-ε* with enhanced wall treatment is chosen. A coolant box with 13 film cooling channels has been integrated into the numerical model from the previous chapter. Boundary layers are attached to all walls to capture the wall effect. Y+ value was made sure to be equal to unity on the hub (ID) and the shroud surface (OD). At the result, there are 8.16-million-cell grid, which was created to satisfy the entire above requirement with reasonable cell skewness and aspect ratios. Again, it is the secondary flows that promote the coolant jet lifting from the OD endwall, where the cooling jets are integrated into the horse-shoe vortex and passage (the horse-shoe pressure side leg turns into the passage vortex). The grid is created in Gambit and is shown in Figure 70. Fluent is again employed to conduct the CFD analysis with steady compressible scheme. Realizable *k-ε* viscous model, which is paired with enhanced wall treatment, is the viscous model for the current numerical simulation. Residuals are set to be less than 10^{-4} for flow and turbulence parameters, but 10^{-6} for the energy equation.

Marking and patching technique was employed extensively for the initialization of temperature and total pressure in the flow field (for example: coolant temperature is initially assigned for the region below the ID surface when there are 13 coolant pipes and coolant plenum box, and mainstream hot temperature is assigned for the rest).

Typically, it takes 10-15 wall-clock hours with an 8 nodes combined with 8-pack Ansys 12.1 to reach the required converging criteria within 5K to 8K iterations. Five "main" cases corresponding the BR=0, 0.4, 1, 1.9 and 2.4 were pilot runs. The settings and initialization data for the other cases were read and interpolated from the pilot cases. At a result, the computing time was reduced 2 to 3 times. All the runs were performed in the Parker Hannifin central computing center located at Mentor, Ohio, USA. For the next section, both film cooling effectiveness and pressure loss coefficient will be extracted pitch-wise as shown in the Figure 72.

V.3 Impact of Secondary Flow on Film Cooling Performance

Four blowing ratios, BR=0.4, 1.0, 1.9, 2.4 with three midspan angles of attack, i=-10^{o}, 0^{o}, +10^{o} form a testing matrix to gain a better understanding of the effect of secondary flow inside the annular passage on the film performance. With the right blowing ratio, the injected film jet will spread out and form a thin blanket to cover the downstream surface, which separates the surface from the hot mainstream. In practice, there are usually several rows of platform film holes axially located inside the passage from the leading edge to the trailing. Only film cooling at the stagnation region is investigated in this study, therefore the temperature distribution of interest on the ID surface is boxed by axial planes z/C_a=-0.15 and z/C_d=0.69. Film cooling effectiveness is averaged along the circumference direction (similar as in Chapter 3), again it is defined as in the Equation 5.1, and spatially-averaged of film cooling effectiveness is also defined as in Equation 5.2

$$\overline{\eta}(z)=\frac{\int \eta(z,s)\;ds}{\int ds} \tag{5.1}$$

$$\overline{\overline{\eta}}=\frac{\int \eta(z,s)\;dz\,ds}{\int dz\,ds} \tag{5.2}$$

Selected pitchwise-averaged film cooling effectiveness is validated with the second configuration (CONF2) from Barigozzi et al. (2006). They experimentally studied film cooling on flat endwall cascade. From their experimental setup, there are 14 conical film holes to form a row which is located at z/Ca=8% upstream from the airfoil leading edge. Geometric parameters are L/D=10.7, α=30° with 20° conical flare angle. They performed experiments for the coolant to mainstream mass flow rate ratio from 0.5% to 2.5% which is defined as in Equation 5.3. It is good to note here that *BR* is often defined as the coolant to mainstream mass flux ratio in the literature as well as in this current study. Table 16 is prepared for comparison purpose between several selected cases and corresponding cases from Barigozzi et al. (2006)

$$MFR=\frac{\dot{m}_c}{\dot{m}_\infty}\times 100\% \tag{5.3}$$

Table 16 Selected cases from the current study versus the study from Barigozzi et al. (2006), and Knost and Thole (2003)

	Current study	Barigozzi et al. (2006)	Knost and Thole (2003)
Hole shape	cylindrical	Conical (20^o flare angle)	
L/D		10.7	
Number of hole, N	14	13	
Angle of attack, ψ	43^o	30^o	

As seen from Figure 73, for a specific flow angle, for example $\Phi=43^o$, coolant jets perform the best with BR=1 and gradually reduced with increase of blowing ratio due to jet liftoff. The injected coolant coming out with relatively higher momentum than the mainstream is lifted into the free stream and does not have a chance to "hug" the downstream surface. Obviously, this matches the trend obtained from experimental work from Barigozzi et al. (2006) which is also shown in the same figure. Spatially-averaged film cooling effectiveness is also validated with the literature as shown in Figure 74. Four blowing ratios are shown, and again the trend which is film performance is nonlinear with respect to BR, is also observed from Barigozzi et al. (2006).

To see how the flow angle of the incoming flow (mainstream) affects the film cooling performance, $\bar{\eta}$ was plotted against flow angles ($\Phi=33^o$, 43^o, and 53^o) as shown in Figure 75 (BR=1) and Figure 76 (BR=2.4). When the mass flux of the coolant equals to the mainstream's (blowing ratio of unity), increasing angle of attack will increase $\bar{\eta}$ from the location where the film jets are injected up to $z/C_a=0.1$. There will be no difference between $\Phi=33^o$ or $\Phi=43^o$ since the coolant has formed a good "blanket" underneath the passage vortex, which is developed from the pressure-side leg horse-shoe vortex. When the mainstream flow angle is at 43^o, which is the same with the compound injection angle of the film jet, the mainstream has a tendency that it splits the coolant into 2 sides of the airfoil (suction side and pressure side). When Φ decrease from 43^o to 33^o, the mainstream will have a tendency to split more coolant into the pressure side, where a large amount of coolant will get onto the PS-leg of the horse vortex which starts at the LE then traverses clockwise and to the SS of the left-neighbor airfoil.

In the other hand, when Φ increases to 53^o, the mainstream seems to make coolant split more into the SS of the airfoil which is then less affected by the strong passage vortex, and actually is helped by the SS-leg horse vortex to stick more onto the platform up to 10% of the axial chord length. But, this larger amount of coolant will be lift off by the SS-leg horse vortex of the airfoil, which start to take off into the midspan after z/C_a=0.1, which also brings that large amount of coolant onto the midspan. At a result, $\bar{\eta}$ drops tremendously for M10A53 in the Figure 75.

At higher blowing ratio, BR=2.4, the momentum of the coolant easily dominates the momentum of the mainstream, as it has been shown in the previous chapters that the coolant has a tendency of shooting straight to the midspan area. From Figure 76, when Φ is decrease from 43^o down to 33^o, a larger amount of coolant is split into the pressure side of the considering airfoil with relatively strong momentum, which then get twisted with the PS-leg horse-shoe vortex into the space, and as a result performs the least among the three. On the other hand, if Φ is increased to 53^o, larger amount of coolant is split into the SS of the considered airfoil, but the extra amount with a relatively high momentum will get into the space which yields little improvement in performance compared to Φ=43^o.

Another way to look at the effect of aerodynamics on the film cooling performance is to consider the film performance with respect to the angle of attack at four different blowing ratios as shown in Figure 77. Blowing ratio of 1 gives the best film performance among the four. Also, it is obvious that one can gain up to 17% ($\overline{\overline{\eta}}$=0.3 to 0.35) if one switches Φ from 33° to 43° for high blowing ratio, but increasing Φ further will not gain much. On the other hand, for "optimum" blowing ratio, there is nothing gained in term of $\overline{\overline{\eta}}$ if one increase Φ from low level of flow angle (33°) to middle level (43°), but there will be a loss if one keeps increasing the flow angle Φ.

V.4 Impact of Film Cooling on Aerodynamic Performance of the Annulus Cascade

Mass-weighted average pressure loss coefficient, ζ on the axial plane z/C_a=1.27 is studied. Typical ζ for all 4 blowing ratios are briefly introduced in Figure 78. For comparison purpose, ζ is laterally averaged in the pitchwise direction, named $\overline{\zeta}$ which is defined as in Equation 5.3.

$$\overline{\zeta}(r) = \frac{\int \zeta(r, s) ds}{\int ds} \tag{5.3}$$

where *ds* varies from the left periodic surface to the right periodic surface of the annular passage. Figure 79, 80, and 81 shows the variation of $\overline{\zeta}$ with respect to blowing ratio at different incident angles: *i*= -10°, -10°, and +10° respectively. From those three plots, in general, at higher incident angles, more aerodynamics losses occur at the wedge area downstream of the airfoils. Figure 82 indicates that with the middle level of incident angle (i=0°) without film cooling, the loss was minimal, and it gains its maximum value with the highest incident angle (i=+10°)

As seen in Figure 83, the film cooling jets in case M10A53 which are injected with a 43° compound angle to form a nice film on the top of the hub platform as the pressure loss coefficient is on top of the baseline curve from 40% span to the shroud surface (100% span). On the other hand, at a certain blowing ratio, if one varies the incoming angle of the mainstream, the laterally-averaged pressure coefficient will behave as in the Figures 83, 84, and 85. With Figure 84, one can conclude that BR will not increase the aerodynamics losses much if BR increases from the low level of BR (0) to BR=1.0, but pressure loss will tremendously increase if one starts to exceed from BR=1.0.

Figures

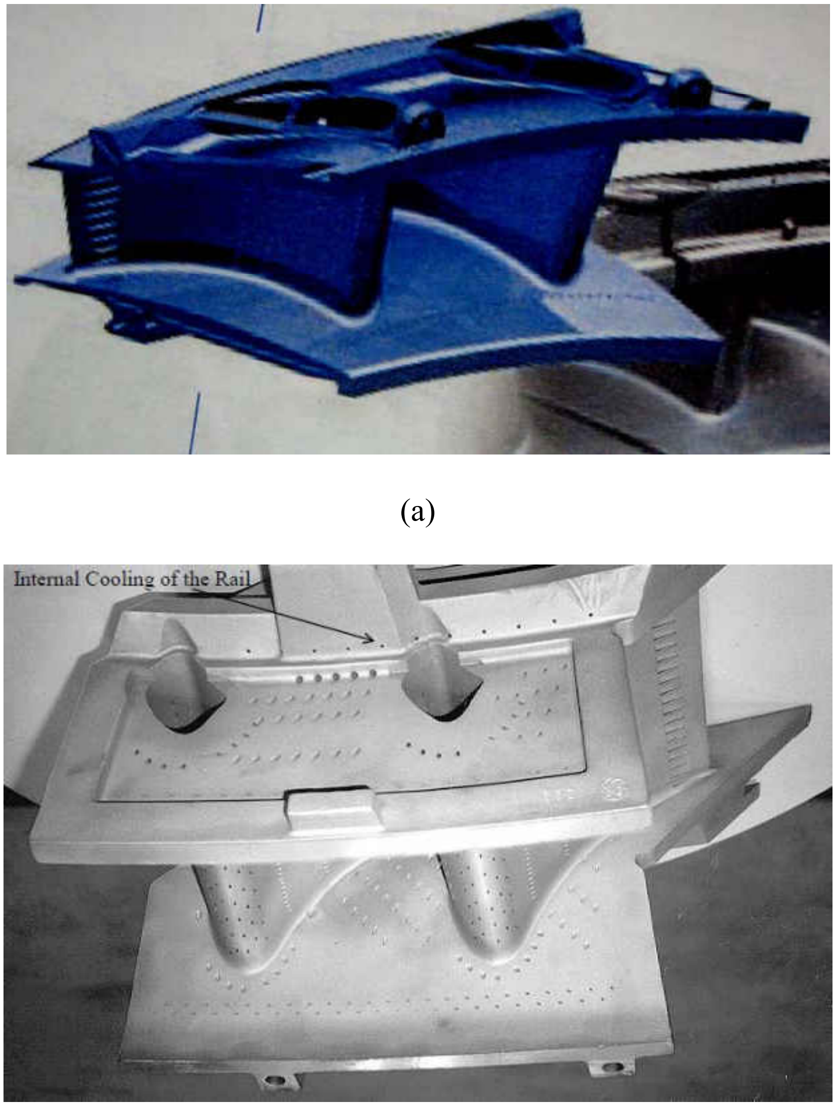

(a)

(b)

Figure 67 Application of film cooling on the stator stagnation region, after (a) GE web site (2010) and (b) Freidrich (1997)

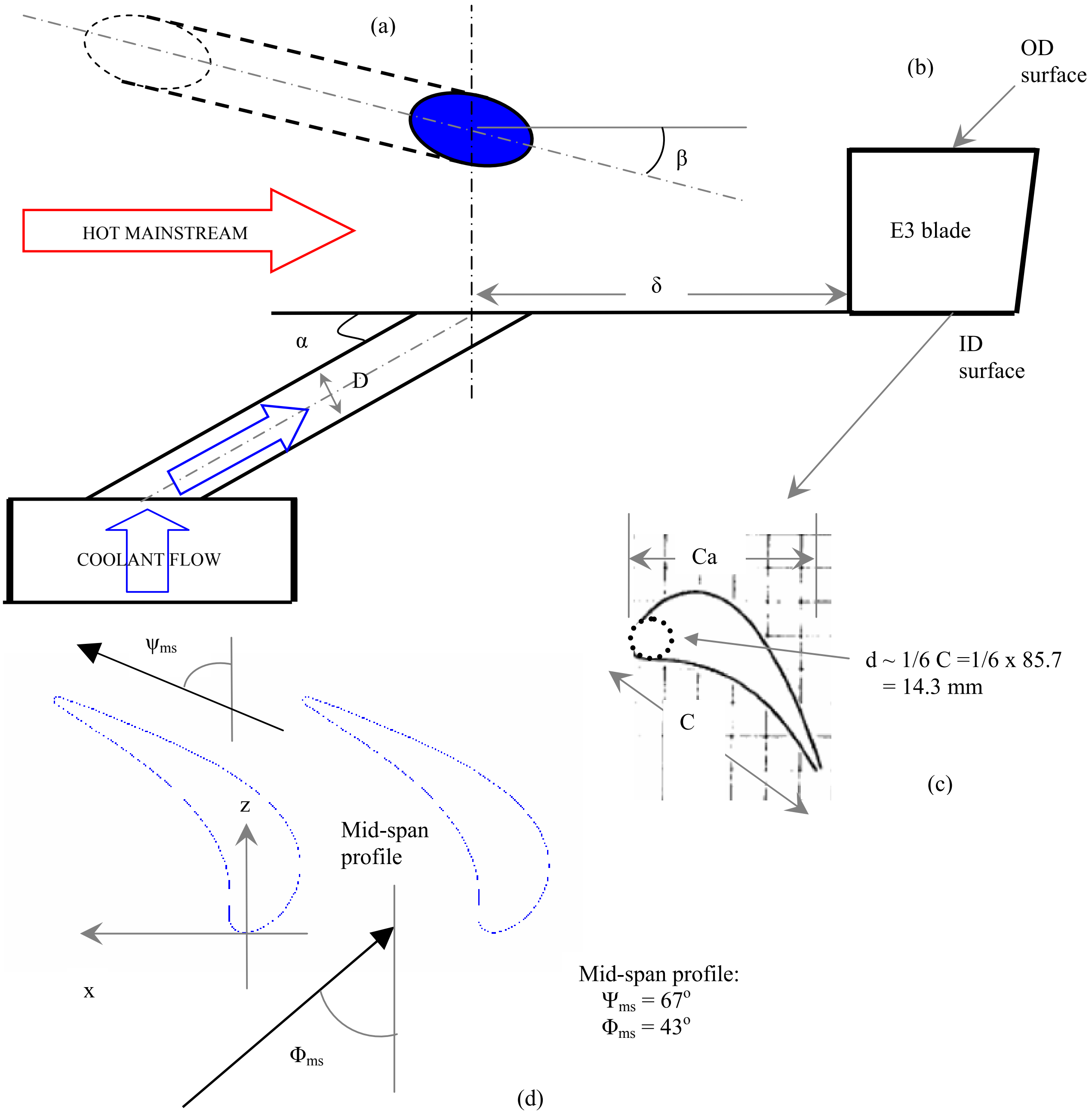

Figure 68 (a) Stagnation region film cooling (not draw to scale), (b) 1st stage E3 turbine blade, (c) approximation of the leading-edge-fillet diameter, and (d) definition of Φ and ψ on the mid-span profile

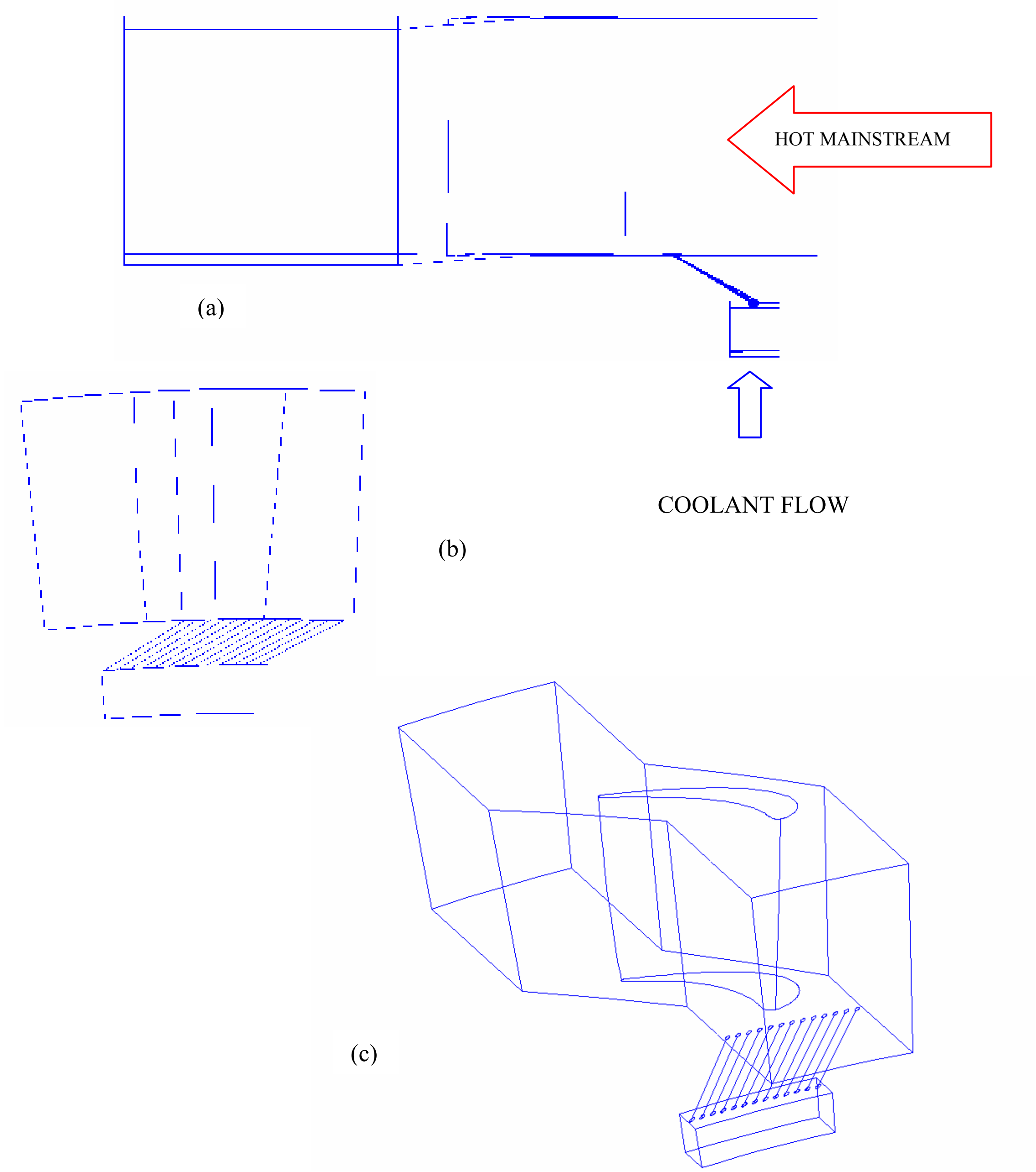

Figure 69 Sketch of hub-endwall film cooling model: (a) side view, (b) look after-forward view and (c) isometric view

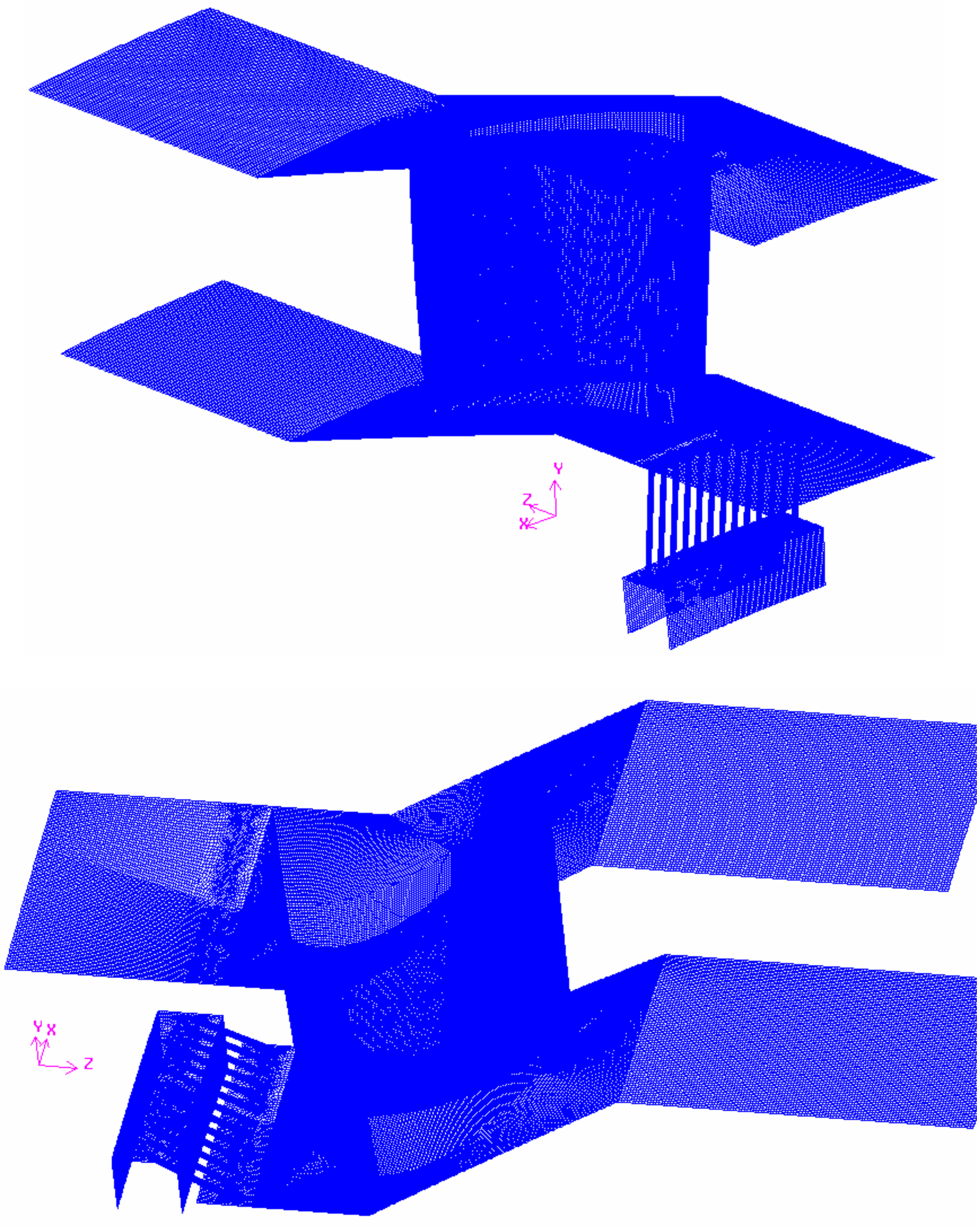

Figure 70 Mesh grid for film cooling in the stagnation region in an annular cascade (8.16 million cells mesh is selected to show)

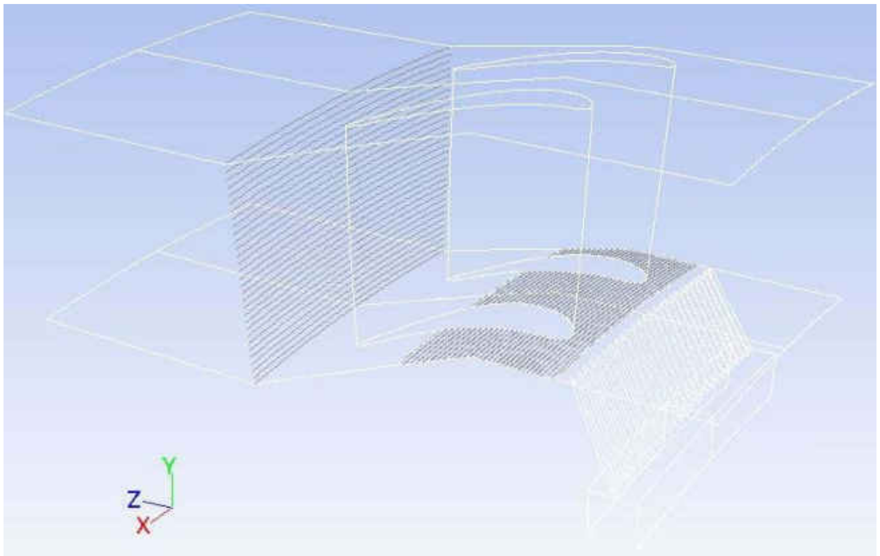

Figure 71 surfaces where ζ and η are extracted for this study

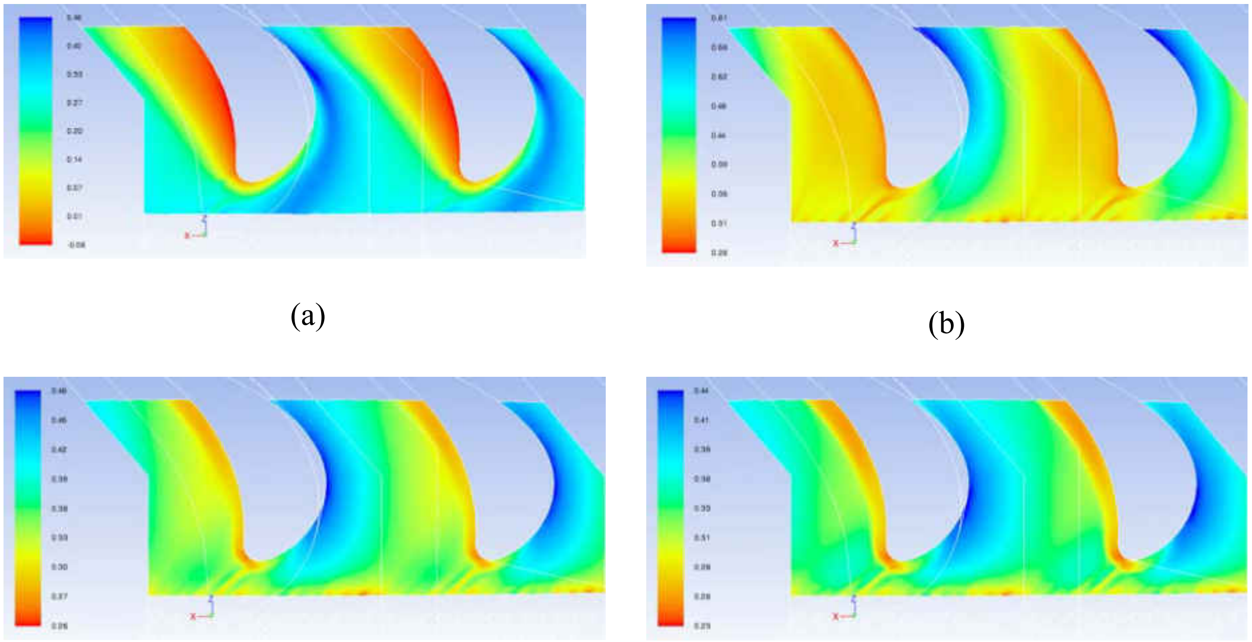
(a)
(b)
(c)
(d)

Figure 72 Typical obtained η from the 8.16 million cells grid: case (a) M04A43, (b) M10A43, (c) M19A43, and (d) M24A43

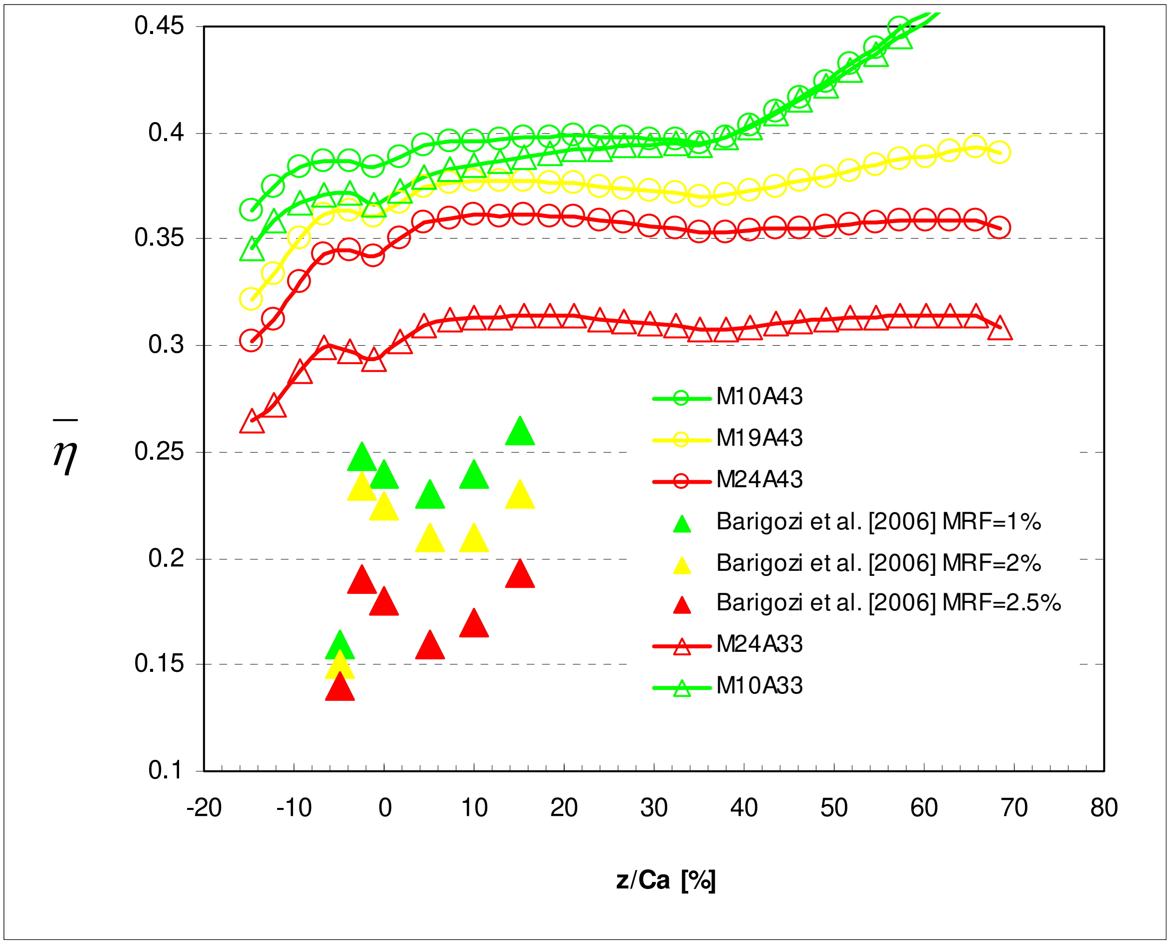

Figure 73 Validation of the current work with literature

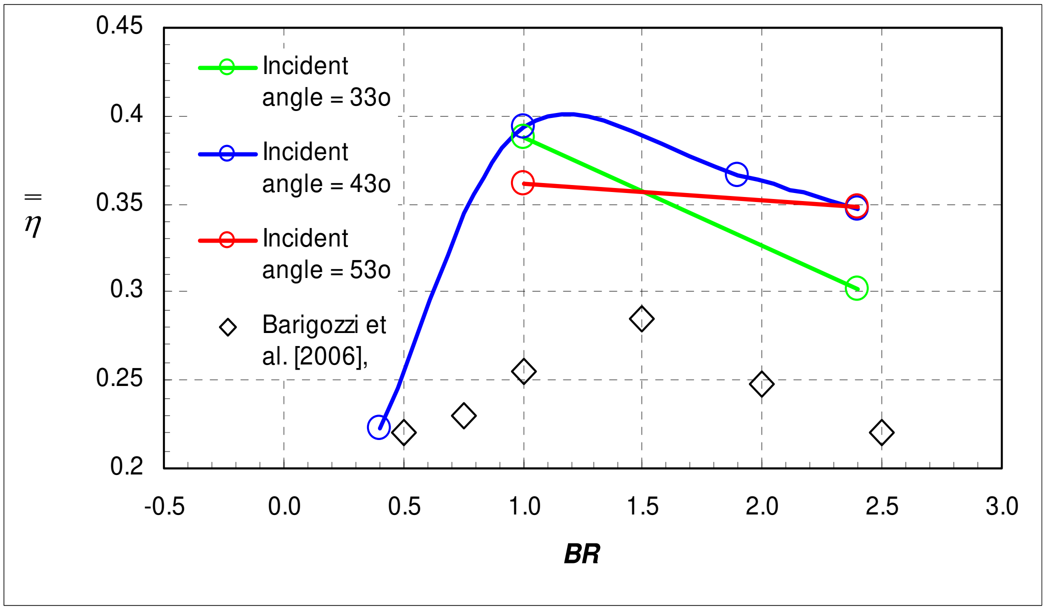

Figure 74 Validation of the current work with literature on

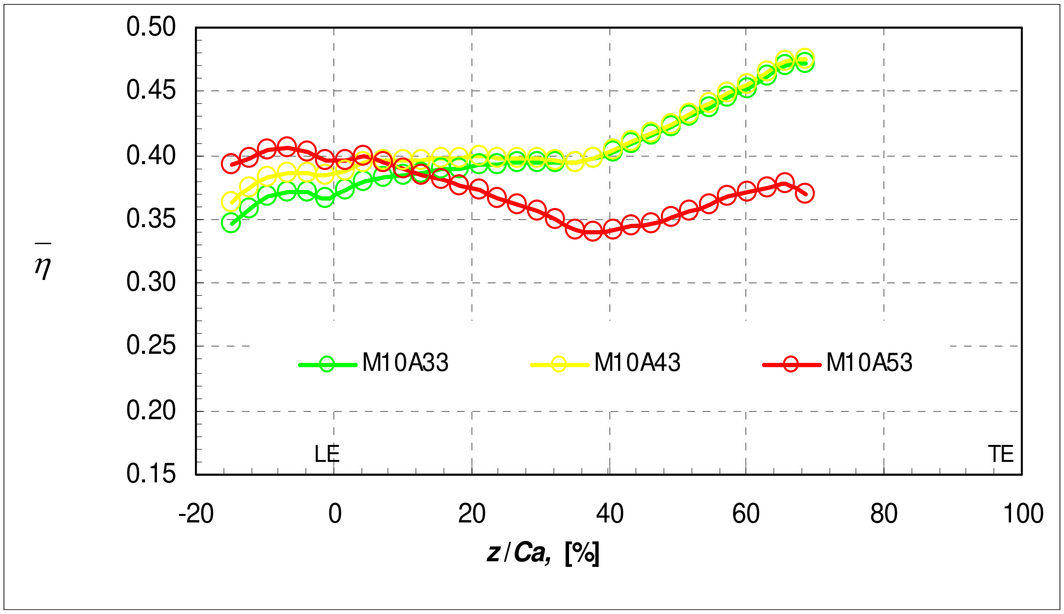

Figure 75 Plot of laterally-averaged η against flow angle Φ for BR=1

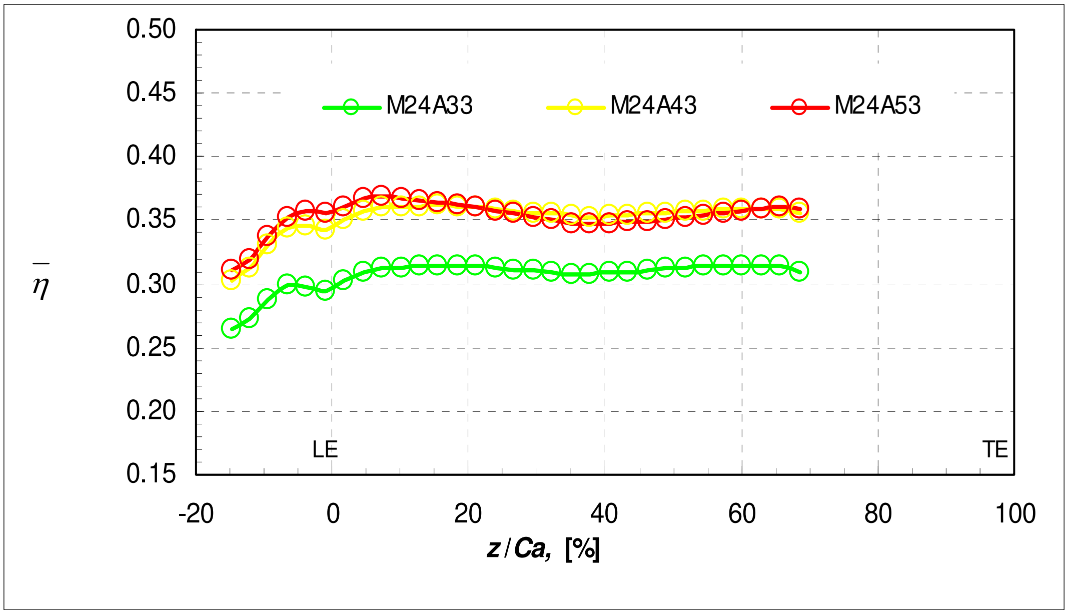

Figure 76 Plot of laterally-averaged η against flow angle Φ for BR=2.4

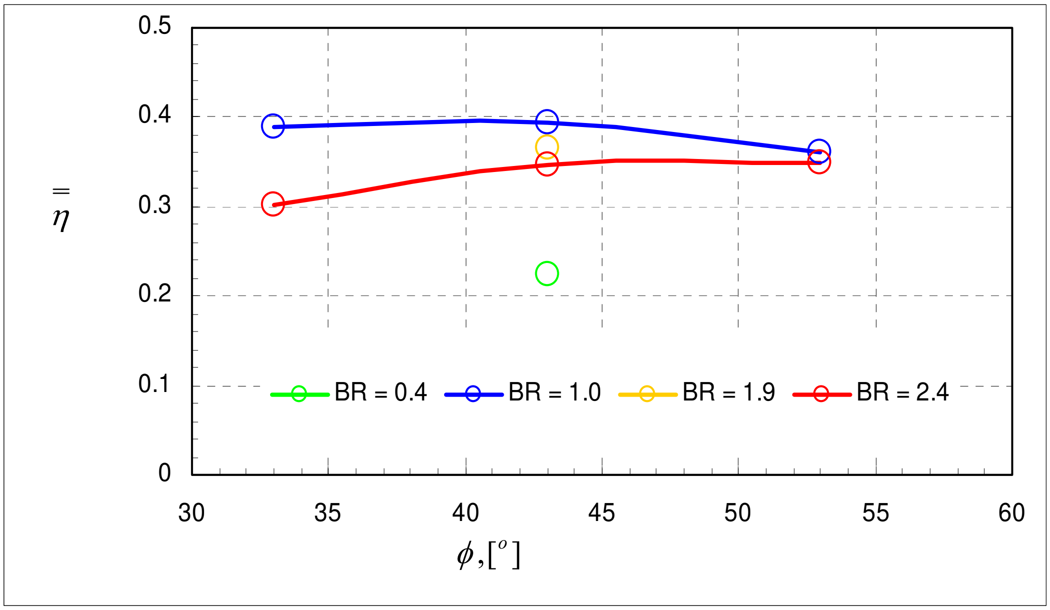

Figure 77 Plot of spatially-averaged η versus Φ

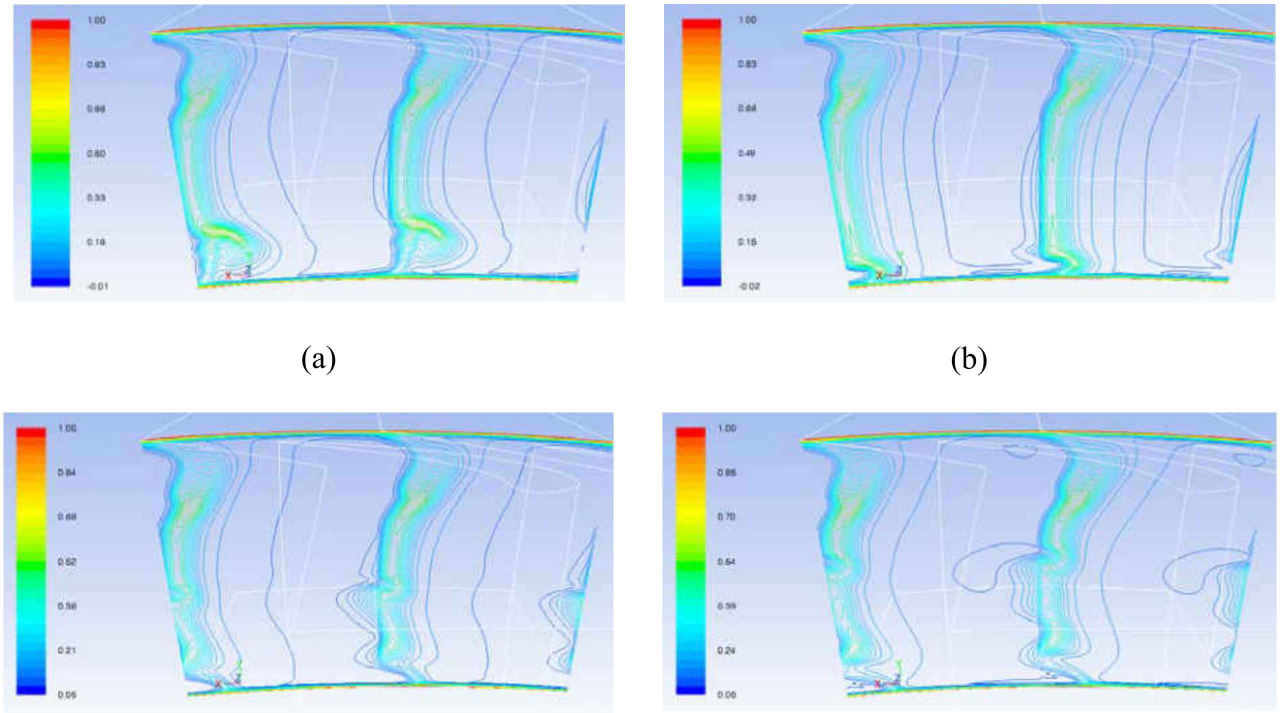

(a) (b)

(c) (d)

Figure 78 Contour plot of pressure loss coefficient, ζ at four blowing ratios: (a) M04A43, (b) M10A43, (c) M19A43, and (d) M24A43

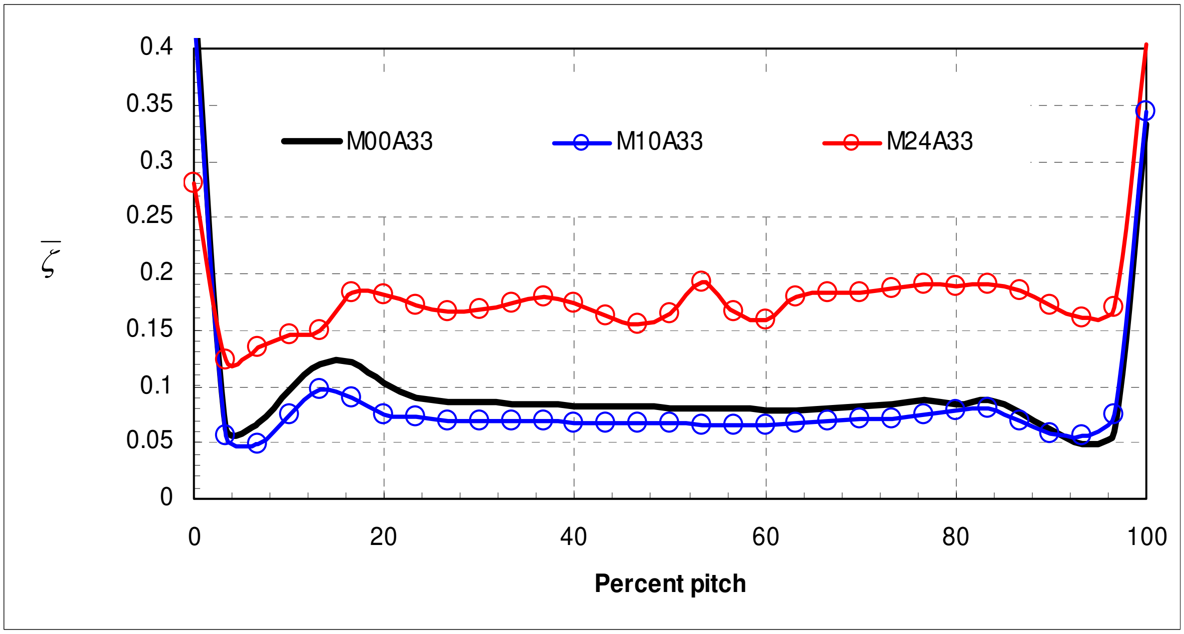

Figure 79 Laterally-averaged pressure loss coefficient, laterally-averaged ζ versus *BR* at *Φ*=33°

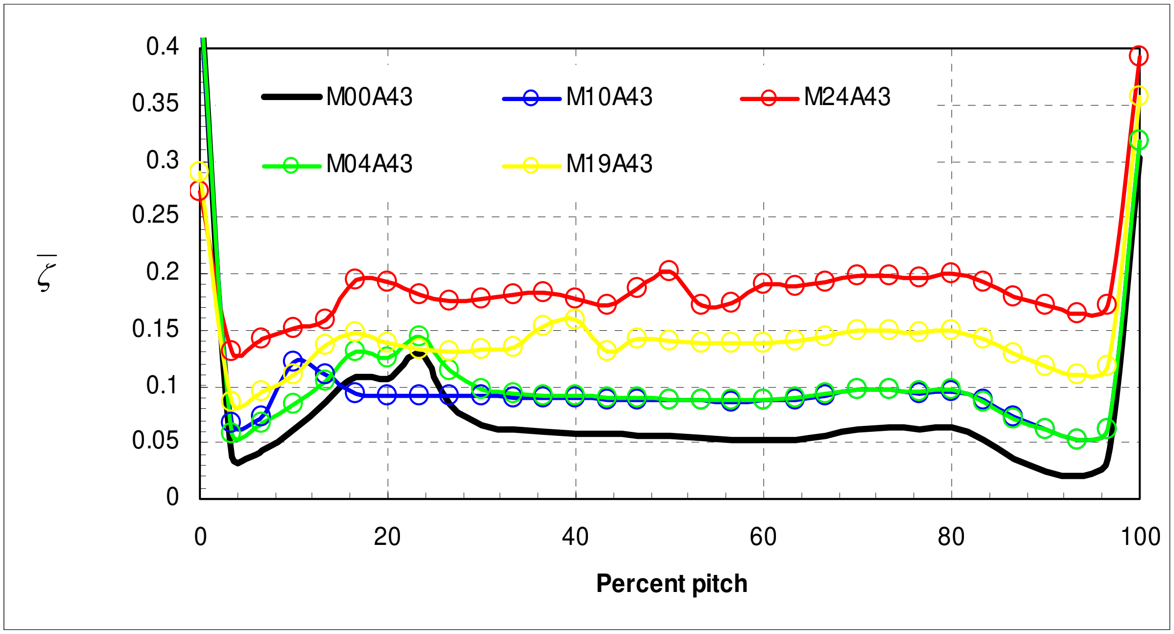

Figure 80 Laterally-averaged pressure loss coefficient, laterally-averaged ζ versus *BR* at *Φ*=43°

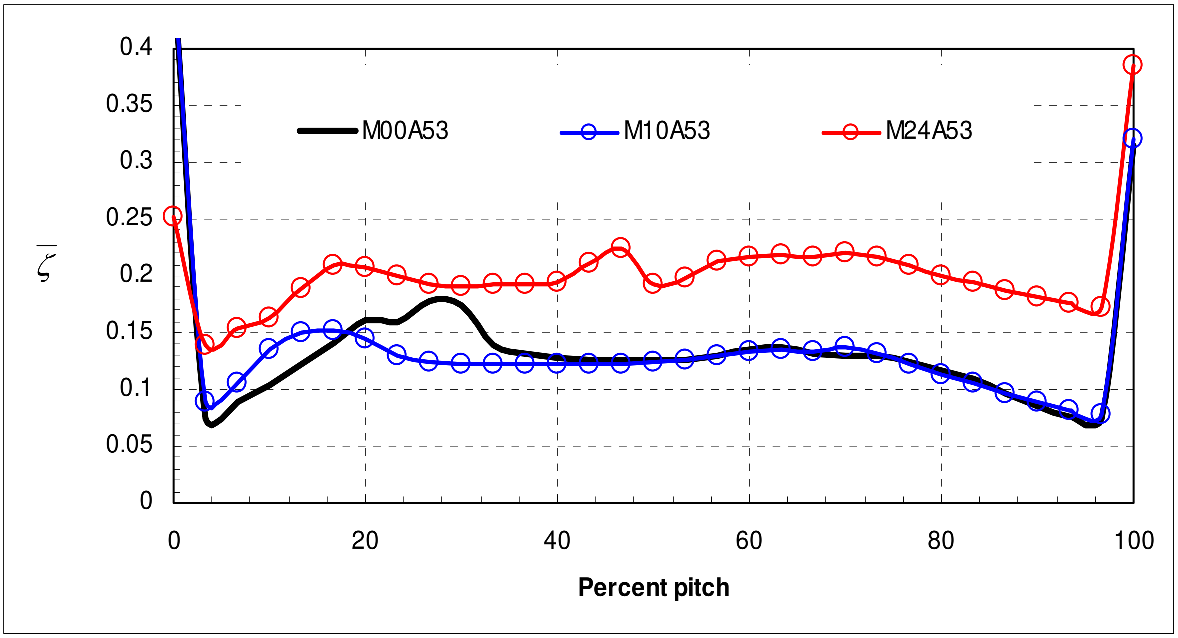

Figure 81 Laterally-averaged pressure loss coefficient, laterally-averaged ζ versus *BR* at Φ=53°

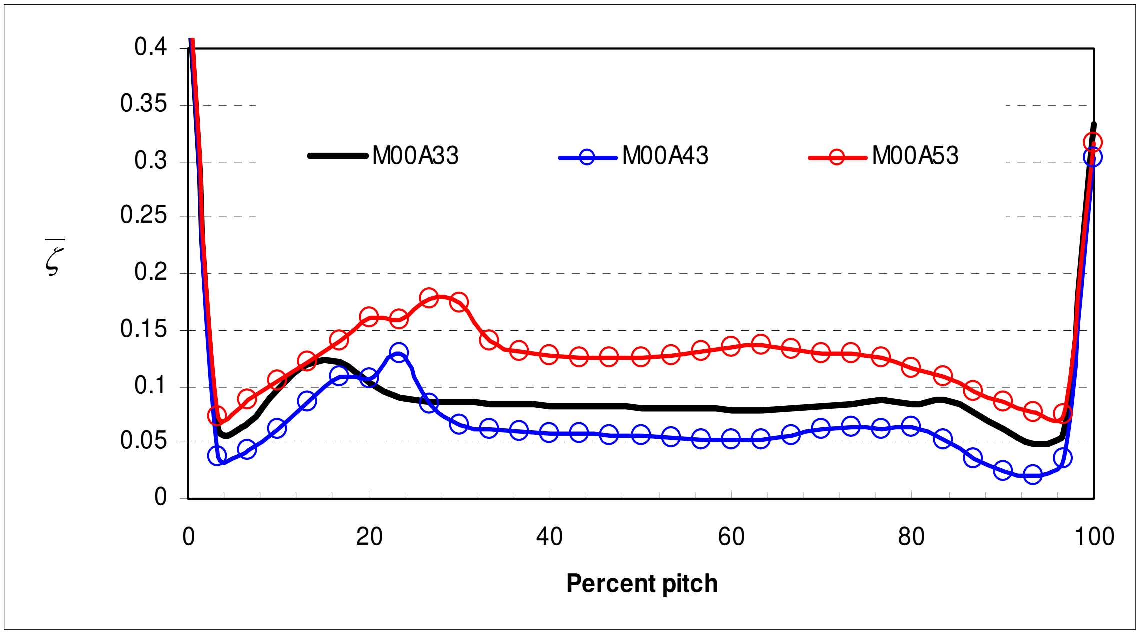

Figure 82 Laterally-averaged pressure loss coefficient, laterally-averaged ζ versus floe angle Φ at *BR*=0 (baseline)

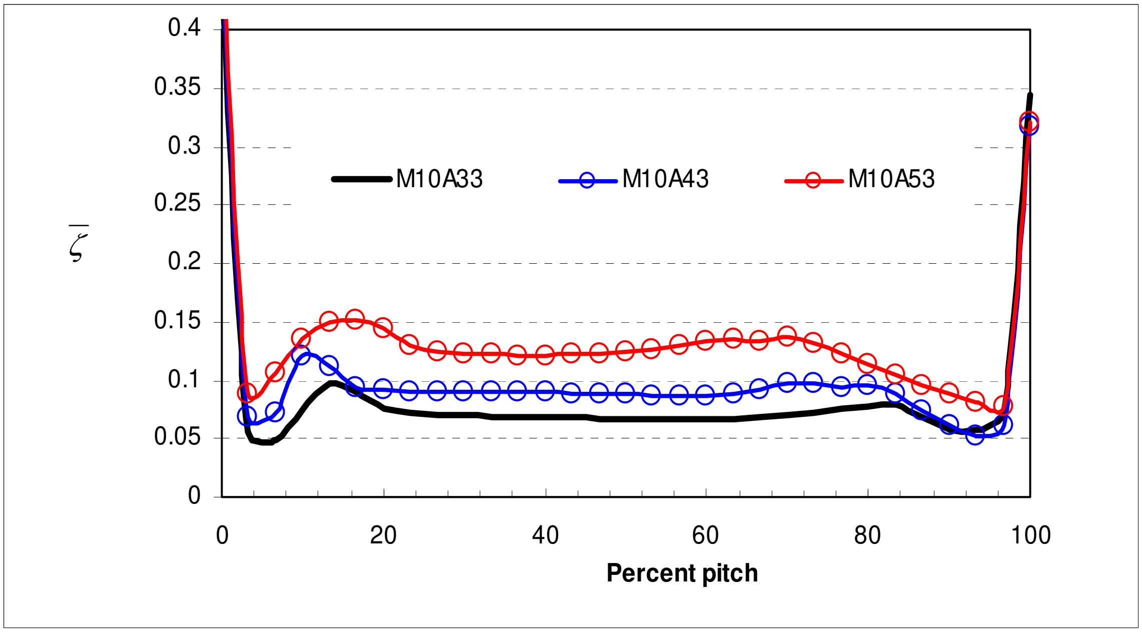

Figure 83 Laterally-averaged pressure loss coefficient, laterally-averaged ζ versus floe angle Φ at *BR*=1.0

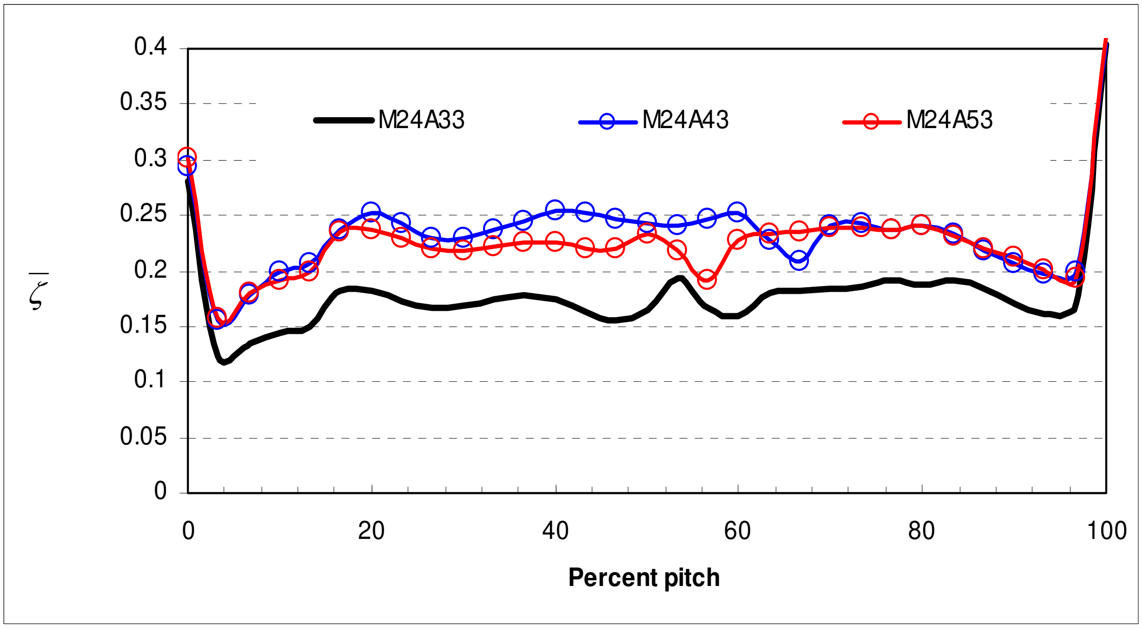

Figure 84 Laterally-averaged pressure loss coefficient, laterally-averaged ζ versus floe angle Φ at *BR*=2.4

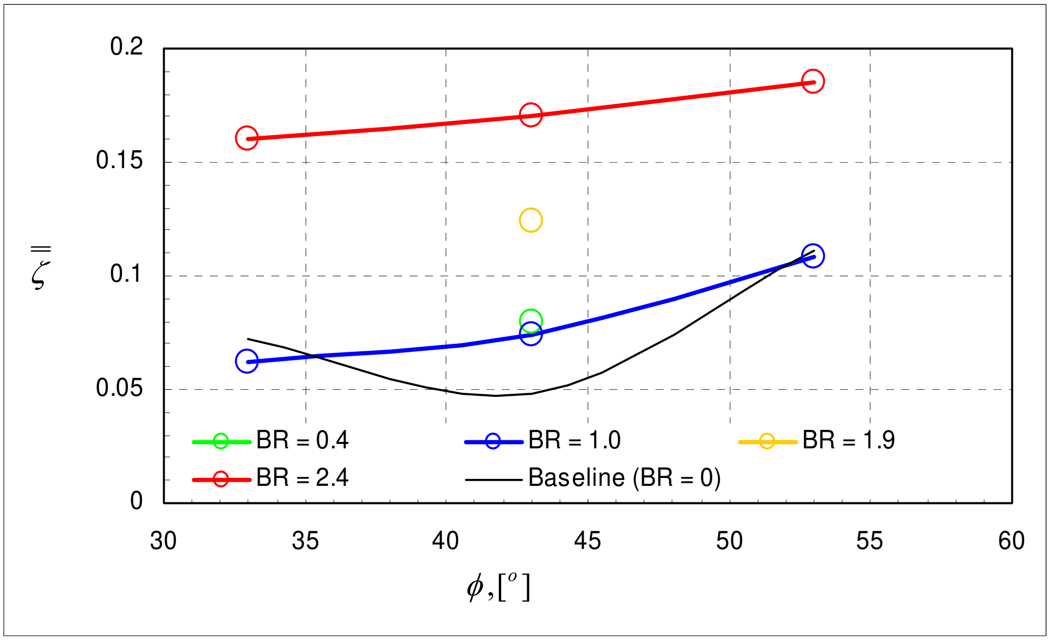

Figure 85 Spatially-averaged ζ versus flow angle Φ

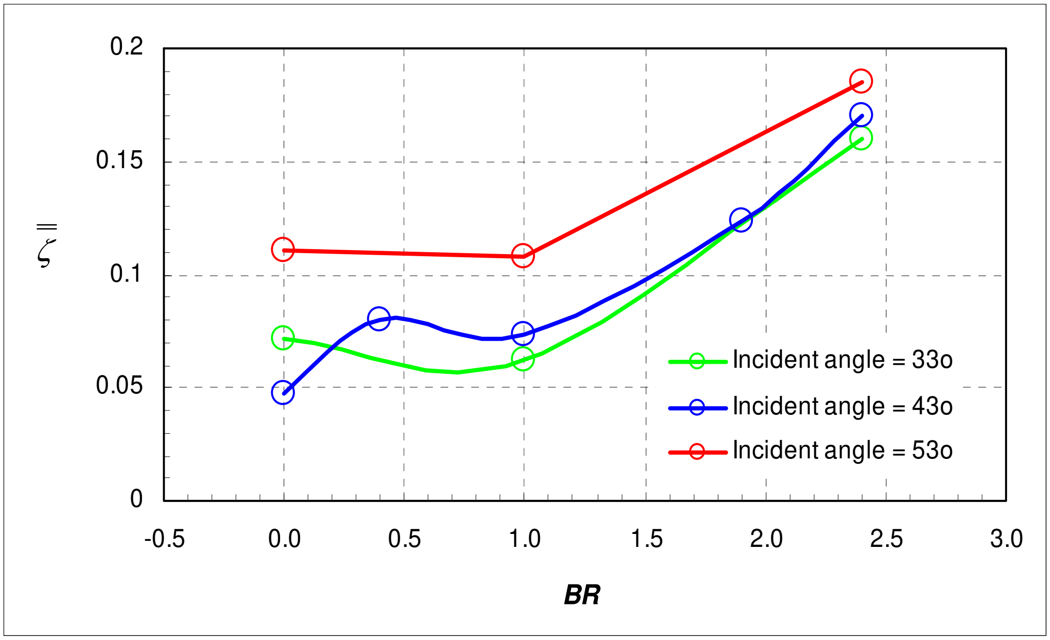

Figure 86 Spatially-averaged ζ versus blowing ratio at three flow angles Φ

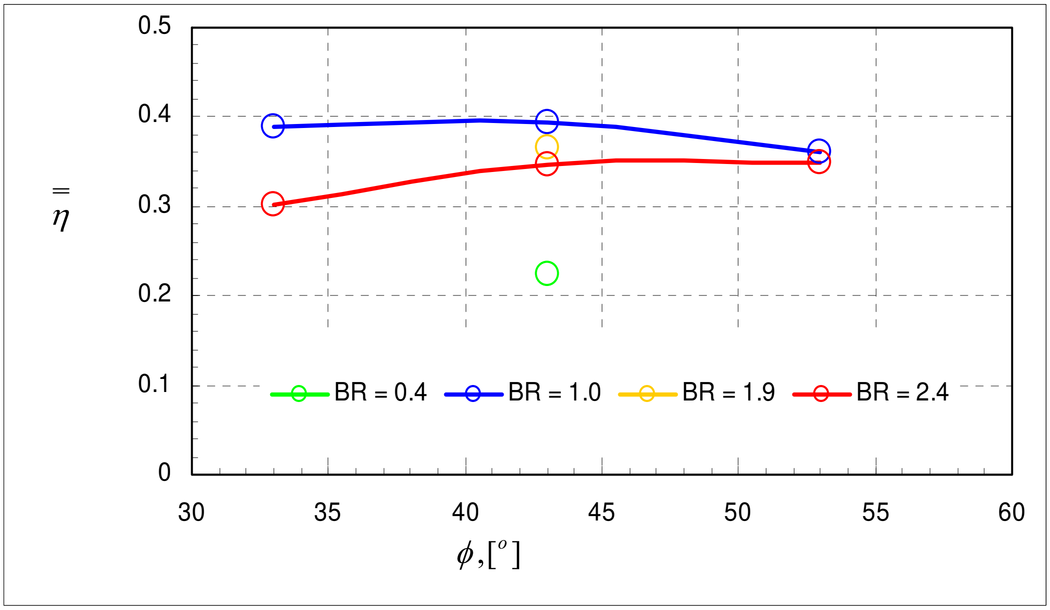

Figure 87 Spatially-averaged η versus flow angle at four blowing ratios

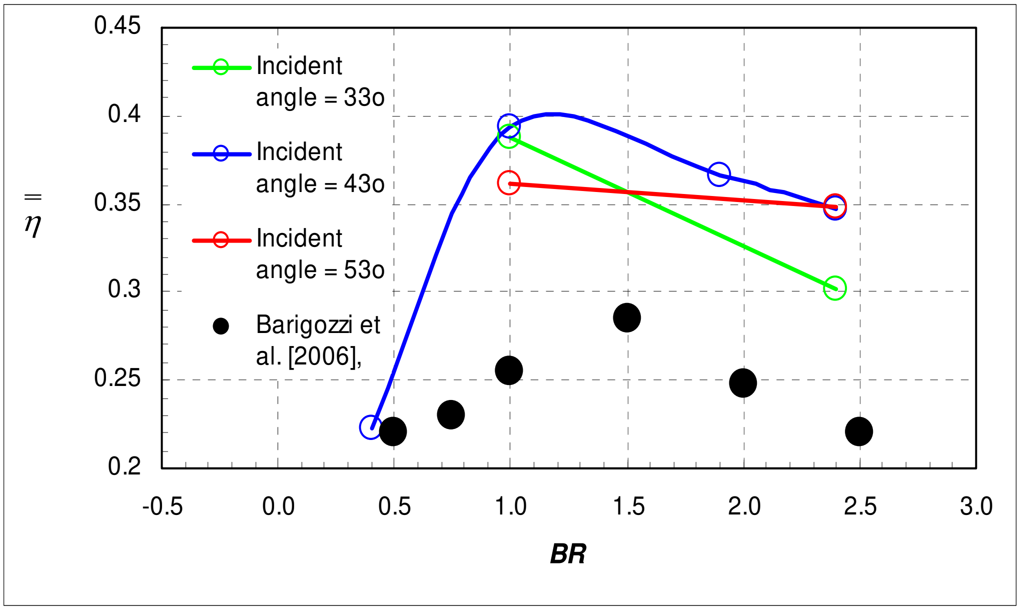

Figure 88 Spatially-averaged η versus blowing ratios at three mainstream flow angles Φ

CHAPTER VI. CONCLUDING REMARKS AND FUTURE WORKS

Concluding Remarks

In the first part of the work, conjugate heat transfer numerical models for cylindrical-shaped film hole with and without trench; conical-shaped film holes are modeled with grid independent study. The numerical results show good agreement with in-house experiments as well as literature data. Conductivity effects of the material are taken into account and both film cooling effectiveness (FCE) as well as cooling uniformity coefficient (*CUC*) is studied.

A benchmarking between 2 conical-shaped film holes (CON3 and CON6) and a cylindrical-shaped film hole (CYL) are conducted. CON6 and CON3 shows a dominant performance over the CYL (baseline) in terms of centerline FCE as well as laterally-averaged FCE. Conical-shaped film holes with 6^o flaring angle (CON6) give a higher *FCE* versus the 3^o one (CON3). In general, a conical-shaped film hole with blowing ratio in the middle level (*BR*=1) will give the best centerline FCE as well as laterally-averaged FCE, while in cylindrical-shaped film hole, *BR* of low level brings a better film performance than *BR* of 1 and 1.5. All of these are obviously reflected on the spatially-averaged *FCE* that one will benefit the most with the highest flaring conical angle (CON6) at middle level of blowing ratio (*BR*=1): the spatially-average FCE can gain up to 50% and 25% more compared to the *BR*=1 and *BR*=1.5 conical-shaped film hole cases respectively (as least for the range of study in this work).

However, CON6 at *BR*=0.5 give the best uniformity of temperature distribution on the studied downstream surface (up to 15% more in term of spatially uniformity coefficient, $\overline{\overline{CUC}}$). It is worth to note that $\overline{\overline{CUC}}$ is reduced tremendously at highest blowing ratio (*BR*=1.5) for both CON3 and CON6, but it is opposite for the cylindrical-shaped hole where it actually gains its best uniformity of temperature distribution with highest blowing ratio (*BR*=1.5), i.e. it can gain up to 15% more in $\overline{\overline{CUC}}$ compare to *BR*=1 case.

It is well known that the trenched film hole outperforms the cylindrical film cooling hole. A design of experiment was performed to a cylindrical film hole sitting on a trench to find even the best combination of geometrical and flow condition parameters. Four factors are considered as process factors: *p/D*, *s/D*, *BR* and *DR*. The first order and second order of factor pitch-to-diameter ratio obviously play the most important factor among the four with up to 25% and 13% of significant values, respectively. Here, we see again trenched film hole perform the best at its middle blowing ratio (*BR*=1) rather than *BR*=0.5 or *BR*=1.5. It is interesting about this design of experiment that for the two-way factor (*s/D*)(*DR*): one can gain up to 400% of spatially-average FCE if one sets both (*s/D*x*DR*) from (1,1) down to (-1,-1). Last, the trench depth typically gives higher laterally-averaged FCE at deeper trench: up to 50% more in $\overline{\overline{\eta}}$ if one increases *s/D* from 0.1 to 0.55; but there is only 5% more in $\overline{\overline{\eta}}$ if one increases s/D to the highest level (*s/D*=1). This result agrees with several works in the available literature.

In the second part of the work, a test rig of film cooling on the ID platform of an annular cascade of 3D GE-E3 airfoils was built and a corresponding numerical model also developed and once again the testing data favorably correlated to the numerical simulation results as well as the relevant open literature. The endwall film cooling numerical model is then built based on the aerodynamic model from chapter IV, and the interaction between the mainstream and the film cooling jets were investigated extensively. Four blowing ratios at three incident angles which make up 11 cases were investigated.

At an flow angle at the middle level (Φ=43^o), any deviation away from BR=1 will give a decrease of film cooling performance. However, for the BR=1, there is not much difference in terms of aerodynamics affecting film performance between Φ=33^o and Φ=43^o, but FCE will drop if one has a higher flow angle (Φ=53) of the incoming mainstream. For the BR=2.4, higher flow angle actually gives the best film performance: one can gain up to 17% more compared to Φ=33^o.

The ratio of the mainstream mass flux and the coolant jets should be equal to gain the best film cooling on the hub platform. At 43^o flow angle, one can pay 100% more aerodynamic lost due to increase BR from 1 to 2.4. With BR=1, one pays only a maximum of 40% with a BR=1 at 43% in terms of pressure loss coefficient with respect to the baseline (no film cooling); it actually gives the same amount of pressure in the cases of Φ=33^o or Φ=53^o between the BR=1 and the baseline.

Future Work Recommendations

In this study, preliminary conclusion can be inferred from 11 cases for the interaction behavior between the main stream flow and the injected film cooling jets, as in the current study for the annular cascade investigation. However, it would be great to obtain a complete 15 cases to ensure the current conclusions in the study.

Large eddy simulation for the film cooling on the flat plate can be conducted and benchmarking between LES results and RANS results should give a good conclusion and gain more fidelity. When one needs to obtain quick and less expensive results, a RANS viscous model in numerical simulation is sufficient.

One can check to see if the trench improvement obtained from film cooling on flat plate is still applicable for the film on the stagnation region on the annular cascade. With a simple design of experiment, one can find the best combination of the distance of the trench location before the leading edge, the trench depth and the blowing ratio condition to give the optimum film cooling performance as well as the least aerodynamic loss downstream of the cascade.

Again, LES can be employed in this complex 3D annular cascade to validate the RANS simulation and gain better confidence about the conclusions which have been made base on the RANS simulation, which was already validated with in-house experiment and with the literature. In-house experimental film cooling need to performed and will add to the fidelity of the current study results.

LIST OF REFERENCES

Boyle, R. J., and Senyitko, R. G., 2003, "Measurements and Predictions of Surface Roughness Effects on Turbine Vane Aerodynamics," ASME Paper No. GT2003-38580.

Bunker, R. S., 2005, "A Review of Shaped Holes Turbine Film Cooling Technology", ASME J. Heat Transfer, 127, pp. 441–453

Bunker, R. S., Bailay, J.C., Lee, C.P., and Abuaf, N., "Method for Improving the Cooling Effectiveness of a Gaseous Coolant Stream, and related Articles of Manufacturer", US Patent 6,234,755, 2001.

Bunker, R., 2002, "Film Cooling Effectiveness due to Discrete Holes Within a Traverse Surface Slot", ASME paper GT-2002-30178

Burd, S.W. and Simon, T.W., "Flow Measurement in a Nozzle Guide Vane Passage with a Low Aspect Ratio and Endwall Contouring", Journal of Turbomachinery", Vol. 122, 2000, pp. 659-666.

Chiang, C.L., 2003, Statistical Methods of Analysis, World Scientific Publishing Co. Pte. Ltd., Singapore, 467-468.

Colban, W., Gratton, A., Thole, K.A. and Haendler, M., "Heat Transfer and Film-Cooling Measurements on a Stator Vane With Fan-Shaped Cooling Holes", Journal of Turbomachinery, Vol. 158, 2006, pp. 53-62.

D.M. Kercher, 2003, "Film-Cooling Bibliography 1940-2002", ???

Dorrington, J.R. and Bogard, D.G., 2007, "Film Effectiveness Performance for Coolant Holes Embedded inVarious Shallow Trench and Crater Depressions," ASME paper GT-2007-27992.

E.R.G. Eckert and R.M. Drake, Jr., 1987, "Analysis of Heat and Mass Transfer", Hemisphere Publishing Corporation

Eriksen, V. L., and Goldstein, R. J., 1974, "Heat Transfer and Film Cooling Following Injection through Inclined Circular Circular Tubes" ASME Journal Heat Transfer, 96, pp. 239-245

Fluent, 2009, "Fluent Version 6.3.26", USA, ANSYS Inc

Fluent, 2010, "Fluent Version 12.1", USA, ANSYS Inc.

Friedrich, S. (1991). Endwall Film-Cooling in Axial Flow Turbines. Ph.D. Dissertation

Gambit, 2009, "Gambit Version 2.3.16", USA, ANSYS Inc

Goldstein, R.J., Eckert, E.R.G., Ramsey, J.W., 1968, "Film Cooling with Injection Through Holes: Adiabatic Wall Temperatures Downstream of a Circular Hole", Paper No. 68-GT-19, Gas Turbine Conference, Washington, D.C., USA

Goldstein, R.J., 1970. "Film Cooling Following Injection Through Inclined Circular Tubes. Israel Journal of Technology" Volume 108 (1-2): p. 145-154

Gritsch, M., Schulz, A. and Wittig, S., 2003. "Effect of Internal Coolant Crossflow on the Effectiveness of Shaped Film-Cooling Holes", Journal of Turbomachinery, Vol. 125, p547-554

Harrison, K.L. and Bogard, D.G., 2007, "CFD Predictions of Film Cooling Adiabatic Effectiveness for Cylindrical Holes Embedded in Narrow and Wide Tranverse Trenches," Paper No. GT-2007-28005, IGTI Turbo Expo, Montreal, Canada

Harrison, S., 1989, "The Influence of Blade Stacking on Turbine Losses", Ph.D. Thesis,

J.G.V. Bohl, 1940, "Behavior of Parallel Air Streams", Ingenieur Archiv, Vol. 11, pp 295 (in German)

Javadi, K. and Javadi, A., 2008, "Introducing Film Cooling Uniformity Coefficient (CUC)", ASME International Mechanical Engineering Congress and Exposition, Boston, Massachusetts, Paper No. IMECE 2008-68502

Johnson, P.L., Nguyen, C.Q., Ho, S.H., and Kapat, J.S., 2010, "Sensitivity Analysis of Domain Considerations for Numerical Simulations of Film Cooling". Proceedings of 14th International Heat Transfer Conference, Washington D.C., USA, ASME-IHTC14-23241

Kapat, J.S. (2009). Private Communication. University of Central Florida, Orlando, Florida

Kawai, T., Adachi, T. and Akashita, K., "Structure and decay of secondary flow in the downstream of a cascade", Japan Society of Mechanical Engineers, Vol. 28, No. 242, 1985, pp. 1642-1650.

Kline, S., and McClintock, F., 1953, "Describing Uncertainties in Single-Sample Experiments", Mechanical Engineering, 75, pp. 3-8

Knost, D.G. and Thole, K.A., 2003 [2003]. "Computational Prediction of Endwall Film-Cooling for a First Stage Vane",

Kost, F.and Nicklas, M., "Film-Cooled Turbine Endwall in a Transonic Flow Field: Part I—Aerodynamic Measurements", Journal of Turbomachinery, Vol. 123, 2001, pp. 709-720.

Kunze, M., Vogeler, K., Brown, G., Prakash, C. and Landis, K., "Aerodynamic and Endwall Film Cooling Investigations of a Gas Turbine Nozzle Guide Vane Applying Temperature-Sensitive Paint", ASME Processding of Turbo Expo 2009, Orlando, Florida, 2009, Paper GT2009-59412.

Langston, L.S., "Cross Flow in a Turbine Cascade Passage", Gas Turbine Conference and Products Show, New Orleans, Louisiana, 1980.

Liu Q., "Study of Heat Transfer Characteristics of Impinging Air Jet Using Pressure and Temperature Sensitive Luminescent Paint", Ph.D. Dissertation, Orlando, UCF, 2006.

Minitab, 2007, "Minitab 15 Statistical Software English", USA, Minitab Inc.

Montgomery, D.C., 2001, Design and Analysis of Experiments 5th edition, John Wiley & Sons, Inc., New York.

Myers, R. H., Montgomery, D.C., and Anderson-Coo, C.M., Response Surface Methodology: Process and Product Optimization Using Designed Experiments, 3rd ed., John Wiley & Sons, New Jersey, 2009, Chaps. 7

Nguyen, C.Q., Rodriguez, S., Zuniga, H., Ho, H.H. and Kapat, J. S., 2009. "Sensitivity Analysis of Flow Conditions and Geometric Parameters on the Film Cooling Effectiveness for a Flat Test Plate, Part 1: Single Row of Cylindrical Holes Film Cooling" ASME Proceedings of Summer Heat Transfer 2009, San Francisco, California, USA Paper HT-88141

Nguyen, C.Q., Tran, N.T.V., Bernier, B.C., Ho, S.H., and Kapat, J. S., "Sensitivity Analysis for Film Effectiveness on a Round Film Hole Embedded in a Trench Using Conjugate Heat Transfer Numerical Model". ASME Proceedings of Turbo Expo 2010, Glasgow, UK, 2009, Paper GT2010-22120.

Nicklas, M, "Film-Cooled Turbine Endwall in a Transonic Flow Field: Part II—Heat Transfer and Film-Cooling Effectiveness", Journal of Turbomachinery, Vol. 123, 2001, pp. 720-729.

Pepe, D.M. and Ittleson, A.J., 2004, "Laser Drill Hole for Film Cooling", US Patent 6,744,010 B1

Qiu, Junfen, 2001, "Temperature Sensitive Paint Development for Thermographic Applications", MS Thesis, University of Central Florida, Orlando, FL

Ricklick, M.A., 2009. "Characterization of an Inline Row Impingement Channel for Turbine Blade Cooling Applications", Ph.D. Dissertation, University of Central Florida, Orlando, ,Florida

Rodriguez, S., 2008, "Effect of Pressure Gradient and Wake on Endwall Film Cooling Effectiveness", Ph.D. Thesis

Sauer, H., Müller, R., Vogeler, K., "Reduction of Secondary Flow Losses in Turbine Cascades by Leading Edge Modifications at the Endwall", J. of Turbomachinery, Vol. 123, 2001, pp. 207-213.

Sawyer, 1966, "Gas Turbine Engineering Handbook", 1st Edition, Stamford, CT. Gas Turbine Publications, Inc.

Sharma, O. P. and Butler, T. L., "Predictions of endwall losses and secondary flows in axial flow turbine cascades", Journal of Turbomachinery, Vol. 109, No. 2, 1986, pp. 229-236.

Sieverding, "Recent progress in the understanding of basic aspects of secondary flows in turbine blade passages", Journal of Engineering for Gas Turbines and Power, Vol. 107, No. 2, 1985, pp. 248-257.

Sinha, A. K., Bogard, D. G., and Crawford, M. E., 1991,"Film Cooling Effectiveness Downstream of a Single Row of Holes with Variable Density Ratio", ASME J. Turbomachinery, 113, pp. 442-449

Spencer, M.C., Jones, T.V., and Lock, G.D. 1996 "Endwall Heat Transfer Measurements in an Annular Cascade of Nozzle Guide Vanes at Engine Representative Reynolds and Mach Numbers", International Hournal of Heat and Fluid Flow 17: 139-147

Steinthornson, E., 2010. Private Communication. Parker Hannifin Inc., Mentor, Ohio

Sundaram, N. and Thole, K. A., "Bump and Trench Modifications to Film-Cooling Holes at the Vane-Endwall Junction", J. of Turbomachinery, Vol. 130, 2008, pp. 41013-41022.

Taslim, M.E. and Ugarte, S., 2004, "Discharge Coefficient Measurements for Flow through Compound-Angle Conical Holes with Cross-Flow", International Journal of Rotating Machinery", 10, pp. 145-153

Timko, L.P., "Energy Efficient Engine High Pressure Turbine Component Test Performance Report", 1982, NASA CR-168289.

University of Cambridge; see also Harrison, S., 1989, "Secondary Loss Generation in a

Vogt, H.F. and Zippel, M., "Sekundärströmungen in Turbinengittern mit geraden und gekrümmten Schaufeln; Visualisierung im ebenen Wasserkanal", Forschung im Ingenieurwesen, Vol. 62, 1996. pp. 247-253.

Wang T., Chintalapati S., Bunker R., and Lee CP, 2002, "Jet Mixing in a Slot," Experimental Thermal and Fluid Science, 22, pp. 1-17.

Waye, S. K., and Bogard, D.G., 2006, "High Resolution Film Cooling Effectiveness Measurements of Axial Holes Embedded in a Transverse Trench with Various Trench Configurations" Paper No. GT-2006-90226, IGTI Turbo Expo, Barcelona, Spain

Zhang, L.J. and Jaiswal, R.S., "Turbine Nozzle Endwall Film Cooling Study Using Pressure-Sensitive Paint", Journal of Turbomachinery, Vol. 123, 2001, pp. 730-739.

Zuniga, H. A., 2007, "Study of Discharged Coefficient and Trends in Film Cooling Effectiveness of Conical Holes with Increasing Diffusion Angles", MS Thesis